Nano-Structured Catalyst Preparation and Application in Fischer-Tropsch Synthesis

ナノ構造触媒の調製およびフィッシャー・トロプシュ合成への応用

Chuang XING

邢 闖

Supervisor: Prof. **Noritatsu TSUBAKI**

Tsubaki Laboratory

Graduate of Science and Engineering for Education

University of Toyama

August 2014

Contents

Overview and Preface

This thesis is for a doctorate of the University of Toyama.

Methane and carbon dioxide are well-known greenhouse gases. Large amounts of methane are widely available in nature in the form of natural gas while substantial amounts of carbon dioxide are generated by human activity. Therefore, the utilization of these two gases transforms to chemical products, which is an important and hot topic in 21^{th} century. Carbon dioxide reforming of methane or methane dry reforming is an efficient route for conversion of these two greenhouse gases into synthesis gas (syngas), the produced syngas with a H_2/CO molar ratio around 1 is suitable to be transformed to valuable hydrocarbons through Fischer-Tropsch synthesis (FTS).

The depletion of crude oil and the rapid growing demand of liquid fuels have attracted more interest for the synthesis of alternative fuels from the rich-reserved coal, natural gas and renewable biomass via FTS reaction. Generally, the FTS reaction mainly produces normal hydrocarbons and some building-block chemicals such as lower olefin, which can not be directly used as the transportation fuels, especially for the extensively demanded gasoline. Additional hydrocracking and isomerization steps are usually employed for the production of gasoline in industry. But these steps increase the operating cost and complexity of the processes. So it is more promising for the direct synthesis of gasoline components (rich in middle isoparaffin) from syngas without extra processes.

Zeolite crystals with inherent micropores, high acidity, uniform micropore size and shape selectivity have been widely applied as heterogeneous catalysts or catalyst supports in the petrochemical and fine chemical industries. Considering that zeolite is powerful in cracking and isomerization of hydrocarbons owing to their unique shape selectivity and acidity, and that the intrinsic cracking rate of linear hydrocarbons increases with the carbon number enhanced gasoline production with improved isoparaffin content can be obtained when a conventional FTS catalyst is combined with a zeolite.

In **Chapter 1**, as FTS feed gas, syngas (CO + H_2) was produced via the carbon dioxide reforming reaction of methane by using Ni based catalyst. Deactivation and carbon deposition on catalysts are the biggest challenges for this reaction. In addition

of rare earth metals to Ni base catalyst, such as La, Ce, Zr and so on, these catalysts enhanced reaction activity as well as decreased carbon deposition.

In **Chapter 2** studied the conventional FTS reaction, by using the controllable encapsulation of cobalt clusters inside the channels of CNTs. With the combination of concentrated nitric acid refluxing, varied thermal treatment and wetness impregnation method on carbon nanotubes (CNTs), we realized the controllable encapsulation of cobalt clusters inside the channels of CNTs. The reaction results showed the increase CO conversion with increasing the filling degree of cobalt clusters inside the CNTs channels.

Chapter 3 *to* ***Chapter 6*** *researched particularly one-step synthesis of middle isoparaffin from syngas via FTS reaction with the tandem catalysis process.*

In **Chapter 3**, one-step synthesis of middle isoparaffin from syngas via FTS was realized facilely using the zeolite capsule catalyst with a core-shell structure. As compared with the usually used hydrothermal synthesis way for zeolite shell preparation limited the design and preparation of various zeolite shell enwrapping different core catalysts, the industrial scalability of zeolite capsule catalyst, and so on. An improved hydrothermal synthesis process named physically adhesive (PA) method in this chapter. The PA method presented in this report is very cost-saving, reliable and scalable, with which we could realize the industrialization of zeolite capsule catalyst more readily.

In **Chapter 4** designed a hierarchical HZSM-5 zeolite with combined micro- and mesopore structure via one-step approach by using TPAOH and F127 as dual templates. The hierarchical HZSM-5 exhibited significantly higher mesopore surface area and larger mesopore volume than conventional HZSM-5. The CO conversion of FTS reaction on the present catalyst increased significantly. Meanwhile, both of the C_{5+} hydrocarbons selectivity and the isoparaffin selectivity increased.

In **Chapter 5**, mesoporous zeolite Y was introduced as FTS support for direct synthesis of middle isoparaffin. Mesoporous zeolite Y was prepared by a two-step process consisting of acid leaching and base leaching. The CO conversion, isoparaffin and C_{5-11} selectivity of mesoporous zeolite Y supported Co based catalysts increased

significantly as compared with the pristine Y supported Co catalyst due to the optimized hydrocracking and isomerization function afforded by the hierarchical zeolite Y.

In prior studies, the conventional capsule catalyst with the size scale of 1000-2000 um, this is a significantly technological interest to reduce the size of the capsule catalyst. In **Chapter 6**, we designed the Fe base micro-capsule catalyst with unique size about 1-2 um. The micro-capsule catalyst with Fe/Silica core and H-ZSM-5 zeolite shell via an in-situ crystallization route on Fe/SBA-15 catalyst by using the SAC process was first synthesized and applied in direct synthesis of isoparaffin from syngas via FTS reaction. The newly developed heterogeneous catalyst preparation method reported here will be also widely applied in designing other similar micro-capsule catalyst for varied tandem catalysis processes.

Chapter 1 Promotional effect of La_2O_3 and CeO_2 on Ni/γ-Al_2O_3 catalysts for CO_2 reforming of CH_4

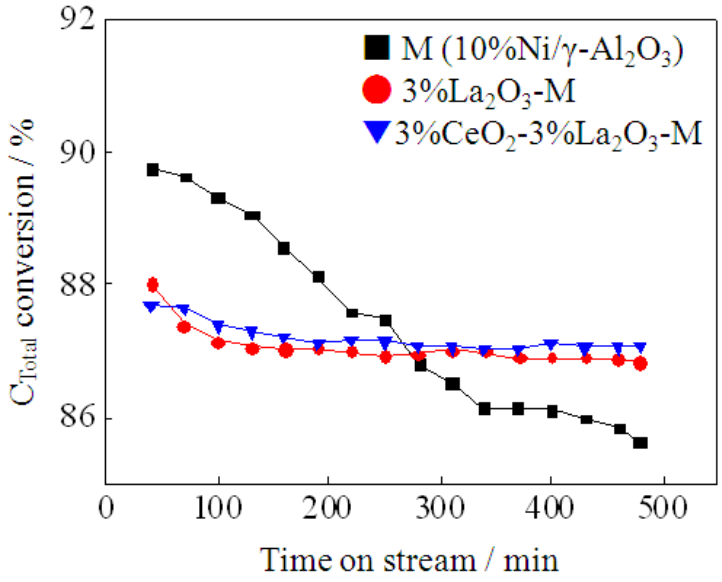

Abstract

The CO_2 reforming reaction of CH_4 was conducted by using Ni based catalyst prepared by co-impregnation method. The properties of the catalysts and the carbon deposition performance on the catalyst surface were surveyed by XRD, TPR, TG-DTA, and SEM. The results showed that the activity of the Ni/γ-Al_2O_3 catalyst with Ni loading of 10% was higher than those with other Ni loadings. However, the Ni/γ-Al_2O_3 catalyst was not stable in the continuous reaction due to a large amount of carbon deposition on the catalyst surface. Although the activity of Ni/γ-Al_2O_3 with the La_2O_3 and CeO_2 as promoters was not obviously increased, the carbon deposition on Ni/γ-Al_2O_3 with La_2O_3 and CeO_2 as promoters was greatly suppressed in the CO_2 reforming reaction of CH_4, and the amount of carbon deposition on the 10%Ni/3%CeO_2-3%La_2O_3-γ-Al_2O_3 catalyst were reduced 76.2 % compared with the 10%Ni/γ-Al_2O_3 catalyst due to alkaline function and dispersion enhancement of La_2O_3-CeO_2, as well as the electronic interaction between CeO_2 and Ni. The results of SEM showed that the moss-like carbon on the 10%Ni/γ-Al_2O_3 catalyst was hardly gasified with CO_2 and encapsulated Ni particles，resulting in the catalyst deactivation. On the other hand, the filamentous carbon on the 10%Ni/3%CeO_2-3%La_2O_3-γ-Al_2O_3 catalysts could be eliminated readily by gasifying with CO_2. Because of the suppression in the sintering of Ni particles and the dominant formation of the reactive filamentous carbon on the Ni based catalyst added by La_2O_3 and CeO_2 promoters, 10%Ni/3%CeO_2-3%La_2O_3-γ-Al_2O_3 catalyst showed stable activity in the continuous CO_2 reforming reaction of CH_4 at 1073 K and atmospheric pressure.

Keywords: Methane, CO_2 Reforming, La_2O_3-CeO_2, Promoter, Carbon Deposition

1.1 Introduction

In recent years, the catalytic process of CO_2 reforming of CH_4 (CDRM) (also called dry reforming) into synthesis gas ($CH_4 + CO_2 \rightarrow 2H_2 + 2CO$) has become an attractive but challenging subject for the chemical utilization of carbon-containing "greenhouse" gases (CH_4 and CO_2) [1]. This process generates synthesis gas ($CO + H_2$) with a H_2/CO ratio of 1:1 which is suitable for some industrial processes such as DME (dimethyl ether) synthesis, oxo synthesis and Fischer-Tropsch synthesis on Fe-based catalysts [2,3]. The extensive efforts have been made to develop novel and practical catalysts for this process [4,5].

Various catalysts, including Ni-based catalysts and supported noble metal catalysts, have been investigated for the CO_2 reforming of CH_4 [6-11]. The cheap Ni-based catalysts have high activity and selectivity. However, thermodynamic studies indicated that the Ni-containing catalysts are easy to cause carbon deposition by the side reactions in the CDRM, leading to the deactivation of the catalyst [12]. The side reactions to cause carbon deposition are the methane decomposition (1) and the CO disproportionation (2) [9]:

$$CH_4 \rightarrow C + 2H_2 \qquad (1)$$

$$2CO \rightarrow C + CO_2 \qquad (2)$$

Compared to Ni-based catalysts, the noble metal-based catalysts are less sensitive to carbon deposition [9]. However, their limited availability and expensive prices make them less favored for practical applications [13,14]. Therefore the development of carbon deposition resistant Ni-based catalysts for CO_2 reforming of CH_4 is requested.

In recent years, a number of studies on CO_2 reforming of CH_4 over supported Ni catalysts [15] have indicated that support may play an important role in the activity and

resistance of carbon deposition on the catalysts. The modified supports have been studied in order to improve the stability and carbon resistance of nickel catalysts, mainly by the addition of alkali and alkaline-earth metal oxides as well as rare earth oxides [16-19]. The rare earth oxides have a high oxygen storage capacity and can absorb or release oxygen reversibly in responding to the oxygen concentration in the gas-phase [20]. Their presence shows beneficial effect on the catalyst performance, such as improving the dispersion of the active species, delaying the transition of alumina support from γ-Al_2O_3 to low-surface-area phase α-Al_2O_3 [21,22]. It has been demonstrated that the addition of ceria as a promoter in the Ni/Al_2O_3 catalyst can enhance the activity, stability and resistance of carbon deposition in CH_4 reforming with CO_2 [23,24]. Lanthanum oxide has been previously used in catalysts for CDRM, mainly as the sole support component [25,26]. Studies conducted by Zhang et al. with Ni/Al_2O_3 and Ni/La_2O_3 catalysts in this reaction at 1023 K show that Ni/Al_2O_3 was active but deactivated soon, while Ni/La_2O_3 was not active but stable [27].

Although the importance of support and promoter effect to improve the performance of the nickel based catalysts has been recognized, there have been very few investigations on the CO_2 reforming of CH_4 over Ni based catalysts with lanthanum/cerium oxide binary promoters, as well as a lack of study on the effect of binary promoters on the stability and the carbon deposition behaviors of the catalysts.

In the present work, a series of supported Ni/γ-Al_2O_3 catalysts and La_2O_3-CeO_2 binary promoted Ni based catalysts were prepared with the impregnation method for investigating their performances and reactivity in the continuous reaction CO_2 reforming of CH_4. In particular, the carbon deposition and the stability of different catalysts during the reaction were evaluated.

1.2. Experimental

1.2.1 Catalyst preparation

Ni/γ-Al_2O_3 catalyst was prepared by incipient wetness impregnation of γ-Al_2O_3 (Catalysis Society of Japan, S_{N2}=151.2 m^2/g, total pore volume 0.53 ml/g, average pore diameter 14.08 nm) with the aqueous solution of nickel nitrate. The impregnated solid were was subsequently dried at 393 K for 12 h and calcined in air at 773 K for 2 h.

The La_2O_3 and/or CeO_2 promoted Ni based catalysts were prepared by incipient wetness impregnation of the γ-Al_2O_3 with the aqueous solution of $Ni(NO_3)_2 \cdot 6H_2O$, $La(NO_3)_3 \cdot 6H_2O$, and $Ce(NO_3)_3 \cdot 6H_2O$, followed by drying at 393 K for 12 h and calcining at 773 K for 2 h.

The loadings of nickel, lanthanum and/or cerium referred to the weight percent of Ni, La and/or Ce atoms in the catalyst in this study.

1.2.2 Catalyst characterization

1.2.2.1 Temperature-programmed reduction (TPR)

Temperature-programmed reduction (TPR) experiment was carried out in a quartz-made microreactor using 0.2 g dried catalyst with a 5 % H_2 diluted by nitrogen at atmospheric pressure. Before reduction, the catalyst was heated to 323 K in flowing N_2 for 70 min. Then, the 5% H_2 (45 ml/min) was passed over a catalyst sample, and the temperature was linearly raised from 323 K to 1073 K at a heating rate of 2.0 K/min. The effluence gas was analyzed with a gas chromatograph with a thermal conductivity detector (TCD), with nitrogen used as a reference.

1.2.2.2 X-ray diffraction (XRD)

Powder X-ray diffraction (XRD) Patterns were acquired on a RINT 2400 X-ray diffractometer, using monochromatic Cu-Kα radiation and scanning 2θ from 20º to 80º,

operated at 40 kV and 40 mA.

1.2.2.3 TG-DTA analysis

The carbon deposition on spent catalysts was examined by thermal analysis (TG-DTA), using a Germany NETZSCH thermoanalyzer (model STA 449C). The spent samples of 5 mg were heated at a rate of 10 K min^{-1} from room temperature to 1173 K in a flow air (10 cm^3 min^{-1}).

1.2.2.4 Scanning electron microscope (SEM)

Scanning electron microscopy (SEM) observations of the fresh and the spent catalyst samples were performed using a JSM-6360LV (JEOL Ltd., Japan).

1.2.3 Catalytic activity measurements

The CO_2 reforming reaction of CH_4 was carried out under atmospheric pressure in a quartz-tube fixed-bed reactor (i.d. 8 mm). The configuration of the reactor was showed in Fig. 1.1. The catalyst (0.2 g, 20-40 mesh) were reduced in situ in a flow of 99.999% H_2 (40 ml min^{-1}) at 773 K for 1 h prior to the reforming reaction. The reactor was heated up to the set temperature after the reduction. A gaseous mixture of $CH_4/CO_2/Ar$ with a volume ratio of 44.0:47.2:8.8 was fed into the reactor at a flow rate of 40 ml min^{-1}, in which argon was employed as an internal standard.

The effluent gas component from the reactor through the ice-water-cooled trap was analyzed using an on-line Gas Chromatograph Thermal Conductivity Detector (GC-TCD) with an active carbon column (TDX-01). Total carbon conversion was calculated as follows:

Total carbon conv. = CH_4 conv. × a/(a+b) + CO_2 conv.× b/(a+b)

(a,b were the contents of CH_4, CO_2 in the feed gas)

CH_4 conv. = 100 × [(CH_4/Ar in feed – CH_4/Ar in effluent)] / (CH_4/Ar in feed)

CO_2 conv. = 100 × [(CO_2/Ar in feed – CO_2/Ar in effluent)] / (CO_2/Ar in feed)

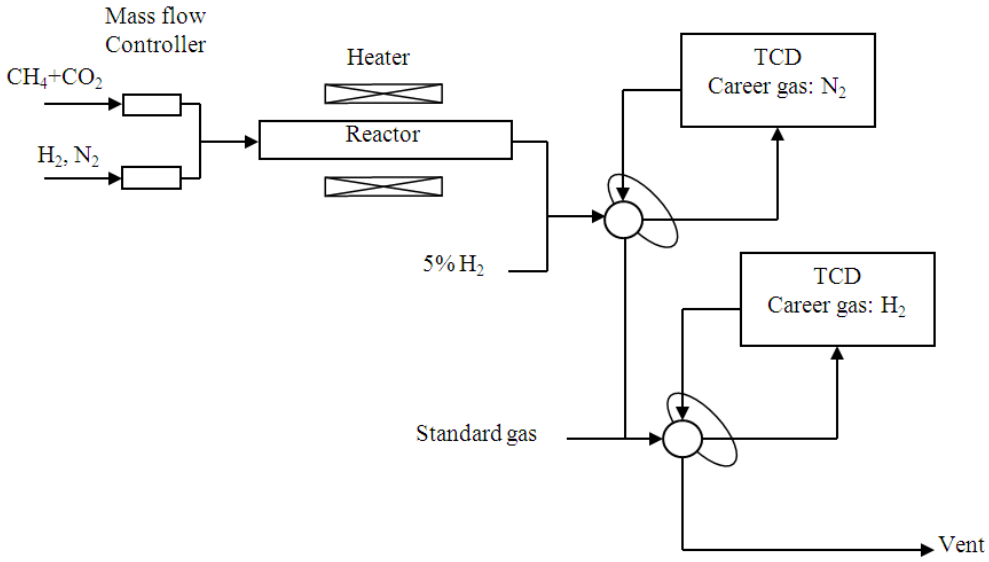

Fig. 1.1. Schematic diagram of the fixed bed reaction for CDRM.

1.3 Results and discussion

1.3.1 Influence of Ni loading in Ni / γ-Al_2O_3 catalysts on the reaction

Table 1.1 was the results of the CO_2 reforming of CH_4 at 973 K and atmospheric pressure for 8 h by using the Ni/γ-Al_2O_3 catalysts with different Ni loading, which were calcined at 773 K for 2 h, and reduced in situ by 99.999% H_2 at 773 K for 1 h. Fig. 1.2 shows influence of Ni loading on the carbon deposition on Ni/Al_2O_3 catalysts.

Table 1.1 Influence of Ni loading in Ni/γ-Al_2O_3 on the reaction [a]

Catalyst	Conversion / %			CO		H_2/CO
	CH_4	CO_2	C_{Total}	Selectivity/%	Yield/%	
5%Ni/γ-Al_2O_3	59.20	82.28	71.04	54.62	39.60	0.89
7%Ni/γ-Al_2O_3	59.82	81.95	71.19	54.88	39.19	0.89
10%Ni/γ-Al_2O_3	61.26	81.63	71.57	59.69	42.72	0.82
15%Ni/γ-Al_2O_3	64.72	81.87	68.83	54.68	40.06	0.92

[a] Reaction conditions: Cat., 0.2 g; T, 973 K; P, 0.1 MPa; reaction time, 8 h; feed gas, CH_4/CO_2/Ar=44.0/47.2/8.8, 40 ml min^{-1}.

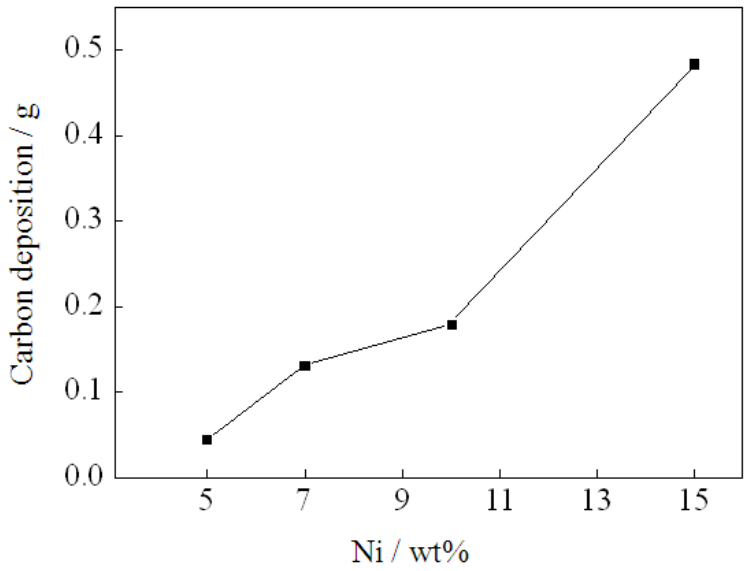

Fig. 1.2. Influence of Ni loading in Ni/γ-Al_2O_3 on the carbon deposition for CDRM (Reaction conditions: Cat., 0.2 g; T, 973 K; P, 0.1 MPa; reaction time, 8 h; feed gas, $CH_4/CO_2/Ar$=44.0/47.2/8.8, 40 ml min^{-1}).

Table 1.1 showed that the CH_4 conversion increased, and the CO_2 conversion did not change obviously, and the total carbon conversion increased with Ni loading increasing from 5% to 10%, and then the total carbon conversion decreased with Ni loading increasing from 10% to 15%. The CO and H_2 were only detected in the conducts besides unreacted CH_4 and CO_2. The selectivity and yield of the CO increased with Ni loading increasing from 5% to 10%, and then they decreased with Ni loading increasing from 10% to 15%. The total carbon conversion and CO yield were the highest on the 10%Ni/γ-Al_2O_3 catalyst. However, after 8 h reaction, the carbon deposition on Ni/γ-Al_2O_3 catalyst increased with the Ni loading increasing in the Fig. 1.2. Therefore, the Ni loading of 10% in the Ni/γ-Al_2O_3 catalyst was favorable for the CO_2 reforming of CH_4, and the total carbon conversion of 71.57%, the CO yield of 42.72%, and the ratio of H_2 to CO of 0.82 were obtained on the 10%Ni/γ-Al_2O_3 catalyst.

1.3.2 Influence of La_2O_3 promoter on the properties of Ni based catalyst

In order to reduce the carbon deposition on the Ni based catalyst, the La_2O_3 promoter was introduced into the 10%Ni/γ-Al_2O_3 catalyst for CDRM. Fig. 1.3 was the results of the CO_2 reforming reaction of CH_4 at 973 K and atmospheric pressure for 8 h by using the 10%Ni/La_2O_3-γ-Al_2O_3 catalysts with different La loading, whose precursors were calcined at 773K for 2 h, and reduced in situ by H_2 at 773K for 1 h. Fig. 1.4 showed the change of the carbon deposition on 10%Ni/La_2O_3-γ-Al_2O_3 catalysts with different La loading in the reactions.

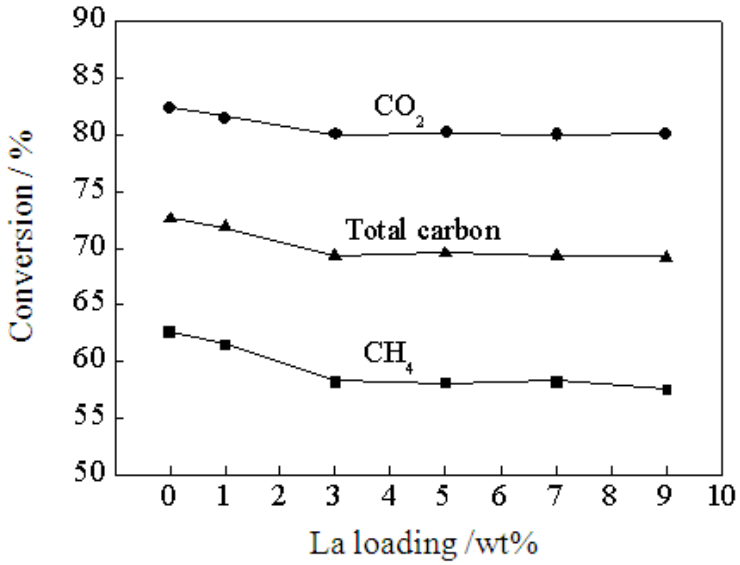

Fig. 1.3. Influence of the La loading in 10%Ni/La_2O_3-γ-Al_2O_3 catalysts on the conversion for CDRM (Reaction conditions: Cat., 0.2 g; T, 973 K; P, 0.1 MPa; reaction time, 8 h; feed gas, $CH_4/CO_2/Ar$=44.0/47.2/8.8, 40 ml min^{-1}).

Fig. 1.3 showed that the CH_4, CO_2, and total carbon conversion decreased with La loading increasing from 0% to 3%, and did not clearly change with La loading increasing from 3% to 9%. However, the carbon deposition on the 10%Ni/La_2O_3-γ-Al_2O_3 catalyst decreased with increased La loading, while the carbon deposition did not

clearly change with La loading increasing from 3% to 9% in the Fig. 1.4. It is notable that the carbon deposition on 10%Ni/3%La_2O_3-γ-Al_2O_3 catalyst decreased 50% compared with that of 10%Ni/γ-Al_2O_3 catalyst at the same reaction conditions. It was favorable to improve 10%Ni/γ-Al_2O_3 with La loading of 3%.

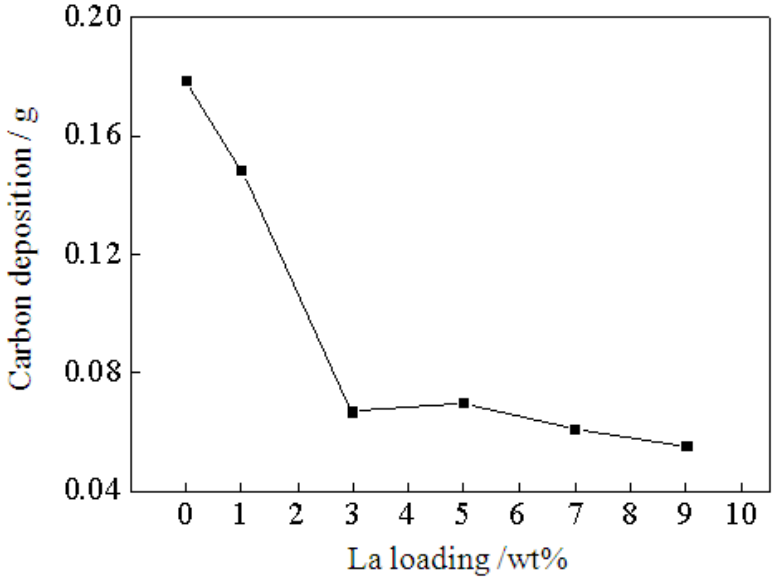

Fig. 1.4. Influence of the La loading in 10%Ni/La_2O_3-γ-Al_2O_3 catalysts on carbon deposition for CDRM (Reaction conditions: Cat., 0.2 g; T, 973 K; P, 0.1 MPa; reaction time, 8 h; feed gas, CH_4/CO_2/Ar=44.0/47.2/8.8, 40 ml min^{-1}).

1.3.3 Influence of impregnation order on the properties of 10%Ni/3%La_2O_3-γ- Al_2O_3 catalyst

Fig. 1.5 was the reaction results of CDMR at 973 K and atmospheric pressure for 8 h by using the 10%Ni/3%La_2O_3-γ-Al_2O_3 catalysts prepared by different impregnation order, whose precursors were calcined at 773 K for 2 h, and reduced in situ by H_2 at 773 K for 1 h.

Fig. 1.5 showed that the CH_4, CO_2, and total carbon conversion were higher, and the carbon deposition was less on the catalyst prepared by co-impregnation method than

those on other catalysts prepared by sequential impregnation method. Although the CH_4, CO_2, and total carbon conversion were higher, the carbon deposition was higher also on the catalyst prepared by impregnating nickel at first, and then impregnating lanthanum. Furthermore, the CH_4, CO_2, and total carbon conversion were lower although the carbon deposition was less on the catalyst prepared by impregnating lanthanum at first, and then impregnating nickel than those on other catalysts. Therefore, the catalysts were prepared by the co-impregnation method in this study.

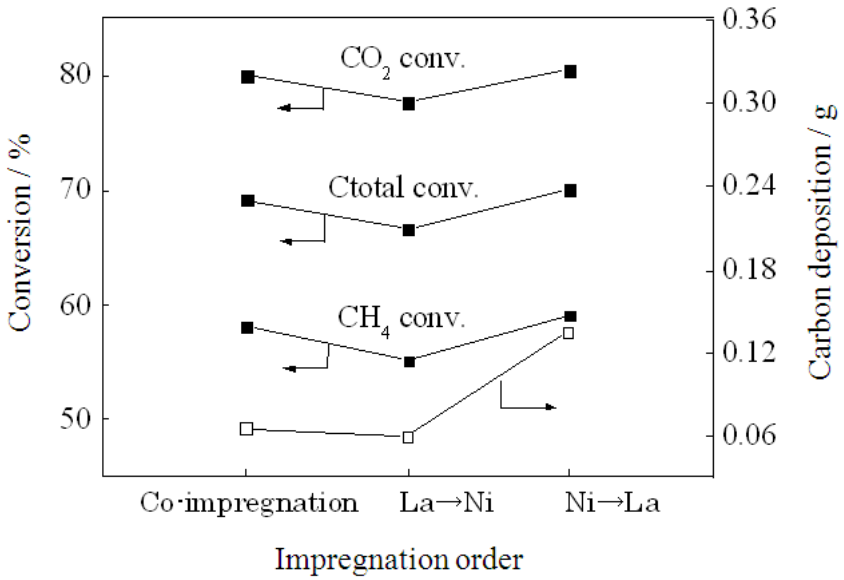

Fig. 1.5. Influence of impregnation order preparing 10%Ni/3%La_2O_3-γ-Al_2O_3 catalyst on the conversion and carbon deposition for CDRM (Reaction conditions: Cat., 0.2 g; T, 973 K; P, 0.1 MPa; reaction time, 8 h; feed gas, $CH_4/CO_2/Ar$=44.0/47.2/8.8, 40 ml min^{-1}).

1.3.4 Influence of temperature on the reaction by using 10%Ni/3%La_2O_3-γ-Al_2O_3 catalysts

Because the CO_2 reforming reaction of CH_4 was an endothermic reaction (ΔH_{298} =+247 kJ mol^{-1}). It is favorable to conduct this reaction at higher reaction temperature. The CO_2 reforming reaction of CH_4 proceeded on the 10%Ni/3%La_2O_3-γ-Al_2O_3

catalysts at different reaction temperature and atmospheric pressure for 8 h. The results of the reaction were showed in the Table 1.2.

The results in the Table 1.2 showed that the CH_4, CO_2, total carbon conversion arose, and CO yield as well as the ratio of H_2/CO enhanced with the reaction temperature increasing. It is notable that the amount of carbon deposition decreased with the reaction temperature increasing. Because more CO_2 reacted with the carbon deposition at higher temperature, i.e. $CO_2 + C \rightarrow 2CO$, the CO_2 conversion was as high as 96.86 %, the CO_2 played a key role for elimination of carbon deposition at higher temperature.

Table 1.2 Influence of temperature on the reaction by using 10%Ni/3%La_2O_3-γ-Al_2O_3 catalysts[a]

Catalyst	T / K	Conversion / %			CO Yield / %	H_2/CO	Carbon deposition/g [c]
		CH_4	CO_2	C_{total}			
3%La_2O_3-M [b]	973	58.12	80.02	69.27	31.20	0.91	0.0667
	1073	76.97	96.86	87.16	32.40	1.16	0.0535

[a] Reaction conditions: Cat., 0.2 g; P, 0.1 MPa; reaction time, 8 h; feed gas, $CH_4/CO_2/Ar$= 44.0/47.2/8.8, 40 ml min^{-1}; [b] M means 10%Ni/γ-Al_2O_3.; [c] Determined by TG, unit is g/0.2g cat.

1.3.5 Influence of La_2O_3-CeO_2 binary promoters on the properties of the Ni based catalysts

To further reduce the amount of carbon deposition and enhance the CH_4, CO_2, and total carbon conversion, CeO_2 was introduced into 10%Ni/3%La_2O_3-γ-Al_2O_3 catalyst, by the same co-impregnation method, to obtain the Ni based catalyst with La_2O_3-CeO_2 binary promoters. Table 1.3 and Fig. 1.6 showed influence of cerium loading on the properties and carbon deposition for 10%Ni/CeO_2-3%La_2O_3-γ-Al_2O_3 catalyst in the CDRM at 1073 K and atmospheric pressure for 8 h.

Table 1.3 Influence of Ce loading on the properties of 10%Ni/CeO_2-3%La_2O_3-γ-Al_2O_3 catalyst [a]

Catalyst	Coversion / %			CO		H_2/CO
	CH_4	CO_2	C_{Total}	Selectivity / %	Yield / %	
3%La_2O_3-M [b]	76.97	96.86	87.16	38.47	32.40	1.16
1%CeO_2-3%La_2O_3-M	76.79	97.15	87.24	36.76	31.82	1.01
3%CeO_2-3%La_2O_3-M	77.27	97.05	87.41	48.65	42.41	1.09
5%CeO_2-3%La_2O_3-M	77.17	96.80	87.02	45.92	39.95	1.15
7%CeO_2-3%La_2O_3-M	77.09	96.04	86.30	41.62	35.90	1.19

[a] Reaction conditions: Cat., 0.2 g; T, 1073K; P, 0.1 MPa; reaction time, 8 h; feed gas, CH_4/CO_2/Ar=44.0/47.2/8.8, 40 ml min^{-1}; [b] M means 10%Ni/γ-Al_2O_3.

Table 1.3 indicated that the CH_4, CO_2, the total carbon conversion, the CO selectivity and the yield increased with the cerium loading increasing from 0 to 3%, and the CH_4, CO_2, the total carbon conversion, CO selectivity and the yield were the highest when the cerium loading was 3%, and then decreased with the cerium loading further increasing from 3% to 7%. The ratio of H_2/CO was around 1 even using 10%Ni/CeO_2-3%La_2O_3-γ-Al_2O_3 catalyst with different cerium loading in the reaction. Fig. 1.6 showed that the amount of the carbon deposition on 10%Ni/CeO_2-3%La_2O_3-γ-Al_2O_3 catalyst decreased with the cerium loading increasing, and the amount of the carbon deposition was the lowest when the cerium loading was 3%. This might be due to the redox property of ceria to prevent the carbon deposition. Consequently, the 10%Ni/ CeO_2-3%La_2O_3-γ-Al_2O_3 catalyst with 3% cerium loading was favorable for the CDRM. The CH_4, CO_2, and total carbon conversion reached 77.27%, 97.05%, and 87.41% respectively, while CO selectivity and yield reached 48.65% and 42.41%, with the H_2/CO in the products close to 1. And the amount of the carbon deposition was 0.0349 g / 0.2 g catalyst after the CO_2 reforming reaction of CH_4 for 8 h by using 10%Ni/3%CeO_2-3%La_2O_3-γ-Al_2O_3 catalyst at 1073K and atmospheric pressure.

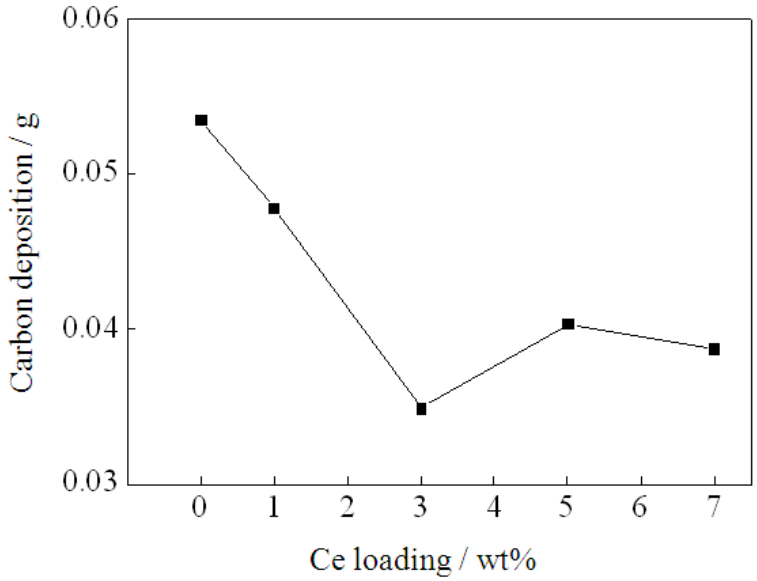

Fig. 1.6. Influence of Ce loading in 10%Ni/CeO_2-3%La_2O_3-γ-Al_2O_3 catalyst on carbon deposition for CDRM (Reaction conditions: Cat., 0.2 g; T, 1073 K; P, 0.1 MPa; reaction time, 8 h; feed gas, CH_4/CO_2/Ar=44.0/47.2/8.8, 40 ml min^{-1}).

According to the findings above, the reaction results of the CDRM on the Ni based catalysts with different promoters were summarized in Table 1.4. Fig. 1.7 was the variations of total carbon conversions with time on stream for CDRM at 1073 K and atmospheric pressure for 8 h by using these Ni based catalysts.

Table 1.4 showed that not only the amount of carbon deposition was suppressed, but also the activity was enhanced slightly by using the catalyst with the La_2O_3 and the CeO_2 binary promoters, compared with other catalysts in the CDRM. The amount of carbon deposition on the 10%Ni/3%CeO_2-3%La_2O_3-γ-Al_2O_3 catalyst were reduced 76.2 % compared with the 10%Ni/γ-Al_2O_3 catalyst. The results in Fig. 1.7 showed that the total carbon conversion on 10%Ni/γ-Al_2O_3 catalyst decreased rapidly with the reaction time, whereas the total carbon conversion on 10%Ni/3%La_2O_3-γ-Al_2O_3 catalyst almost did not change after 2 h, and the total carbon conversion on 10%Ni/3%CeO_2-3%La_2O_3-γ-Al_2O_3 catalyst almost kept stable through the test duration.

Table 1.4 Influence of the promoter on the performances of Ni based catalysts [a]

Catalysts	Conversion / %			CO		H_2/CO	Carbon deposition/g [c]
	CH_4	CO_2	C_{total}	Selectivity/%	Yield/%		
M [b]	78.20	96.29	87.49	47.79	42.04	1.06	0.1466
3% La_2O_3-M	76.97	96.86	87.16	38.47	32.40	1.16	0.0535
3%CeO_2-3%La_2O_3-M	77.27	97.05	87.41	48.65	42.41	1.09	0.0349

[a] Reaction conditions: Cat., 0.2g; T, 1073K; P, 0.1MPa; reaction time, 8 h; feed gas, $CH_4/CO_2/Ar$=44.0/47.2/8.8, 40ml min^{-1}; [b] M means 10%Ni/γ-Al_2O_3; [c] Determined by TG, unit is g/0.2g cat.

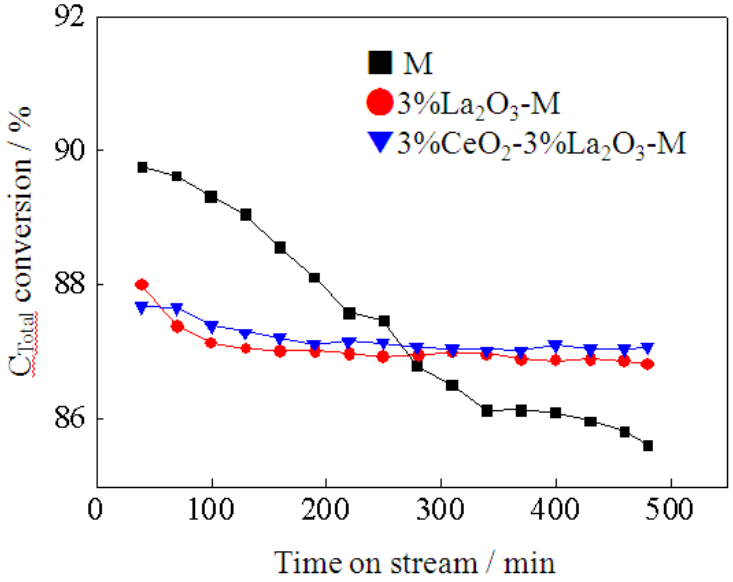

Fig. 1.7. Variations of total carbon conversions with reaction time for the continuous reaction of the CO_2 reforming of CH_4. (M means 10%Ni/γ-Al_2O_3; Reaction conditions: Cat., 0.2 g; T, 1073 K; P, 0.1 MPa; reaction time, 8 h; feed gas, $CH_4/CO_2/Ar$=44.0/47.2/8.8, 40 ml min^{-1}).

The results above indicated that CeO_2-La_2O_3 dual promoter not only enhanced the activity of the Ni based catalyst, but also improved the stability of the catalyst as well as the performance to prevent carbon deposition. The 10%Ni/3%CeO_2-3%La_2O_3- γ-Al_2O_3 catalyst was favorable for the CO_2 reforming of CH_4, and syngas with H_2/CO ratio near to 1 was obtained at 800 ^oC and atmospheric pressure.

1.3.6 XRD analysis

Fig. 1.8 exhibited XRD patterns of the catalysts calcined at 773 K. The peaks at the

diffraction angle 37.3, 43.3˚, 62.9˚ and 75.4˚ were the peaks of the NiO phase [28-30]. The peaks intensity of the NiO phase was weaker in the 10%NiO/3%La_2O_3- γ-Al_2O_3 and 10%NiO/3%CeO_2-3%La_2O_3-γ-Al_2O_3 catalysts than those in the 10%NiO/γ-Al_2O_3 catalysts. This might be due to the fact that the dispersion of the NiO species became more homogeneous and higher by the promoters La_2O_3 and CeO_2. And the particle diameter of the NiO was smaller in the 10%NiO/3%La_2O_3-γ-Al_2O_3 and 10%NiO/3%CeO_2-3%La_2O_3-γ-Al_2O_3 catalysts than those in the 10%NiO/γ-Al_2O_3 catalysts. The peaks at the diffraction angle around 37.1˚, 45.7˚and 67˚ were the peaks of the γ-Al_2O_3 phase [28,29]. The nickel aluminate ($NiAl_2O_4$, spinel) phase might be also in these catalysts formed by the reaction of the Al_2O_3 with NiO as follow: NiO + Al_2O_3 → $NiAl_2O_4$. Due to the peak broadening and superimposition of γ-Al_2O_3 and $NiAl_2O_4$ phases, it is difficult to clearly distinguish γ-Al_2O_3 and $NiAl_2O_4$ phases by means of XRD [28,29]. It is notable that the formation of the spinel phase in the NiO-Al_2O_3 based catalysts is related to the calcination temperature of the catalysts. The higher the calcination temperature, the larger the fraction of Ni^{2+} ions converted into spinel. This conversion was practically complete for a calcination temperature of 1023 K [30]. Because the calcination temperature of the catalysts in this study was only 773 K, the amounts of the spinel was limited in all Ni based catalysts. The peaks at diffraction angle 28.5˚, 33.0˚ and 56.3˚ were the CeO_2 phase in the 10%NiO/3%CeO_2-3%La_2O_3-γ-Al_2O_3 catalyst. The lanthanum-containing phase was not detected in the catalysts loaded lanthanum, probably due to their high dispersion and low crystallinity.

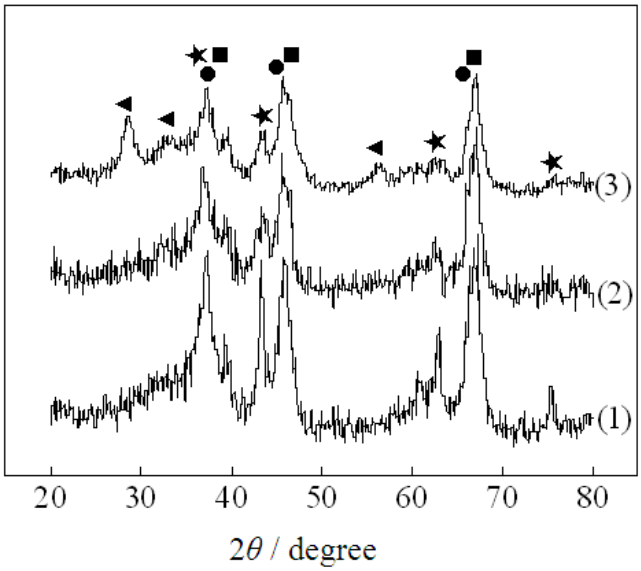

Fig. 1.8. XRD patterns of samples calcined (★NiO ■γ-Al_2O_3 ●$NiAl_2O_4$ ◄CeO_2).
(1)10%NiO/γ-Al_2O_3 (2)10%NiO/3%La_2O_3-γ-Al_2O_3 (3)10%NiO/3%CeO_2-3%La_2O_3-γ-Al_2O_3.

1.3.7 TPR analysis

Fig. 1.9 was TPR patterns of the Ni based catalysts calcined at 773 K. The TPR results showed that nickel species in the catalysts were reduced in the temperature range between 673 and 873 K. The reduction temperature (at the maximum peak) for "free" NiO was at 600 K or higher [30], depending on the preparation method and conditions. The reduction temperature (at the maximum peak) for NiO in the 10%Ni/γ-Al_2O_3 was increased to 788 K due to stronger interaction between NiO and Al_2O_3 species. The reduction temperature (at the maximum peak) for NiO in three catalysts was almost same, but the shape of the reduction peak (at the maximum peak) was broader for 10%Ni/3%La_2O_3-γ-Al_2O_3 and 10%Ni/3%CeO_2-3%La_2O_3-γ-Al_2O_3 than that for 10%Ni/γ-Al_2O_3, and a shoulder at about 820 K arose for 10%Ni/3%La_2O_3-γ-Al_2O_3 and 10%Ni/3%CeO_2-3%La_2O_3-γ-Al_2O_3. This was probably due to the different interaction between NiO and Al_2O_3, La_2O_3 or CeO_2, resulting in different state of the NiO species

in the catalysts with La_2O_3 and CeO_2 promoters, and more Ni^{2+} presence in the surface phase containing Ni, Al, and La or Ce, in which interaction was more stronger due to the increase of the polarization effect of the ions in the surface, making reduction more difficult in the 10%Ni/3%La_2O_3-γ-Al_2O_3 and 10%Ni/3%CeO_2-3%La_2O_3-γ-Al_2O_3 [29,31,32]. The reduction peak of the spinel ($NiAl_2O_4$) was not observed at higher reduction temperature than 873 K because the catalysts were calcined at lower temperature of 773 K, and there was almost no spinel phase in the catalysts [30]. All analysis showed that the results of TPR were consistent with that of XRD.

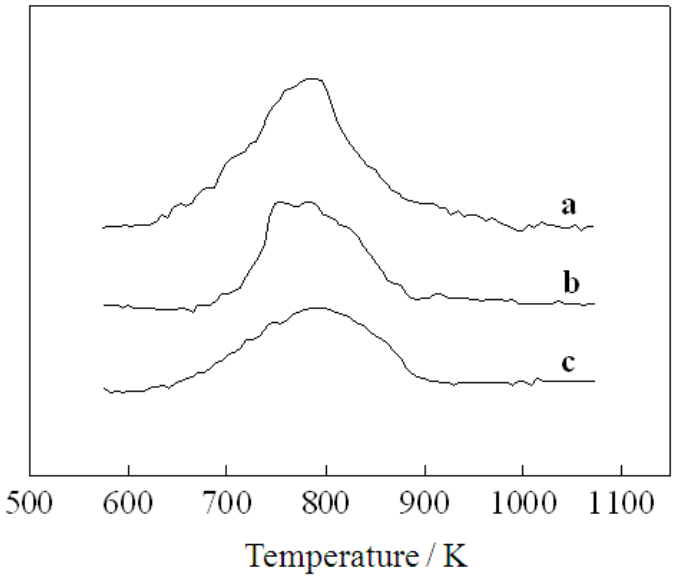

Fig. 1.9. TPR patterns of the catalysts. a. 10%Ni/γ-Al_2O_3, b. 10%Ni/3%La_2O_3-γ-Al_2O_3, c. 10%Ni/3%CeO_2-3%La_2O_3-γ-Al_2O_3.

It is believed that Ni^0 is the active component both for the steam-reforming and for the carbon dioxide-reforming reactions [33]. Because the reduction temperature and time for 10%Ni/3%La_2O_3-γ-Al_2O_3 and 10%Ni/3%CeO_2-3%La_2O_3-γ-Al_2O_3 catalysts were the same as 10%Ni/γ-Al_2O_3 catalyst, thus the reducibility was different for three

catalysts, and the reducibility for 10%Ni/3%La_2O_3-γ-Al_2O_3 and 10%Ni/3%CeO_2-3%La_2O_3-γ-Al_2O_3 catalysts was lower than that for the 10%Ni/γ-Al_2O_3 catalyst. Therefore, the initial activities of the 10%Ni/3%La_2O_3-γ-Al_2O_3 catalyst and the 10%Ni/3%CeO_2-3%La_2O_3-γ-Al_2O_3 catalyst was lower than that of 10%Ni/γ-Al_2O_3 catalyst as in Fig. 1.7.

1.3.8 TG-DTA analysis

The TG-DTA analysis of the 8 h spent catalyst samples in the CO_2 reforming of CH_4 at 1073 K and atmospheric pressure were indicated in Fig. 1.10. There were two exothermic peaks at 857 K and 925 K for 10%Ni/γ-Al_2O_3 sample, and one exothermic peak at 853 K for 10%Ni/3%La_2O_3-γ-Al_2O_3 sample, and one broader exothermic peak at 762-830 K for 10%Ni/3%CeO_2-3%La_2O_3-γ-Al_2O_3 sample in the DTA curves. The exothermic peak shifted gradually to low temperature and peak area decreased gradually if loading La_2O_3 and CeO_2 into the Ni/γ-Al_2O_3 catalysts. These findings indicated that different carbon deposition species on these catalysts were oxidized, and the carbon deposition species on the 10%Ni/γ-Al_2O_3 with La_2O_3 and CeO_2 promoters were more easily oxidized than that on the 10%Ni/γ-Al_2O_3 catalyst, thus temperature of the exothermic peaks for the carbon deposition oxidation on the 10%Ni/γ-Al_2O_3 with La_2O_3 and CeO_2 promoters was lower than that on the 10%Ni/γ-Al_2O_3 catalyst.

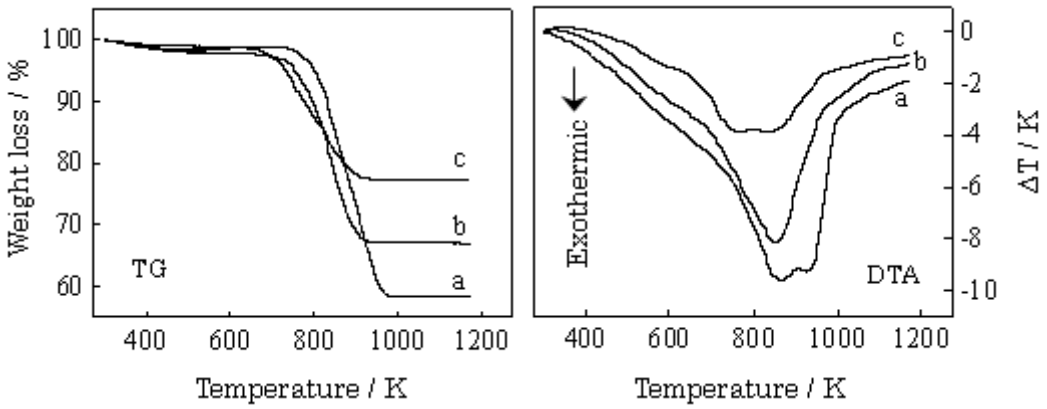

Fig. 1.10. TG-DTA analysis of the 8 h spent catalyst samples. (a. 10%Ni/γ-Al_2O_3, b. 10%Ni/3%La_2O_3-γ-Al_2O_3, c. 10%Ni/3%CeO_2-3%La_2O_3-γ-Al_2O_3).

TG analysis showed that weight losses were about 41%, 31% and 21% for the10%Ni/γ-Al_2O_3, 10%Ni/3%La_2O_3-γ-Al_2O_3 and 10%Ni/3%CeO_2-3%La_2O_3-γ-Al_2O_3 catalysts, respectively, indicating a significant amount of carbon deposition on the 10%Ni/γ-Al_2O_3, and smallest amount of carbon deposition on the 10%Ni/3%CeO_2-3%La_2O_3-γ-Al_2O_3 catalyst after the reaction for 8 h.

Carbon deposition could be formed on the catalysts in different ways, depending on the reaction conditions and the property of catalyst. In principle, the amount of carbon deposition formed should depend on the nickel quantity present at the catalyst surface and its particle size. On alumina, pyrolytic carbon is produced, depending on the surface acidity and the components of the support [29,34].

La_2O_3 actually played dual roles in preventing the carbon deposition for the CO_2 reforming of CH_4. On one hand, addition of La_2O_3 could decrease the acidity of the support, thereby stop pyrolytic carbon formation, and the basic La_2O_3 favored the chemisorption and dissociation of CO_2 and subsequently accelerated the carbon elimination by $CO_2 + C = 2CO$. On the other hand, the La_2O_3 dispersed in the Al_2O_3 and Ni crystallites could prevent the Ni grains from excessive growth at high temperatures.

CeO_2 as a promoter influenced Ni/γ-Al_2O_3 used for CO_2 reforming of CH_4 in two respects. Firstly, the addition of CeO_2 to Ni/γ-Al_2O_3 could improve the Ni dispersion; secondly, there was an electronic interaction between CeO_2 and Ni, where CeO_2 could increase the *d*-electron density of Ni atoms. The electron-rich character of the Ni atoms naturally inhibited the cracking of CH_4 [28,35,36]. In addition, because CeO_2 is basic, it was favorable to adsorb CO_2 and so eliminate the carbon deposition.

1.3.9 SEM analysis

Fig. 1.11 showed SEM images of 10%Ni/γ-Al_2O_3 catalyst (Fig.11 a, b), and 10%Ni/3%CeO_2-3%La_2O_3-γ-Al_2O_3 catalyst (Fig. 11 c, d) before and after the reforming reaction for 8 h at 1073K and atmospheric pressure.

Kim et al reported that in the reforming reaction, the deposition of carbon could occur on Ni particles in the various forms of carbon such as adsorbed atomic carbon, amorphous carbon, bulk Ni carbide and crystalline graphitic carbon, and types of carbon deposition depended on metal particle size and the components of the catalyst [37]. Matsukata reported that the morphology of graphitic carbon was carbon filaments, and the morphology of amorphous carbon was moss-like amorphous carbon encapsulating Ni particles [38]. The filamentous carbon could be readily eliminated by gasification with CO_2, and while the carbon with a moss-like morphology could hardly be eliminated by gasification with CO_2, and this type of carbon encapsulated Ni particles, leading to the deactivation of the Ni based catalyst [37,38].

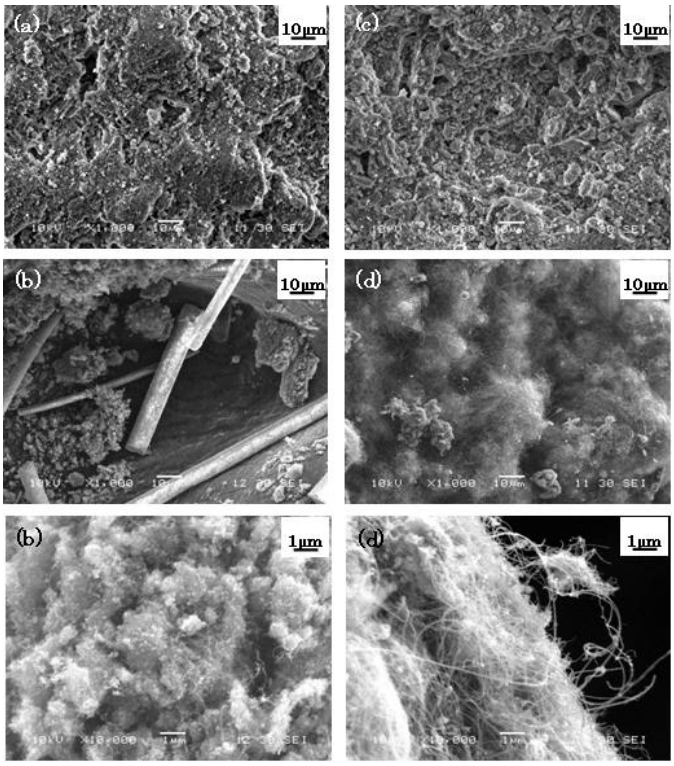

Fig. 1.11. SEM micrographs of the catalysts before and after reaction for 8 h at 1073 K. (a,b, before and after reaction on 10%Ni/γ-Al_2O_3; c,d, before and after reaction on 10%Ni/3%CeO_2-3%La_2O_3-γ-Al_2O_3, b,d has 10μm scale and 1μm scale images).

Fig. 1.11 showed that the substantial amount of carbon deposition was formed on the two spent 10%Ni/γ-Al_2O_3 and 10%Ni/3%CeO_2-3%La_2O_3-γ-Al_2O_3 catalysts during the CO_2 reforming of CH_4. Two different types of carbonaceous species, the moss-like amorphous carbon and filamentous carbon, were observed on the catalysts by SEM. The moss-like carbon was dominantly formed on the 10%Ni/γ-Al_2O_3 catalyst in Fig. 1.11 b. The moss-like carbon could hardly be gasified with CO_2 and it encapsulated Ni particles, deactivating catalyst. Furthermore, the rod-shaped species in Fig. 1.11 b should be Ni particles formed by sintering and encapsulated by the moss-like amorphous carbon. A part of filamentous carbon was also observed on the 10%Ni/γ-Al_2O_3 catalyst in Fig. 1.11 b. The filamentous carbon was mainly observed on the 10%Ni/3%CeO_2-3%La_2O_3-

γ-Al_2O_3 catalysts in Fig. 1.11 d, octopus–like carbon where some carbon filaments grew from one Ni particle was also observed. Although a large amount of filamentous carbon was formed on the 10%Ni/3%CeO_2-3%La_2O_3-γ-Al_2O_3 catalysts, it was reported that there had a hollow inner channel inside a lot of thin filamentous carbon [39] and reactive filamentous carbon species could be eliminated readily, and hence catalyst deactivation by blocking the catalytic active sites by deposited carbon was greatly hindered. Because of the difficulty in the sintering of Ni particles and of the dominant formation of the reactive filamentous carbon by adding La_2O_3 and CeO_2 promoters in Ni based catalyst, 10%Ni/3%CeO_2-3%La_2O_3-γ-Al_2O_3 catalysts showed stable activity in the continuous CO_2 reforming reaction of CH_4.

1.4 Conclusions

The CO_2 reforming reaction of CH_4 was investigated by using different Ni based catalysts prepared by co-impregnation method. The properties of the catalysts and the carbon deposition performance on the catalyst surface were surveyed by XRD, TPR, TG-DTA, and SEM. The results showed that the activity of the Ni/γ-Al_2O_3 catalyst with Ni loading of 10% was higher than those with other Ni loading. However, the Ni/γ-Al_2O_3 catalyst was not stable in the continuous reaction of the CO_2 reforming of CH_4 due to a large amount of carbon deposition on the catalyst surface. Although the activity of Ni/γ-Al_2O_3 catalyst with the La_2O_3 as promoter was not obviously increased, the carbon deposition on 10%Ni/3%La_2O_3-γ-Al_2O_3 catalyst decreased to one-third that of 10%Ni/γ-Al_2O_3 catalyst at the same reaction conditions due to alkaline function and dispersion promotion role of La_2O_3. Not only the amount of carbon deposition was decreased, but also the activity was also improved slightly by using the Ni/γ-Al_2O_3 with

the La_2O_3-CeO_2 binary promoters, due to alkaline function and dispersion action of La_2O_3-CeO_2, as well as electronic interaction between CeO_2 and Ni.

The results of SEM showed that the moss-like carbon on the 10%Ni/γ-Al_2O_3 catalyst could hardly be gasified with CO_2, and encapsulated Ni particles, but the filamentous carbon on the 10%Ni/3%CeO_2-3%La_2O_3-γ-Al_2O_3 catalysts could be eliminated readily. Because of suppressing the sintering of Ni particles and the formation of the reactive filamentous carbon on the Ni based catalyst added by La_2O_3 and CeO_2 promoters, 10%Ni/3%CeO_2-3%La_2O_3-γ-Al_2O_3 catalyst showed stable activity.

References

[1] S. Wang, G.Q.M. Lu, G.J. Millar, ***Energy Fuels*** 10 (1996) 896-904.

[2] N. Laosiripojana, S. Assabumrungrat, ***J. Power Sources*** 163 (2007) 943-951.

[3] Y.X. Pan, C.J. Liu, P. Shi, J. ***Power Sources*** 176 (2008) 46-53.

[4] F. Pompeo, N.N. Nichio, M.M.V.M. Souza, D.V. Cesar, O.A. Ferretti, M. Schmal, ***Appl. Catal. A Gen.*** 316 (2007) 175-183.

[5] S.H. Lee, W. Cho, W.S. Ju, B.H. Cho, Y.C. Lee, Y.S. Baek, ***Catal. Today*** 87 (2003) 133-137.

[6] Y.G. Chen, K. Tomishige, K. Yokoyama, K. Fujimoto, ***J. Catal.*** 184 (1999) 479-490.

[7] Y.G. Chen, O. Yamazaki, K. Tomishige, K. Fujimoto, ***Catal. Lett.*** 39 (1996) 91-95.

[8] O. Yamazaki, K. Tomishige, K. Fujimoto, ***Appl. Catal., A Gen.*** 136 (1996) 49-56.

[9] K. Tomishige, O. Yamazaki, Y. Chen, K. Yokoyama, X. Li, K. Fujimoto, ***Catal. Today*** 45 (1998) 35-39.

[10] K. Tomishige, O. Yamazaki, Y. Chen, K. Yokoyama, X. Li, K. Fujimoto, ***Catal. Today*** 45 (1998) 35-39.

[11] J.F. Munera, S. Irusta, L.M. Cornaglia, E.A. Lombardo, D.V. Cesar, M. Schmal, ***J. Catal.*** 245 (2007) 25-34.

[12] A.M. Gadalla, B. Bower, ***Chem. Eng. Sci.*** 43 (1988) 3049-3062.

[13] J.R.H. Ross, ***Catal. Today*** 100 (2005) 151-158.

[14] M.C.J. Bradford, M.A. Vannice, ***Appl. Catal. A Gen.*** 142 (1996) 73-96.

[15] J.B. Wang, S.Z. Hsiao, T.J. Huang, ***Appl. Catal. A Gen.*** 246 (2003) 197-211.

[16] T. Takeguchi, S.N. Furukawa, M. Inoue, K. Eguchi, ***Appl. Catal. A Gen.*** 240 (2003) 223-233.

[17] J.B. Wang, Y.L. Tai, W.P. Dow, T.J. Huang, ***Appl. Catal. A Gen.*** 218 (2001) 69-79.

[18] W.P. Dow, Y.P. Wang, T.J. Huang, ***J. Catal.*** 160 (1996) 155-170.

[19] W.P. Dow, T.J. Huang, ***J. Catal.*** 160 (1996) 171-182.

[20] H.C. Yao, Y.F.Y. Yao, ***J. Catal.*** 86 (1984) 254-265.

[21] J. Soria, J.M. Coronado, J.C. Conesa, ***J. Chem. Soc., Faraday Trans.*** 92 (1996) 1619-1626.

[22] C. Morterra, V. Bolis, G. Magnacca, ***J. Chem. Soc., Faraday Trans.*** 92 (1996) 1991-1999.

[23] Z.X. Cheng, Q.L. Wu, J.L. Li, Q.M. Zhu, ***Catal. Today*** 30 (1996) 147-155.

[24] S.B. Wang, G.Q. Lu, ***Appl. Catal. B Environ.*** 19 (1998) 267-277.

[25] Zhang, Z. L.; Verykios, X. E. ***J. Chem. Soc., Chem. Commun.*** (1995) 71-72.

[26] Z.L Zhang, X.E. Verykios, ***Catal. Lett.*** 38 (1996) 175-179.

[27] Z. Zhang, X.E. Verykios, S.M. MacDonald, S. Affrossman, ***J. Phys. Chem.*** 100 (1996)744-754.

[28] J. Chen, R. Wang, J. Zhang. F. He, S. Han, ***J. Mol. Catal. A Chem.*** 235 (2005) 302-310.

[29] R. Martinez, E. Romero, C. Guimon, R. Bilbao, ***Appl. Catal. A Gen.*** 274 (2004) 139-149.

[30] J.M. Rynkowski, T. Paryjczak, M. Lenik, ***Appl. Catal. A Gen.*** 106 (1993) 73-82.

[31] B. Scheffer, P. Molhoek, J.A. Moulijn, ***Appl. Catal.*** 46 (1989) 11-30.

[32] P. Arnoldy, J.A. Moulijn, ***J. Catal.*** 93 (1985) 38-54.

[33] R. Blom, I.M. Dahl, A. Slagtem, ***Catal. Today*** 21 (1994) 535-543.

[34] T. Horiuchi, H. Hidaka, T. Fukui, Y. Kubo, M. Horio, K. Suzuki, T. Mori, ***Appl. Catal. A Gen.*** 167 (1998) 195-202.

[35] G.L. Xu, K.Y. Shi, Y. Gao, H. Xu, Y. Wei, ***J. Mol. Catal. A Chem.*** 147 (1999) 47-54.

[36] Y.L. Yang, W.Z. Li, H.Y. Xu, ***React Kinet Catal. Lett.*** 77 (2002) 155-162.

[37] J.H. Kim, D.J. Suh, T.J. Park, K.L. Kim, ***Appl. Catal. A Gen.*** 197 (2000) 191-200.

[38] M. Matsukata, T. Matsushita, K. Ueyama, ***Energy Fuels*** 9 (1995) 822-828.

[39] Y.G. Chen, J. Ren, ***Catal. Lett.*** 29 (1994) 39-48.

Chapter 2 Carbon nanotubes metallic catalyst

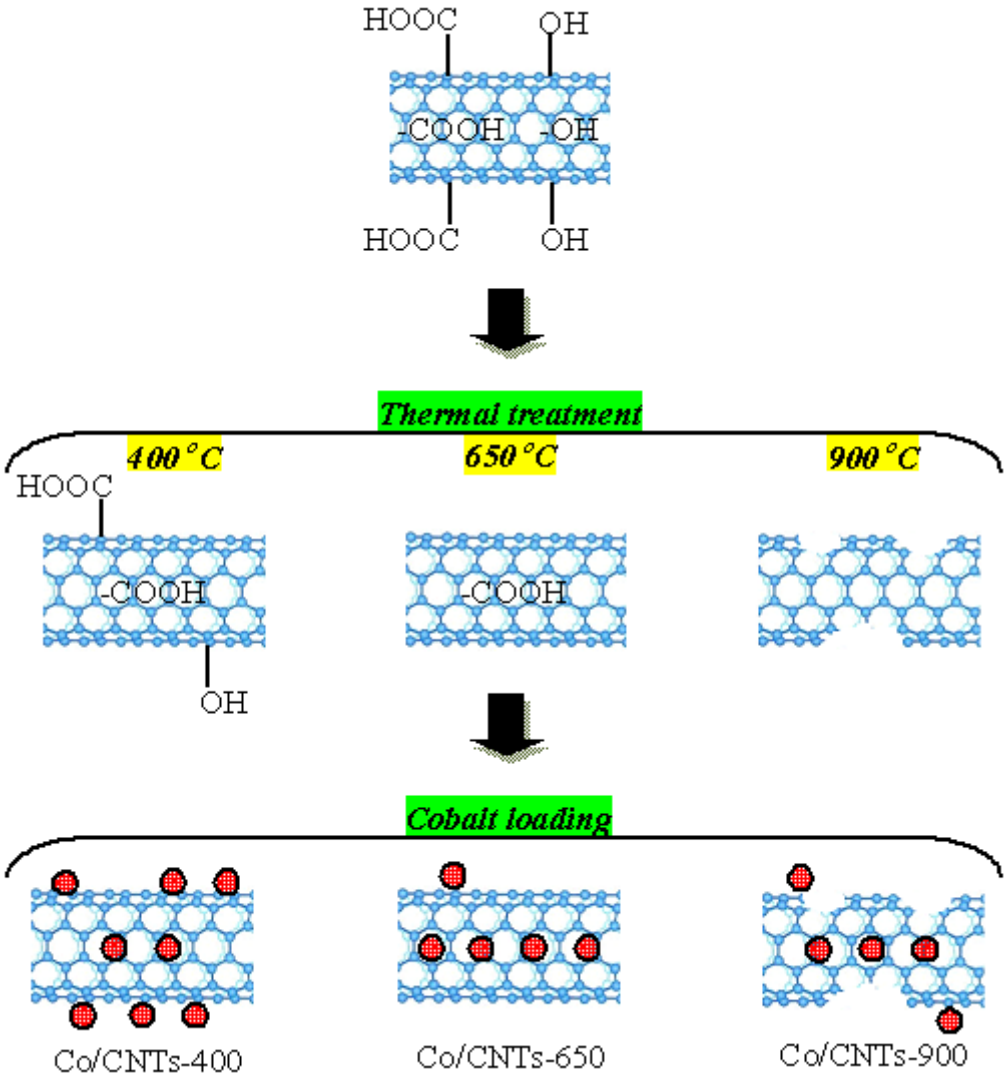

Abstract

By using the combination of concentrated nitric acid refluxing, varied thermal treatment and wetness impregnation method on carbon nanotubes (CNTs), we realized the controllable encapsulation of cobalt clusters inside the channels of CNTs. The analysis results by TPD and TEM on the prepared cartalysts indicated that the controllable encapsulation of cobalt clusters in CNTs channels was realized more readily by controlling the thermal treatment on pristine CNTs support at different temperature. For the Co/CNTs-650 catalyst employing thermal treated CNTs at 650 ^{o}C, the cobalt nanoparticles inside the CNTs channel reached up to 80 % with the particles size of 5-10 nm. The thermal treatment on the pristine CNTs support at this optimized temperature effectively removed the oxygen-containing functional groups on the surface of CNTs, simultaneously keeping the integrity of CNTs walls. The influence of varied thermal treatment of the CNTs support to the catalytic performance of the final Co/CNTs catalysts in the Fischer-Tropsch synthesis (FTS) was investigated. The FTS reaction results on the Co/CNTs-650 catalyst showed both the best CO conversion of 89.3 % and the highest C_{5+} hydrocarbon selectivity of 83.7 %, at the same time holding the lowest CH_4 selectivity of only 8.4 % among all the tested FTS catalysts.

Keywords: Fischer-Tropsch Synthesis, Carbon Nanotubes, Cobalt, Encapsulation.

2.1 Introduction

Fischer-Tropsch synthesis (FTS) is a very promising technology for producing clean synfuel via carbon monoxide hydrogenation. The syngas ($CO + H_2$), as feed gas of FTS, is generated from coal, natural gas and biomass. Syngas had been extensively applied in alcohol synthesis [1], dimethyl ether (DME) synthesis [2] and various FTS process [3-7]. Some metals, like iron, cobalt, nickel and ruthenium, have been applied widely as catalyst for FTS reaction. Practically, the nickel-based FTS catalyst produces too much methane and the ruthenium-based catalyst is too expensive, limiting their use in large-scale industry. Iron is a cost-saving catalyst for FTS reaction, especially in the production of olefins. As we know, besides of the iron-based catalyst, cobalt-based catalyst is also one of the most active metals for the FTS reaction especially at low-severity reaction conditions. In comparison with iron catalyst, the cobalt catalyst exhibits higher activity, higher selectivity to linear hydrocarbons especially paraffin and lower water-gas-shift reaction (WGSR) activity [8].

In FTS process, the catalyst activity and the product selectivity are significantly influenced by the nature, dispersion and loading amount of active metals, as well as the nature and structure of supports [9]. Some common FTS catalysts, like the alumina, silica or titania supported cobalt catalysts, have been investigated widely on their morphology, cobalt particle size and reduction degree [10]. In recent years, some novel carbon materials, such as carbon nanofiber [11], carbon sphere[12], carbon nanotubes [13] and graphene [14], have become the most interested catalyst supports. One of the important reasons using the carbon materials as catalyst support is the weak interaction between the metal phases and the carbon supports, which can lead to high reduction degree and further improve FTS catalyst activity. Carbon nanotubes, since its

unique mechanical, chemical and electrical properties, have been also used as catalyst supports. For instance, it has been reported that iron loaded CNTs as catalyst was used for FTS reaction [15,16]. Due to the space confinement effect offered by the nano-sized channels of CNTs, the metal clusters fixed inside CNTs channels can be reduced more easily and at the same time their aggregation is limited during FTS reaction, consequently determining their better catalytic activity and longer lifetime [17].

Recently, the CNTs supported cobalt catalysts have also been reported [18,19]. However, the reported catalyst preparation methods of these studies are lack of effectively controllable encapsulation of cobalt nanoparticles inside CNTs channel. Furthermore, there are still not the detailed studies on the effect of the distribution of cobalt clusters inside or outside CNTs channels to FTS reaction. In this report, we demonstrate the preparation of a series of cobalt loaded CNTs with the precisely controllable encapsulation cobalt nanoparticles inside CNTs channels by using the combined protocols of concentrated nitric acid refluxing, thermal treatment and the followed incipient wetness approach. These Co/CNTs catalysts and CNTs supports are characterized by temperature programmed desorption, X-ray diffraction, transmission electron microscope and temperature programmed reduction, proving the facilely controllable distribution of cobalt nanoparticles inside or outside CNTs channels. The FTS reaction is performed with these Co/CNTs as catalysts in a fixed-bed reactor. The effect of the distribution of cobalt clusters inside or outside CNTs channels on FTS products is investigated and discussed in detail.

2.2 Experimental

2.2.1 Catalyst preparation

The pristine multi-wall carbon nanotubes (OD = 8-15 nm, Length = 0.5-2 μm) were first refluxed with 65 wt% nitric acid at 120 ^{o}C for 14 h, washed with distilled water until pH = 7, and then dried at 110 ^{o}C over night. After these procedures, the caps of pristine CNTs were opened and cut into segments［17］. The opened CNTs were very favorable for the cobalt-containing liquid to enter the inner channels of the CNTs supports during the followed cobalt loading process. The oxygen-containing groups (such as -C=O, -COOH and -OH) on the outside surface of the HNO_3 treated CNTs can also adsorb metallic ion［20,21］, with which we realize the controllable encapsulation of cobalt clusters inside CNTs channels more facilely.

In order to manipulate the absolute quantity of the oxygen-containing groups on CNTs surface, a thermal treatment procedure on the HNO_3 treated CNTs was designed and performed. Here, the thermal treatment process was performed in a ceramic tube oven with the flowing argon gas at various temperatures (400 ^{o}C, 650 ^{o}C, 900 ^{o}C) for 3 h. And then the 10 wt% cobalt loaded CNTs catalyst was prepared by wetness impregnation method using the cobalt nitrate aqueous solution as source. The wet catalyst precursor was first dried at 120 ^{o}C in air for 10 h, and then calcined at 350 ^{o}C under flowing argon for 3 h. The final CNTs supported cobalt catalyst was denoted as Co/CNTs-x (x = 400, 650, 900), where the“x”means the different temperature of thermal treatment on CNTs. In addition, another catalyst named Co/CNTs-A, as reference catalyst, was also prepared with only nitric acid treated CNTs as support, which was, without further thermal treatment.

2.2.2 Catalyst characterization

The crystalline structure of the sample was confirmed by X-ray diffraction (XRD) pattern with a Rigaku D/max-2550 V diffractometer employing CuKα radiation (λ = 1.54056 Å; scanning rate: 0.02° s^{-1} in the range of 10-80°). Transmission electron microscope (TEM) images of catalysts were obtained with a JEOL JEM-2100 UHR transmission electron microscope operated at 200 kV. Hydrogen temperature programmed reduction (H_2-TPR) analysis of the pretreated supports at varied temperature was conducted on a BELCAT-B-TT (BEL, Japan) instrument. A typical H_2-TPR experiment was carried out in a quartz-made microreactor with a flowed gas of 5%H_2/95%Ar at atmospheric pressure. The sample was first heated to 150 ^oC in flowing He (20 ml/min) for 60 min, followed by cooling to 80 ^oC, and then the 5% H_2 (20 ml/min) passed through the catalyst sample with linearly increased temperature from 80 ^oC to 800 ^oC at a heating rate of 5 ^oC/min. The effluent gas was analyzed by a gas chromatograph with a thermal conductivity detector (TCD). Ammonia temperature programmed desorption (NH_3-TPD) experiments were carried out using the same equipment of TPR studies. Briefly, an amount of 300 mg sample was first purged with He at 150 ^oC for 1 h. And then the sample was cooled down to 80 ^oC under He flow, followed adsorption by using 5%NH_3/95%He with a flowing rate of 20 mL/min. After saturation, the sample was purged again with a flow of He to remove any physically adsorbed ammonia and then temperature was linearly increased from 80 ^oC to 800 ^oC with 5 ^oC/min in He atmosphere for ammonia desorption.

2.2.3 Catalytic activity measurements

FTS reaction was carried out using a flow-type pressurized reactor. The cobalt catalyst of 0.50 g was loaded in the middle of reactor and reduced in situ at 400 ^oC in H_2

for 10 h, and then FTS reaction was implemented at certain reaction conditions. An ice trap with solvent was fixed between reactor and back pressure regulator to capture the heavy hydrocarbons which was finally analyzed by an offline gas chromatograph (Shimadzu GC-2014, FID). The residual gaseous products effused from ice trap were analyzed online by another two gas chromatographs (Shimadzu GC-8A, TCD and Shimadzu GC-14B, FID), respectively. The configuration of the reactor was showed in Scheme 2.1.

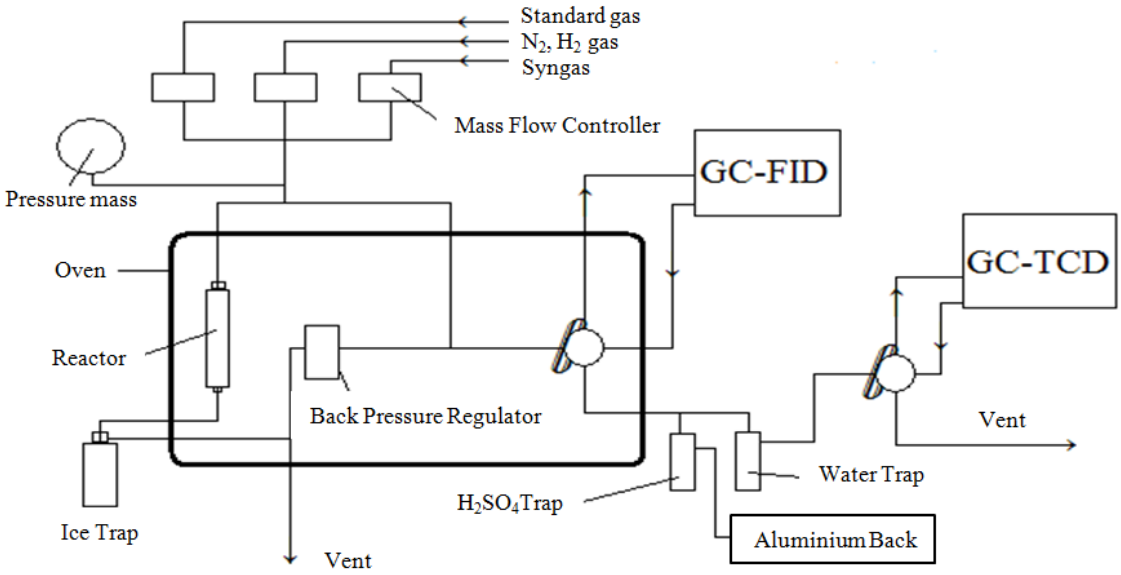

Scheme 2.1. Schematic diagram of FTS reaction

2.3 Results and Discussion

2.3.1 Characterization of catalysts

The textural properties of samples are summarized in Table 2.1. The BET surface area increased from 170 to 223 m^2/g after nitric acid treatment, indicating that then ends of CNTs were opened, at the same time exposed their internal surface area with HNO_3 oxidation. With the increase in the thermal treatment temperature, the BET surface area increased significantly, and the pore volume decreased. However, the total pore volume decreased notably when the temperature increased to 900 ^oC. Table 2.1 also shows the metallic nanoparticles size of Co/CNTs-A, Co/CNTs-400, Co/CNTs-650 and Co/CNTs-900 by TEM images. The increased Co nanoparticles size with the increasing of thermal treatment temperature is attributed to the change of CNTs supported.

Table 2.1 Summary of the textural properties of different samples

Sample	BET Surface area[a] (m^2/g)	Total pore Volume[a] (m^3/g)	Average particle size[b] (nm)
Pristine CNTs	170	1.60	—
CNTs-A	223	0.89	—
CNTs-400	241	0.86	—
CNTs-650	252	0.81	—
CNTs-900	267	0.59	—
Co/CNTs-A	195	0.60	4.0
Co/CNTs-400	213	0.57	3.1
Co/CNTs-650	226	0.50	3.6
Co/CNTs-900	244	0.41	3.9

[a] The surface area was determined by N_2 sorption.

[b] The average sizes of Co nanoparticles were measured from counting and averaging TEM images.

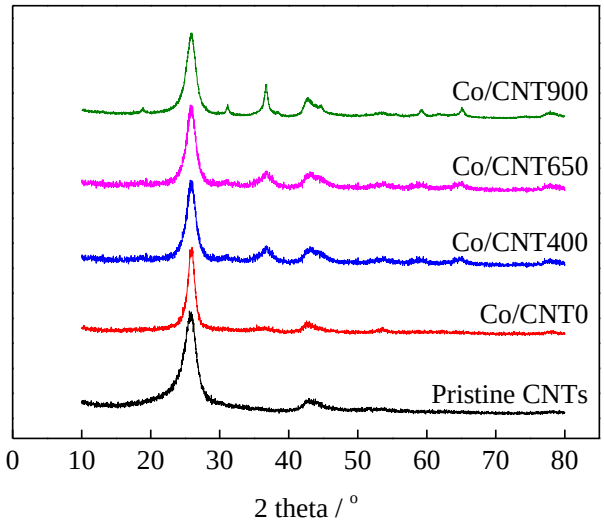

Fig. 2.1. XRD patterns of the samples (a. Pristine CNTs; b. Co/CNTs-A; c. Co/CNTs-400; d. Co/CNTs-650; e. Co/CNTs-900)

X-ray diffraction patterns of the calcined samples, such as pristine CNT, Co/CNTs-A and Co/CNT-x (x = 400, 650, 900), are showed in Fig. 2.1. The main peaks are identified as CNTs and Co_3O_4. The X-ray diffraction patterns show the peaks at 2θ values of 26.3° and 43.0° generally associated with the CNTs support. Other peaks related to the different crystal planes of Co_3O_4 are in good agreement with the previously reported results［22］. However, with the smaller particle size of metal oxide on carbon support, the Co_3O_4 diffraction peaks are slightly weak and wide.

The NH_3-TPD patterns of the CNTs-A and CNTs-x supports are showed in Fig. 2.2b-d respectively. In addition, the TPD of pure CNTs-A sample without adsorbed NH_3, as reference sample, is also tested and presented as Fig. 2.2a. According to this Fig. 2.2a, we can find that the pure support of CNTs-A, with only nitric acid refluxing but no thermal treatment, exhibits the decomposition peaks at 252 ^oC, 440 ^oC and 695 ^oC respectively under He atmosphere. Here, these three peaks are probably due to the

presence of different oxygen-containing groups on the surface of nitric acid treated CNTs. The H_2O peak at about 252 ^oC can be ascribed to the formation of carboxylic anhydrides from carboxyl groups or the dehydration of phenolic hydroxyl [20,23]. The CO_2 peak at about 440 ^oC is attributed to the decomposition of carboxyl or anhydride groups [24]. For the peak at 695 ^oC, it might be assigned to the decomposition of phenol, quinine and ether groups [20]. For NH_3-TPD pattern of the pure CNTs-A (Fig. 2.2b), it exhibits a major NH_3 desorption peak at 201 ^oC, which can be attributed to its weak acidic sites, also being in a good agreement with that report of Wang et al. [25]. However, the NH_3 desorption peak at 201 ^oC can't be observed on the TPD curves of the CNTs-400, CNTs-650 and CNTs-900. It implies that the acidic sites at low temperature had been scavenged through higher thermal treatment at 400 ^oC, 650 ^oC or 900 ^oC. The peaks at 252 ^oC and 440 ^oC also can't be observed on the TPD-NH_3 curves of the CNTs-A, CNTs-400, CNTs-650 and CNTs-900. Furthermore, the weak adsorption peak at 695 ^oC is observed for the CNTs-A, CNTs-400 and CNTs-650, and the intensity of this peak decreases gradually with increasing the thermal treatment temperature. But for CNTs-900, the weak adsorption peaks at 695 ^oC can't be observed at all. These findings indicate that the oxygen-containing groups on the CNTs can be gradually removed by increasing the thermal treatment temperature. In particular, the acidic sites of the CNTs can be removed by using the thermal treatment at 900 ^oC. Therefore, according to the NH_3-TPD analysis results of the CNTs compared in Fig. 2.2, the oxygen-containing groups on CNTs can be removed selectively via thermal treatment way at different temperature, which can also ensure the controllable encapsulation of cobalt nanoparticles inside CNTs channels with the assistance of wetness impregnation method.

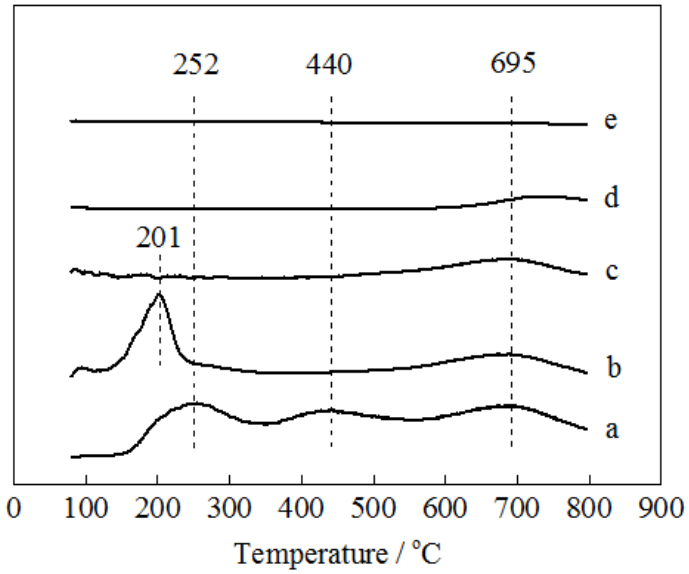

Fig. 2.2. a) The TPD profile of the pure CNTs-A without the adsorbed NH_3 as the reference of the profiles of other samples; NH_3-TPD patterns of the different CNTs supports: b) CNTs-A, c) CNTs-400, d) CNTs-650, e) CNTs-900.

Fig. 2.3 exhibits TEM images of the CNTs-A and the cobalt-loaded catalysts of Co/CNTs-A, Co/CNTs-400, Co/CNTs-650, Co/CNTs-900. As mentioned above, lots of oxygen-containing groups, such as -C=O, -COOH and -OH, formed on the surface of CNTs after nitric acid treatment, and these groups can adsorb cobalt ions on the surface of CNTs during impregnation process. In order to control the formation of cobalt clusters inside CNTs channels, a proper thermal treatment on the nitric acid treated CNTs should be investigated to remove the needless oxygen-containing groups on the outside surface of CNTs. The TEM images of CNTs-A in Fig. 2.3a indicates that the ends of CNTs had been opened after the nitric acid treatment. It is favorable for the cobalt-containing liquid to enter the inner channels of the CNTs supports with opened ends during the wetness impregnation process, sequentially leading to the formation of cobalt clusters inside CNTs channels during thermal treatment process. However, the oxygen-containing groups on the outside surface of the CNTs can also adsorb metallic

ions, thus forming metal-oxygen bonds [21]. For the Co/CNTs-A catalyst without thermal treatment on the nitric acid treated CNTs support, its TEM image in Fig. 2.3b reveals that the highly dispersed cobalt particles mainly deposited at the outside surface of the CNTs. In other words, the oxygen-containing groups on outer surface of the CNTs adsorb more cobalt particles than CNTs channels. Fig. 3c of Co/CNTs-400 shows that the cobalt particles are deposited at both inside and outside of CNTs channels. However, for the Co/CNTs-650 catalyst, most of the cobalt particles are encapsulated inside channels rather than outside surface of the CNTs, as shown in Fig. 2.3d. In the related NH_3-TPD result of this sample given in Fig. 2.2d, the support CNTs-650 still displays a weaker acid intensity. Consequently, the capillarity function of the integrity channels of CNTs-650 plus its weaker acid sites can help to encapsulate most cobalt nanoparticles inside CNTs channels. As a result, the ratio of Co particles inside the CNTs reaches as high as 80% for the Co/CNTs-650 catalyst, and the size of the cobalt nanoparticles is within 5-10 nm, as measured by TEM. The TEM image of Co/CNTs-900 catalyst is also presented in Fig. 2.3e. It seems that the walls of CNTs had been partially broken after thermal treatment at 900 ^{o}C, although almost all the cobalt clusters settle inside the CNTs channels. All the results discussed here experimentally prove that the controllable encapsulation of cobalt clusters in CNTs channels can be realized facilely by the pretreated CNTs with the concentrated nitric acid refluxing plus a followed thermal treatment at certain temperature.

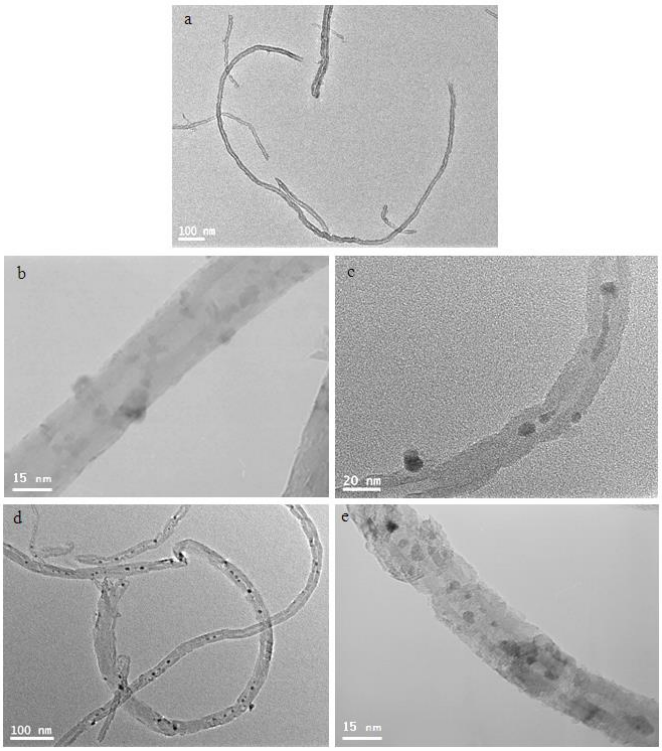

Fig. 2.3. TEM images of sample (a. CNTs-A; b. Co/CNTs-A; c. Co/CNTs-400; d. Co/CNTs-650; e. Co/CNTs-900)

The reduction behavior of different CNTs supports, CNTs-x (x=400, 650, 900), is studied by H_2-TPR and the results are compared in Fig. 2.4. All the fresh samples exhibit multiple reduction peaks due to the possible hydrogenation reaction of various oxygen-containing groups on the surface of CNTs［24］. For the H_2-TPR profile of the pure CNTs-A support, overlapped peaks appear as in Fig. 2.4a, which can be attributed to the hydrogenation of the oxygen-containing groups on the surface of CNTs. But the intensity of H_2-TPR peaks of other pure CNTs-x support decreases linearly since the increase of thermal treatment temperature. Therefore, the higher thermal treatment can effectively eliminate more oxygen-containing groups attached on the CNTs surface.

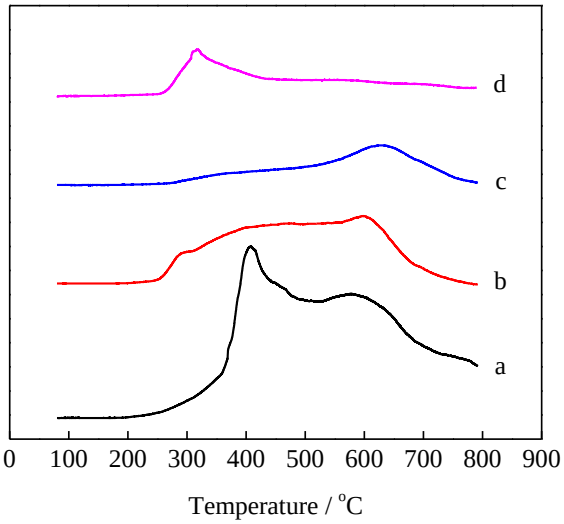

Fig. 2.4. H_2-TPR patterns of the different CNTs supports: a. CNTs-A, b. CNTs-400, c. CNTs-650 and d. CNTs-900.

2.3.2 FTS reactions

The catalytic performance of the CNTs supported cobalt catalysts was investigated in a fixed-bed reactor employing different reaction conditions. Table 2.2 shows that the catalytic performance of the 10wt% Co/CNTs-A and 10wt% Co/CNTs-x (x=400, 650, 900) catalysts in the FTS reaction. For Co/CNTs-A catalyst, the CO conversion and CH_4 selectivity are 92.8 % and 23.5 %, respectively. The catalytic activity of Co/CNTs-A is the highest one among the tested catalysts including Co/CNTs-x (x=400, 650, 900) series of catalysts. Here, the highest activity of Co/CNTs-A should be attributed to the single HNO_3 refluxing treatment that will result in more oxygen-containing groups formed on the surface of CNTs, consequently determining its high cobalt clusters dispersion compared with that of Co/CNTs-x catalysts. Although with slightly lower catalyst activity, the Co/CNTs-x catalysts still exhibit better ability on suppressing the formation of CH_4 and promoting the chain-growth of hydrocarbons. For Co/CNTs-650

catalyst, the selectivity of CH_4 is only 8.4%, the lowest value among the tested catalysts, while the selectivity of C_{5+} hydrocarbons reaches up to the highest value of 83.7%. The Co/CNTs-900 catalyst presents unsatisfied performance both on the catalyst activity (CO Conversion 69.8%) and products selectivity (C_{5+} selectivity 74.9%), possibly due to the fact that higher thermal treatment temperature of 900 ^{o}C partly destroys the structure integrity of CNTs, as proven by the TEM image in Fig. 2.3e.

Table 2.2 Catalytic performance of various catalysts for FTS

Catalyst	Conv. / %	Sel. / %		
	CO	CH_4	CO_2	C_{5+}
Co/CNTs-A	92.8	23.5	17.9	64.7
Co/CNTs-400	75.9	9.5	1.4	82.7
Co/CNTs-650	89.3	8.4	8.3	83.7
Co/CNTs-900	69.8	17.5	1.6	74.9

Reaction conditions: T=240 ^{o}C, P=1.0 MPa, H_2/CO=2/1, W/F=10 gh/mol.

Therefore, the most suitable thermal treatment temperature is 650 ^{o}C, which can help to encapsulate more cobalt clusters inside CNTs channels and at the same time reduce the possible damage on the walls of CNTs from thermal treatment. It is also very interesting that the amount of the C_{5+} hydrocarbons in the FTS products increases with increasing the amount of encapsulation of cobalt particles in CNTs channels. This phenomenon can be attributed to fact that the syngas easily enriches inside the channels of CNTs and contacts more cobalt clusters for more time, thus favoring the growth of longer chain hydrocarbons［15］.

Table 2.3 shows that the FTS reactions on the 10wt% Co/CNTs-650 catalyst at varied reaction temperature or with different ratio of H_2/CO. With increasing the reaction temperature from 220 ^{o}C to 260 ^{o}C, the CO conversion, the selectivities of CH_4

and CO_2 increase gradually, but the selectivity of the C_{5+} hydrocarbon decreases slightly. These results suggest that higher reaction temperature also favor the CO conversion of cobalt-loaded CNTs catalyst, but simultaneously suppress the formation of long-chain hydrocarbons, similar to former reports on general FTS catalysts［26］. It is well known that the carbon chain of FTS hydrocarbons will shift towards the shorter range if increasing FTS reaction temperature［27］. In addition, decreasing the ratio of H_2/CO from 2 to 1 in the syngas can clearly affect the CO conversion as well as FTS products distribution, as given also in Table 2.3. By using the syngas of H_2/CO = 1/1 for FTS reaction at 240 ^oC, the CO conversion decreases to 43.4 %, lower than 89.3 % of FTS reaction using the syngas of H_2/CO = 2/1 as the feed gas at the same reaction temperature. But the selectivity of CH_4 reduces to 5.4 % with the increase of C_{5+} hydrocarbons up to 86.3 %.

Table 2.3 Activity and selectivity of Co/CNTs-650 catalyst in FTS reaction

T / ^oC	H_2/CO	Conv. / %	Sel. / %		
		CO	CH_4	CO_2	C_{5+}
220	2/1	55.3	7.7	0.0	84.4
230	2/1	70.4	8.3	6.2	83.9
240	2/1	89.3	8.4	8.3	83.7
250	2/1	93.9	9.2	10.2	81.6
260	2/1	96.0	9.7	13.2	79.7
240	1/1	43.4	5.4	8.7	86.3

Reaction conditions: W/F=10 gh/mol, P=1.0 MPa, Catalyst: Co/CNTs-650.

2.4 Conclusions

In this report, we successfully realized the controllable encapsulation of cobalt clusters inside CNTs channels by using the combination of concentrated nitric acid refluxing, thermal treatment and wetness impregnation on CNTs supports. The thermal

treatment on the HNO_3 treated CNTs support at 650 ^oC effectively removed the oxygen-containing functional groups on the external surface of CNTs, simultaneously keeping the integrity of CNTs walls. The effect of the thermal treatment temperature of CNTs support to the catalytic activity of the final cobalt-loaded CNTs catalyst was investigated via the FTS reaction. For the Co/CNTs-650 catalyst prepared using the thermal treated CNTs at 650 ^oC, it exhibited better catalytic activity, lower CH_4 selectivity and higher C_{5+} hydrocarbon selectivity compared with other cobalt supported CNTs catalysts prepared by employing thermal treatment at other temperatures.

References

[1] K. Takeuchi, T. Matsuzaki, T.A. Hanaoka, H. Arakawa, Y. Sugi, K. Wei, ***J. Mol. Catal.*** 55 (1989) 361-370.

[2] G. Yang, N. Tsubaki, J. Shamoto, Y. Yoneyama, Y. Zhang, ***J. Am. Chem. Soc.*** 132 (2010) 8129-8136.

[3] J. Bao, J. He, Y. Zhang, Y. Yoneyama, N. Tsubaki, ***Angew. Chem. Int. Ed.*** 47 (2008) 353-356.

[4] E. Iglesia, S.C. Reyes, R.J. Madon, ***J. Catal.*** 129 (1991) 238-256.

[5] A.Y. Khodakov, ***Catal. Today*** 144 (2009) 251-257.

[6] B.C. Shi, B.H. Davis, ***Catal. Today*** 106 (2005) 129-131.

[7] S. Storsaeter, O. Borg, E.A. Blekkan, B. Totdal, A. Holmen, ***Catal. Today*** 100 (2005) 343-347.

[8] B.H. Davis, ***Ind. Eng. Chem. Res.*** 46 (2007) 8938-8945.

[9] A. Martínez, C. López, F. Márquez, I. Díaz, ***J. Catal.*** 220 (2003) 486-499.

[10] S. Storsater, B. Totdal, J. Walmsley, B. Tanem, A. Holmen, ***J. Catal.*** 236 (2005) 139-152.

[11] J.P. den Breejen, P.B. Radstake, G.L. Bezemer, J.H. Bitter, V. Froseth, A. Holmen, K.P. de Jong, ***J. Am. Chem. Soc.*** 131 (2009) 7197-7203.

[12] X.M. Sun, Y.D. Li, ***Angew. Chem. Int. Ed.*** 43 (2004) 597-601.

[13] Y. Zhu, Y.C. Ye, S.R. Zhang, M.E. Leong, F. Tao, ***Langmuir.*** 28 (2012) 8275-8280.

[14] K.S. Novoselov, A.K. Geim, S.V. Morozov, D. Jiang, M.I. Katsnelson, I.V. Grigorieva, S.V. Dubonos, A.A. Firsov, ***Nature*** 438 (2005) 197-200.

[15] R.M.M. Abbaslou, A. Tavassoli, J. Soltan, A.K. Dalai, ***Appl. Catal. A Gen.*** 367 (2009) 47-52.

[16] E. van Steen, F.F. Prinsloo, ***Catal. Today*** 71 (2002) 327-334.

[17] W. Chen, Z.L. Fan, X.L. Pan, X.H. Bao, ***J. Am. Chem. Soc.*** 130 (2008) 9414-9419.

[18] A. Tavasoli, M. Trepanier, A.K. Dalai, N. Abatzoglou, ***J. Chem. Eng. Data.*** 55 (2010) 2757-2763.

[19] M. Trepanier, A. Tavasoli, A.K. Dalai, N. Abatzoglou, ***Appl. Catal. A Gen.*** 353 (2009) 193-202.

[20] S. Kundu, Y.M. Wang, W. Xia, M. Muhler, ***J. Phys. Chem. C*** 112 (2008) 16869-16878.

[21] D.S. Zhang, H.X. Fu, L.Y. Shi, J.H. Fang, Q. Li, ***J. Solid State Chem.*** 180 (2007) 654-660.

[22] H. Zhang, W. Chu, C.J. Zou, Z.Y. Huang, Z.B. Ye, L. Zhu, ***Catal. Lett.*** 141 (2011) 438-444.

[23] S. Haydar, C. Moreno-Castilla, M.A. Ferro-Garcia, F. Carrasco-Marin, J. Rivera-Utrilla, A. Perrard, J.P. Joly, ***Carbon*** 38 (2000) 1297-1308.

[24] M.L. Toebes, E.M.P. van Heeswijk, J.H. Bitter, A.J. van Dillen, K.P. de Jong, ***Carbon*** 42 (2004) 307-315.

[25] W.P. Deng, X.S. Tan, W.H. Fang, Q.H. Zhang, Y. Wang, ***Catal. Lett.*** 133 (2009) 167-174.

[26] C. Pirola, C.L. Bianchi, A. Di Michele, S. Vitali, V. Ragaini, ***Catal. Commun.*** 10 (2009) 823-827.

[27] M.E. Dry, ***Catal. Today*** 71 (2002) 227-241.

Chapter 3 Tandem catalytic synthesis of light isoparaffin from syngas via Fischer-Tropsch synthesis by newly developed core-shell-like zeolite capsule catalysts

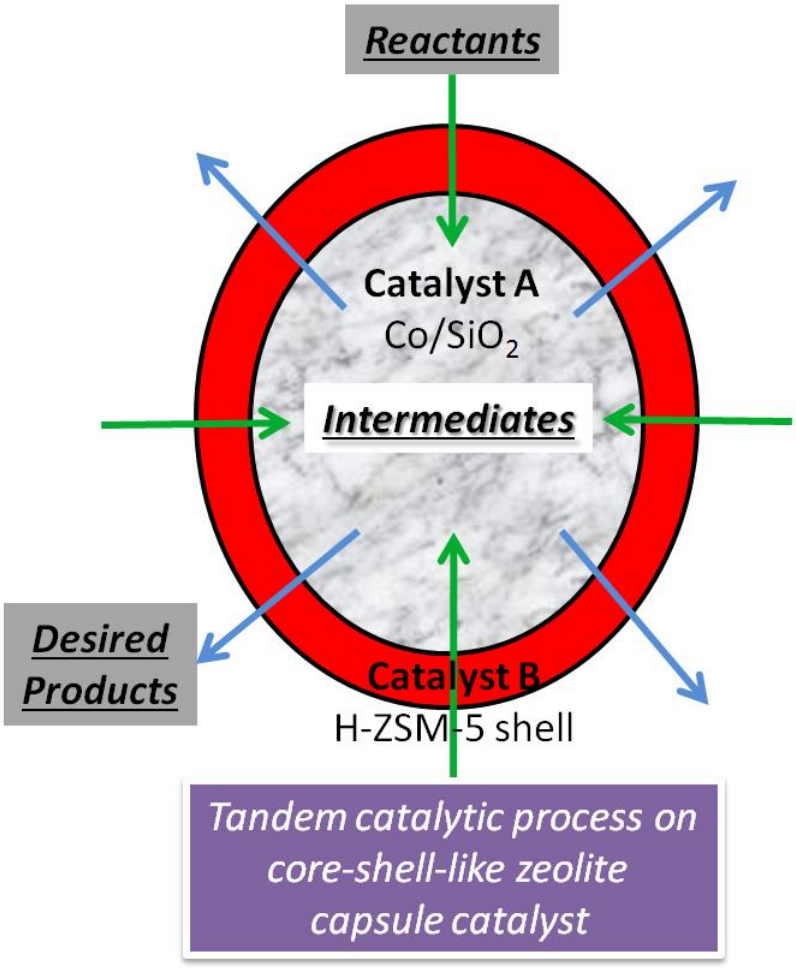

Abstract

One-step synthesis of light isoparaffin from syngas via Fischer-Tropsch synthesis (FTS) belongs to the tandem catalysis process, for which the most used catalyst is hybrid catalyst prepared by simply mixing FTS catalyst and zeolite catalyst. The zeolite capsule catalyst with a core-shell structure has proved its excellent performance for tandem catalysis process［1］, as well as the one-step synthesis of light isoparaffin from syngas mentioned before［2］. However, the usually used hydrothermal synthesis way for zeolite shell preparation limits the design and preparation of various zeolite shell enwrapping different core catalysts, the industrial scalability of zeolite capsule catalyst, and so on. In this report, with a traditional FTS catalyst of 10 wt% Co/SiO_2 as core catalysts, we present two methods for H-ZSM-5 zeolite capsule catalyst preparation. One is an improved hydrothermal synthesis process named stepwise-synthesis, another is an initially reported method that does not employ hydrothermal synthesis approach for H-ZSM-5 zeolite shell preparation. For the last one, we call it physically adhesive (PA) method in this report. The two types of H-ZSM-5 zeolite capsule catalysts prepared by these two methods are investigated via FTS reaction to evaluate their catalytic performance on the direct synthesis of light isoparaffin from syngas. Since the space-confined and synergistic function offered by the special core-shell structure, both of two types of H-ZSM-5 zeolite capsule catalysts could readily realize the one-step synthesis of light isoparaffin with higher selectivity, better than that of the conventional hybrid catalyst. The PA method presented in this report is very cost-saving, reliable and scalable, with which we can realize the industrialization of zeolite capsule catalyst more readily.

Keywords: Isoparaffin, Fischer-Tropsch Synthesis, Zeolite Capsule Catalyst, Zeolite, Tandem Catalysis

3.1 Introduction

Alternative energy sources have moved into the spotlight in recent years with soaring oil prices and dwindling resources [3]. Fischer-Tropsch synthesis (FTS) is a promising process converting syngas (CO +H_2) into a wide range of hydrocarbons that can be used as the substitute of petroleum-derived fuels [4,5], where the feedstock of syngas can be produced from varied resources like natural gas, biomass, coal, carbon dioxide, etc. [6,7]. The FTS products have the advantages of sulphur-free, aromatic-free and nitrogen-free properties [8-10], better than the conventional petroleum-derived products especially considering the serious environmental problems. But the general FTS products are almost normal aliphatic hydrocarbons following the Anderson-Schultz-Flory (ASF) distribution strictly [11]. Since the gasoline-like properties of middle isoparaffin, much effort has been made to explore effective ways on direct the synthesis of branched hydrocarbons via FTS reaction [4,12,13]. Among these studies, the further cracking and isomerization of normal heavy hydrocarbons of FTS on the acidic catalysts is one of most effective routes [8,14]. Therefore, so far, it is of great industrial interest to design hybrid catalysts for the direct synthesis of light isoparaffin from syngas through the tandem catalysis process: general FTS reaction plus cracking & isomerization reaction [15].

The combination of conventional FTS catalyst and zeolite with the structure style of physical mixture is a common way to produce the isoparaffins from syngas at one-step [16,17]. As illustrated by Scheme 3.1a, the FTS catalyst (Catalyst A) converts the syngas (Reactants) into linear hydrocarbons (Intermediates), part of the formed heavy hydrocarbons then migrate to the zeolite (Catalyst B) undergoing further hydrocracking and isomerization to form light isoparaffin (Desired products).

However, this type of catalyst structure style, physical mixture, provides only an unrestricted, open reaction environment where the coupled two reactions, FTS and cracking/isomerization, occur independently and randomly. This means that a part of the general FTS products can leave the catalyst directly without reacting further on the zeolite catalyst, resulting lower selectivity of light isoparaffin［2,18］.

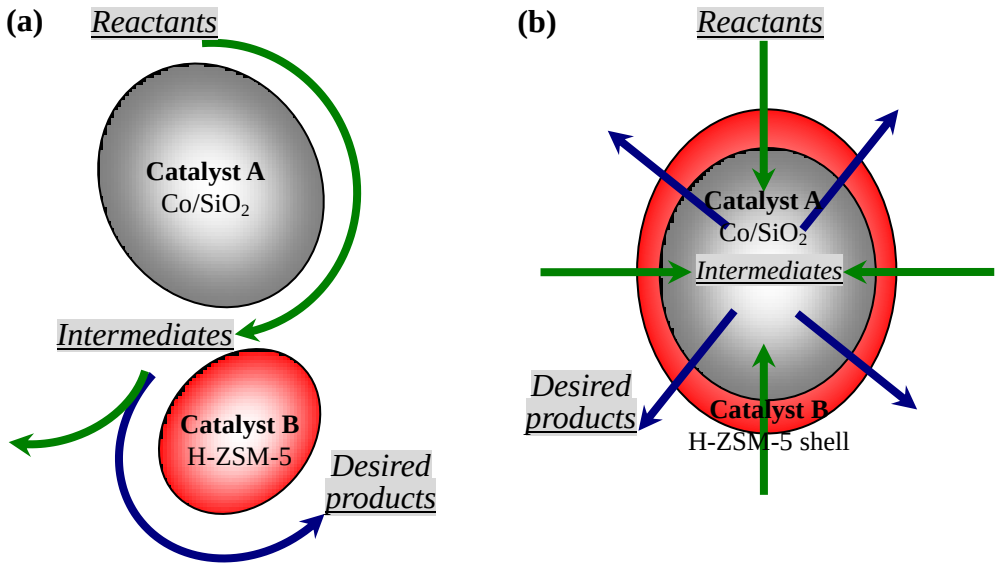

Scheme 3.1 The schematic representation of tandem catalysis process happened on the multifunctional catalyst with different assembly structure: (a) physically mixed catalyst, (b) core-shell-like capsule catalyst.

Designing the catalyst with a special core-shell structure like the assembly style presented by Scheme 3.1b is one of the most effective ways to enhance the selectivity of desired products during a tandem catalysis process［1,19］. Similarly, a catalyst with a core-shell structure (core: FTS catalyst-shell: zeolite membrane) can readily realize higher selectivity of light isoparaffins from syngas, as proved by former studies［2,20,21］. During FTS reaction on this capsule catalyst, the syngas (Reactants) firstly pass through the shell to reach the core catalyst (Catalyst A), forming the linear hydrocarbons (Intermediates). Before leaving the catalyst, all the hydrocarbons must

enter the zeolite shell, and the heavy hydrocarbons have more chances to be converted to isoparaffins (Desired products) on the acidic sites of zeolite shell, consequently resulting in higher selectivity of light isoparaffin in final FTS products.

Although with the striking catalytic performance, the zeolite capsule catalyst is designed only considering few zeolites until now, such as Silicalite-1 and H-ZSM-5, as shell candidates. The general preparation way of hydrothermal synthesis for constructing zeolite membrane synthesis is not so suitable to constructing some other important zeolite shell like H-Y or H-Beta on the FTS catalyst. The strong alkaline synthesis condition often needed for the synthesis of these zeolite membranes significantly limits the design and preparation of various zeolite capsule catalysts. Furthermore, the zeolite shell preparation through hydrothermal synthesis process faces more problems considering the vulnerable property of FTS core catalyst, as well as the difficulty of different zeolite membrane synthesis on varied supports. So far, the facile preparation of various acidic zeolite shells enwrapping different core catalyst is still a challenge.

In this report, two new methods are presented for zeolite capsule catalyst preparation. One is the improved hydrothermal synthesis process, named stepwise-synthesis, with a neutral Silcalite-1 zeolite shell as first intermediate layer for the next acidic H-ZSM-5 zeolite shell synthesis on the Co/SiO_2 FTS catalyst. Another method is a new way initially developed for core-shell-like zeolite capsule catalyst preparation without hydrothermal synthesis process. We call it physically adhesive (PA) method, that is, the independent zeolite powders are directly and uniformly pasted onto the Co/SiO_2 catalyst surface by using one type of silica sol (Ludox) as adhesive. The two types of prepared zeolite capsule catalysts are investigated through FTS reaction to

evaluate their catalytic performance on the direct synthesis of light isoparaffin from syngas. The PA method presented in this report is very cost-saving, reliable and scalable, with which we can realize the industrialization of zeolite capsule catalyst more readily.

3.2 Experimental

3.2.1 Co/SiO_2 catalysts preparation

In this report, the cobalt loaded SiO_2 catalysts with loading amount of 10 wt% was prepared by the conventional incipient wetness impregnation method［10］. The silica supports used in this report were the commercially available silica support (Fuji Silysia Chemical Ltd., Cariact Q-10, size range 0.85-1.70 mm, specific surface area 323 $m^2 \cdot g^{-1}$, pore volume 1.03 $cm^3 \cdot g^{-1}$, average diameter of pore 10 nm). The cobalt resource was $Co(NO_3)_2 \cdot 6H_2O$. The waterish catalyst precursors after impregnation were dried first at 393 K for 12 h and then calcined in air at 673 K for 2 h. The obtained 10 wt% Co/SiO_2 catalysts were used as the core catalyst for the followed zeolite capsule catalysts preparation.

3.2.2 Zeolite capsule catalysts preparation

In this report, two methods were employed for zeolite capsule catalyst preparation. One was a stepwise-synthesis method by using the hydrothermal synthesis process, in which the zeolite shell was prepared according to the description previously reported by us［18］. In brief, one Silicalite-1 zeolite layer was first synthesized on the naked Co/SiO_2 pellets, acting as an intermediate layer, and then another H-ZSM-5 zeolite shell grew on the intermediate layer forming the final H-ZSM-5 shell. The pure Co/SiO_2 and the Silicalite-1 zeolite synthesis solution with molar ratio of 2TEOS:0.48TPAOH: $120H_2O$:8EtOH:$0.024HNO_3$ were sealed together in an autoclave undergoing

hydrothermal synthesis. Crystallization temperature and synthesis time were 453 K and 24 h respectively. The Silicalite-1 zeolite layer coated core catalyst, as supports, was used for the following H-ZSM-5 zeolite shell synthesis. The H-ZSM-5 zeolite shell synthesis solution had the molar ratio of 2TEOS:0.68TPAOH:120H_2O:8EtOH: 0.24Al_2O_3, in which the aluminium resource comes from $Al(NO_3)_3 \cdot 9H_2O$. This hydrothermal synthesis was performed at 453 K for another 24 h. After the synthesis, zeolite capsule catalysts were separated from mother liquor and washed repeatedly by deionized water, followed by drying at 393 K for 12 h. And then, a calcination process was conducted at 773 K for 5 h removing the organic agent settled in zeolite pores. The silica-based core catalyst was stable after the total hydrothermal synthesis process and the followed calcination. he obtained zeolite capsule catalyst was named Co/SiO_2-Z-HT, where the "HT" in the catalyst name means the employed hydrothermal synthesis. The weight increment of this zeolite shell was close to 25 wt% towards to the naked Co/SiO_2 core catalyst.

Another method was a new way initially developed in this report for core-shell-like zeolite capsule catalyst preparation without the assistance of hydrothermal synthesis process. We call it physically adhesive (PA) method. The independent zeolite powders were directly and uniformly pasted on the Co/SiO_2 catalyst surface by using one type of silica sol (Ludox) as adhesive. In brief, the Co/SiO_2 core catalyst was first impregnated by silica sol. And then the wetted Co/SiO_2 pellets were moved into a round-bottom flask and mixed well with a certain amount of zeolite powders through vigorously rocking, finally resulting in the zeolite powder uniformly coated Co/SiO_2 catalyst. The separated samples from flask were dried at 393 K for 12 h and calcined at 773 K for another 3 h. Here, it should be noted that the mentioned process can be repeated for several times

very facilely, whereby we can easily realize varied zeolite coating amount. In this report, the zeolite candidate of H-ZSM-5 zeolite powder was prepared based on the same recipe and synthesis process to that of H-ZSM-5 zeolite shell preparation through hydrothermal synthesis process described above. The obtained zeolite capsule catalyst was named Co/SiO_2-Z-PA, where the "Z" means H-ZSM-5 zeolite shell and the "PA" stands for the physically adhesive method.

3.2.3 Physically mixed catalyst preparation

The H-ZSM-5 zeolite powder was also directly synthesized by using the same method to the H-ZSM-5 zeolite shell synthesis through hydrothermal synthesis process as presented in Section 2.2. The prepared H-ZSM-5 zeolite powder was physically mixed with the crushed 10 wt% Co/SiO_2. And then the mixture powder was granulated into the size of 0.85-1.70 mm. The weight content of zeolite in this physically mixed catalyst is same to that of zeolite capsule catalysts. In the following discussion, this catalyst is named Co/SiO_2-Z-M, where the "M" means the mechanical mixture of H-ZSM-5 and Co/SiO_2.

3.2.4 Hydrogenation catalyst Pd/SiO_2 preparation

The conventional hydrogenation catalyst 2.5 wt% Pd/SiO_2 was prepared by the incipient wetness impregnation method with $Pd(NH_3)_2(NO_3)_2$ as Pd resource. In this report, the Pd/SiO_2 catalyst will be used as hydrogenation catalyst for the dual-catalyst-layer FTS reaction process, in which it is loaded after the upper capsule catalyst layer to hydrogenate the formed olefins from FTS reaction, converting them into saturated hydrocarbons.

3.2.5 Catalyst characterization

An X-ray diffractometer (RINT 2200, Rigaku. Co.) equipped with CuKa radiation

was used to determine crystalline phases of the catalyst and particle size of cobalt oxide. Analysis operations were performed at 40 kV and 40 mA. The thickness of zeolite shell, as well as its composition and surface morphology, was determined by the scanning electron microscopy (JEOL, JSM-6360LV) combined with an energy-diffusive X-ray spectroscopy (JEOL, JED-2300). The samples before analysis were first pretreated by an auto fine coater (JEOL, JFC-1600) to coat a platinum layer on their surface.

3.2.6 FTS reaction

In this report, Fischer-Tropsch synthesis (FTS) reaction was carried out using a flow-type fixed-bed reactor (i.d. 8 mm) similar to the description presented by our previous reports [2]. Two types of catalyst loading model, single-catalyst-layer and dual-catalyst-layer as shown by Scheme 3.2, were adopted for investigating the catalytic performance of zeolite capsule catalysts in FTS reaction. Prior to reaction, the loaded catalysts were first reduced in situ at 673 K in a flow of pure H_2 for 10 h. The FTS reactions were implemented at 553 K under reaction pressure of 1.0 MPa with the syngas (H_2/CO = 2) as feedstock. All the effluent products from reactor were online heated and analyzed firstly by an online gas chromatography (Shimadzu, FID, GC-14B) equipped with a capillary column (J&W Scientific GS-Alumina, i.d. 0.53 mm × 30 m), identifying hydrocarbons composition. And then another online gas chromatography (Shimadzu, TCD, GC-8A) was used to determine the concentration of CO, CO_2, and CH_4 in the effluent from the FTS reactor. The CO conversion and the hydrocarbons selectivity were calculated with the followed equations.

$$\text{CO Conversion} = \frac{\left[\left(\frac{\text{Area}_{\text{CO}}}{\text{Area}_{\text{Ar}}}\right)_{\text{feedgas}} - \left(\frac{\text{Area}_{\text{CO}}}{\text{Area}_{\text{Ar}}}\right)_{\text{effluent}}\right]}{\left(\frac{\text{Area}_{\text{CO}}}{\text{Area}_{\text{Ar}}}\right)_{\text{feedgas}}} \times 100\%$$

$$C_n \text{ Selectivity} = \frac{C_n \text{ yield}}{\sum C_n \text{ yield}} \times 100\%; \quad (\text{The "n" means the carbon number of hydrocarbon.})$$

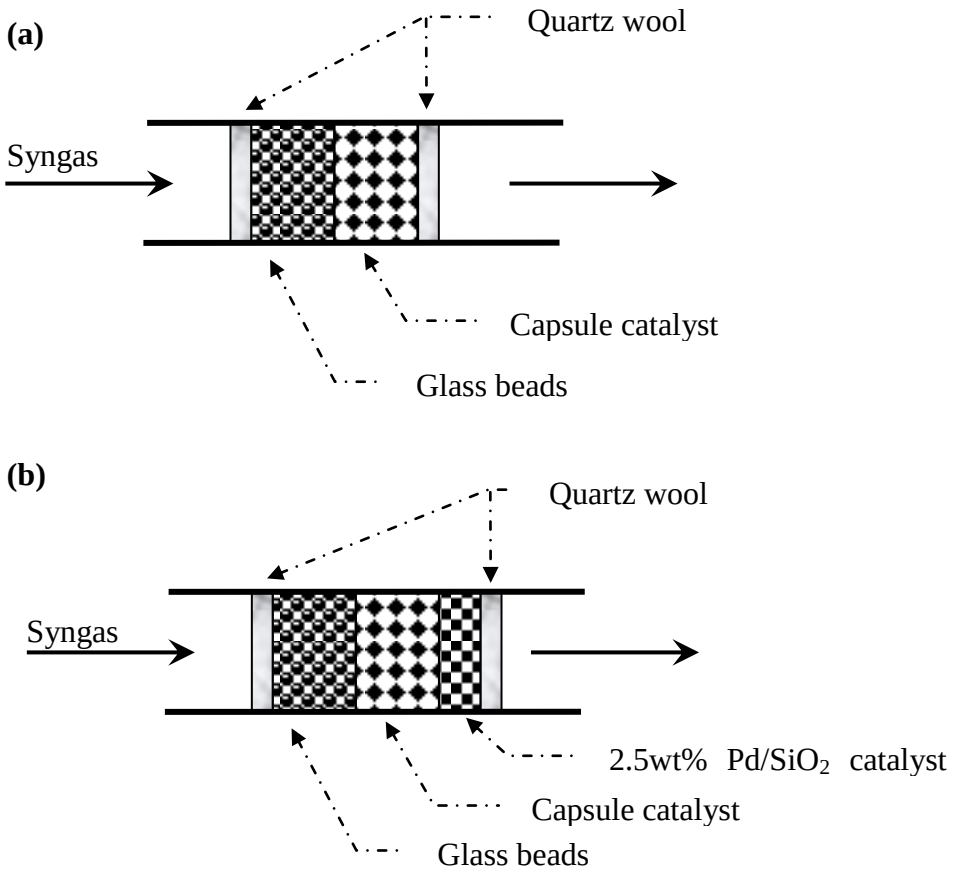

Scheme 3.2 The schematic representation of catalyst loading model in reactor for FTS reaction: (a) single-catalyst-layer, (b) dual-catalyst-layer.

3.3 Results and discussion

3.3.1 X-ray diffraction of catalysts

The two types of zeolite capsule catalysts, 10 wt% Co/SiO_2-Z-HT and 10 wt% Co/SiO_2-Z-PA, were characterized by X-ray diffraction (XRD) to identify whether the zeolite shell has successfully formed on the Co/SiO_2 core catalyst. As the reference of capsule catalysts, the core catalyst 10 wt% Co/SiO_2 and pure H-ZSM-5 zeolite catalyst were also measured by XRD. All XRD patterns of catalysts are showed in Fig. 3.1 and the peaks attributed to H-ZSM-5 zeolite are indexed on the XRD profiles. For XRD

pattern of Co/SiO_2 core catalyst, only some peaks belong to Co_3O_4 can be found and there are no any characteristic peaks of H-ZSM-5 zeolite. The zeolite capsule catalyst of Co/SiO_2-Z-HT is prepared by using the stepwise-synthesis method through hydrothermal synthesis process. The XRD pattern of Co/SiO_2-Z-HT zeolite capsule catalyst, as shown in Fig. 3.1, shows the characteristic peaks of H-ZSM-5 zeolite, indicating the appearance of zeolite crystal on the Co/SiO_2 core catalyst. Another zeolite capsule catalyst of Co/SiO_2-Z-PA prepared by physically adhesive (PA) method is also characterized by XRD to evaluate the formation of zeolite coating on the surface of Co/SiO_2 core catalyst. Comparing the XRD pattern of Co/SiO_2-Z-PA with that of pure H-ZSM-5 and Co/SiO_2, we can clearly identify that the H-ZSM-5 zeolite coating has been constructed successfully on the core catalyst with the assistance of the new developed PA method.

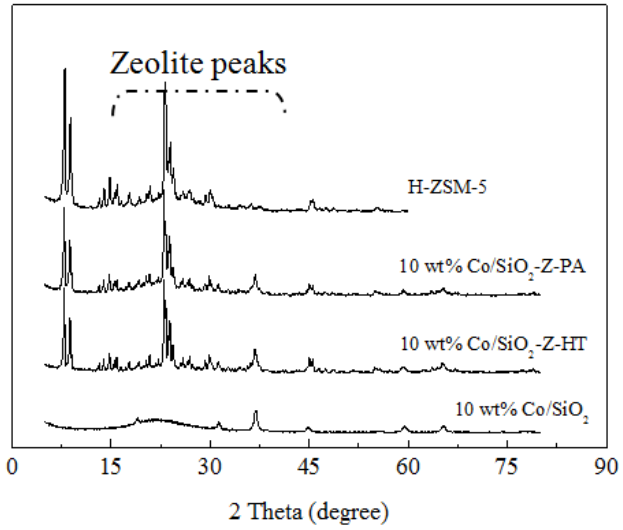

Fig. 3.1. XRD patterns of 10 wt% Co/SiO_2, 10 wt% Co/SiO_2-Z-HT, 10 wt% Co/SiO_2-Z-PA and pure H-ZSM-5 zeolite.

3.2.2 SEM and EDS analysis of catalysts

In order to get the morphology information of zeolite capsule catalysts, we

employed the scanning electron microscope (SEM) combined with an energy dispersive X-ray spectroscopy (EDS) to analyze the catalysts' surface, cross section, elemental compositions. The surface SEM image and EDS analysis of the naked Co/SiO_2 core catalyst are showed in Fig. 3.2. The weight content of cobalt calculated from its molar ratio of 11.4 % on this sample is very similar to its preparation recipe. Here, this ball-like Co/SiO_2 catalyst is used as the core catalyst for the followed zeolite capsule catalyst preparation through either of two different methods.

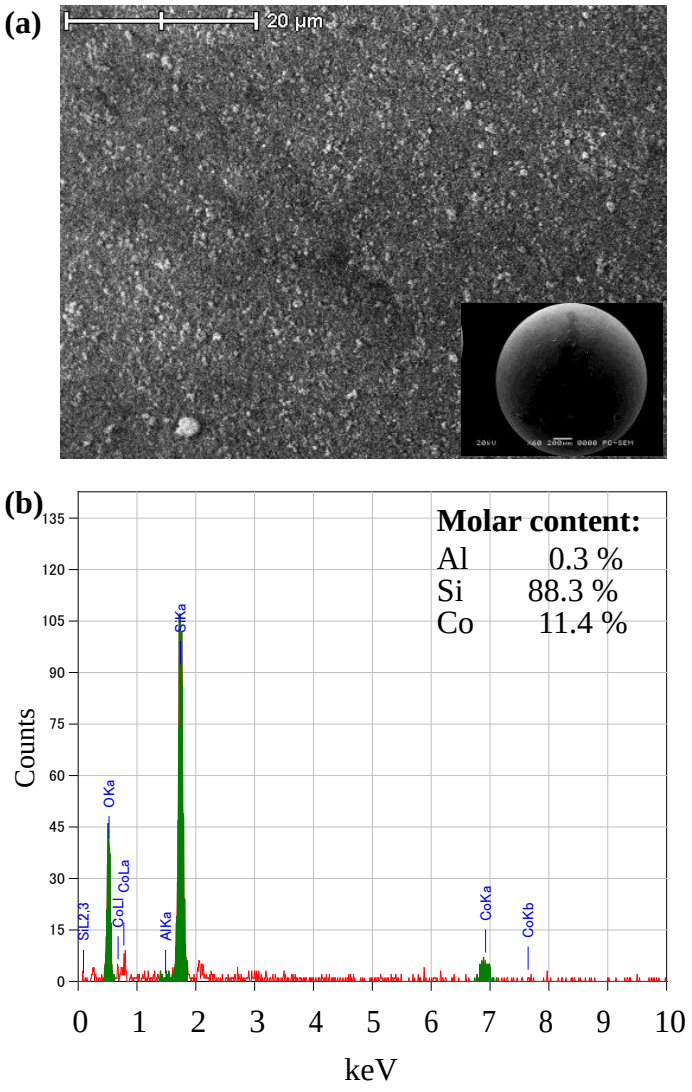

Fig. 3.2. (a) Surface SEM image (inset: complete morphology under lower magnification) and (b) EDS analysis of 10wt% Co/SiO_2.

By using the stepwise-synthesis method, we got the zeolite capsule catalyst Co/SiO_2-Z-HT. This type of zeolite capsule catalyst is characterized by SEM and EDS to judge the quality and integrity of the formed zeolite shell. The surface SEM image of Co/SiO_2-Z-HT is given in Fig. 3.3a, where we can find that the zeolite crystals, with the single crystal size of 1 μm, had formed and covered Co/SiO_2 core catalyst completely. And the formed zeolite shell is a homogeneous, uniform zeolite membrane without cracks or pinholes although undergoing harsh calcination before its characterization. The EDS analysis on this zeolite shell in Fig. 3.3b gives zero signals from cobalt, which can help us to further ensure the perfect encapsulation of core catalyst by zeolite shell. The well-prepared zeolite shell, here, is very crucial to the core-shell-like zeolite capsule catalyst. It can effectively construct a confined space for the FTS reaction happened on the Co/SiO_2 core catalyst, at the same time affording sufficient acidic sites converting the general FTS products of long-chain hydrocarbons directly into light isoparaffins. SEM and EDS analysis had also been employed to analyze the cross-section of zeolite capsule catalyst Co/SiO_2-Z-HT, evaluating its core-shell structure. The related cross-section SEM image, in Fig. 3.4a, suggests that one compact zeolite shell with thickness of 24 μm had formed on the surface of Co/SiO_2. In addition, the EDS line analysis on this cross section of Co/SiO_2-Z-HT, given in Fig. 3.4b, can also help us to identify the interface between core catalyst and zeolite shell. At the interface of two different phases, the Al signals increase sharply but the Si signals decrease conversely since the change of element content.

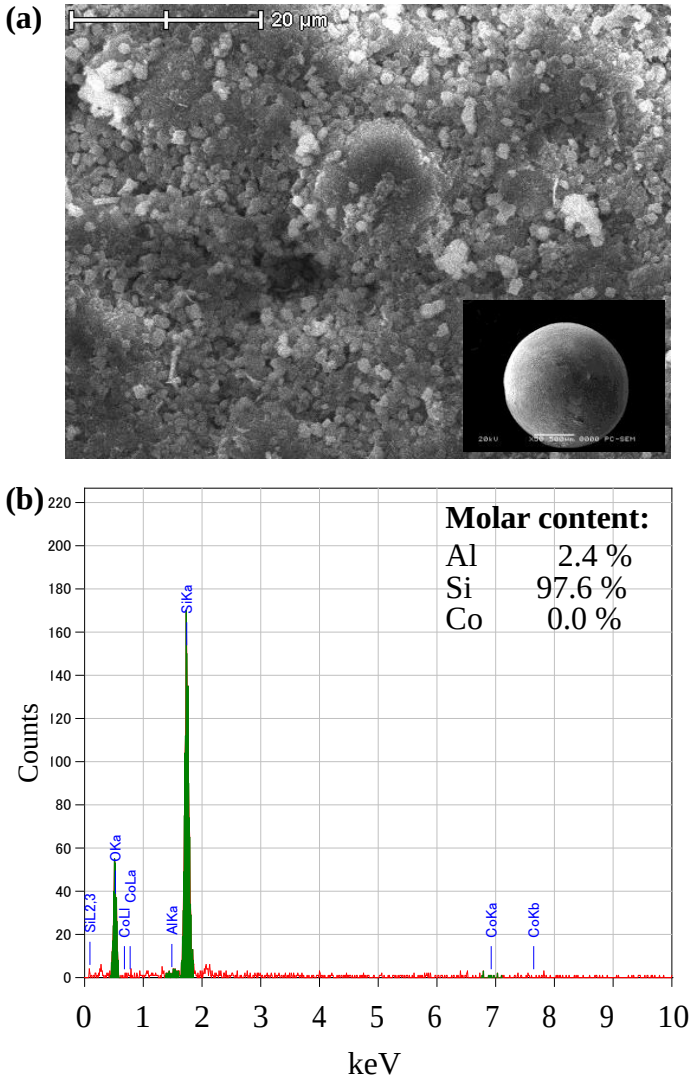

Fig. 3.3. (a) Surface SEM image (inset: complete morphology under lower magnification) and (b) EDS analysis of zeolite capsule catalyst 10% Co/SiO_2-Z-HT.

Another zeolite capsule catalyst Co/SiO_2-Z-PA is prepared by PA method, instead of the generally used hydrothermal synthesis process, to prepare zeolite shell on the naked Co/SiO_2 core catalyst. The surface SEM and EDS analysis results of Co/SiO_2-Z-PA are showed in Fig. 3.5, where we can find that one layer of zeolite has covered core catalyst very well. The slight differences between this type of zeolite shell and that of Co/SiO_2-Z-HT exhibited in Fig. 3.3 are the larger zeolite crystal and more porous structure here. The used zeolite powder for Co/SiO_2-Z-PA preparation is first

calcined to remove organic template. Here, the calcination process can lead to the aggregation of single zeolite crystal, therefore resulting in the zeolite cluster larger than single zeolite crystal. The porous structure of zeolite shell prepared by the PA method should be attributed to the shrinkage of adhesive during calciantion.

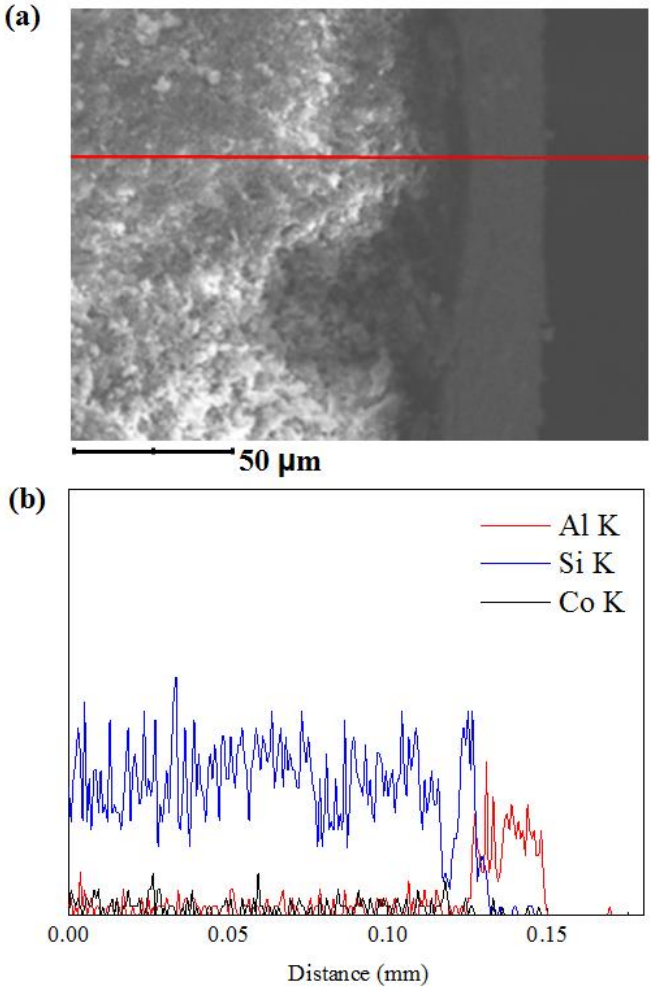

Fig. 3.4. Cross-section SEM image and EDS analysis of zeolite capsule catalyst 10% Co/SiO_2-Z-HT

In Fig. 3.5b, the surface EDS analysis of Co/SiO_2-Z-PA determines its surface elemental composition. The zero signal of cobalt indicates that the zeolite shell prepared by PA method is also integrity and defect-free, suggesting that this newly developed method for zeolite shell preparation without employing hydrothermal synthesis is

successful. The Si/Al on this Co/SiO_2-Z-PA is slightly higher than that of Co/SiO_2-Z-HT, which should be attributed to the use of adhesive, containing a certain mount of SiO_2. This PA method can effectively control the loading amount of zeolite on core catalyst, it is also very cost-saving since the effective utilization of zeolite crystals synthesized by hydrothermal synthesis process. Furthermore, the zeolite shell of capsule catalyst prepared by PA method has a very porous zeolite layer, with which the diffusion of reactants and products passing zeolite shell can be promoted more facilely.

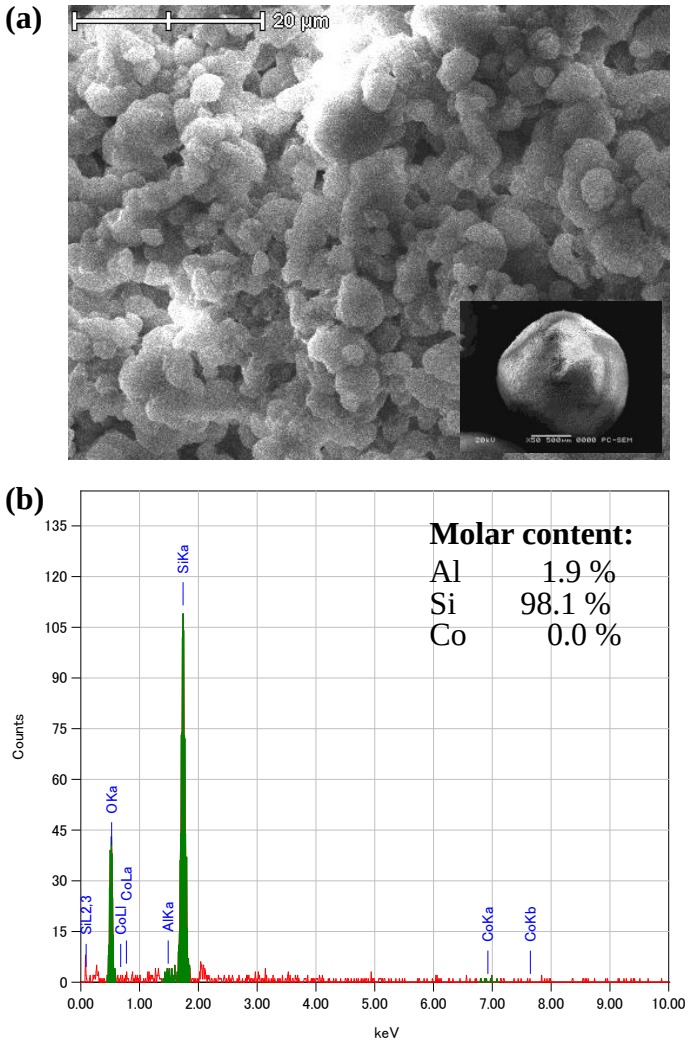

Fig. 3.5. (a) Surface SEM image (inset: complete morphology under lower magnification) and (b) EDS analysis of zeolite capsule catalyst 10% Co/SiO_2-Z-PA prepared by PA method.

3.3.3 Catalytic performances of zeolite capsule catalysts

The catalytic performances of two types of zeolite capsule catalysts, Co/SiO_2-Z-HT and Co/SiO_2-Z-PA, in FTS reaction are presented in Table 3.1. As the reference of zeolite capsule catalyst, the naked Co/SiO_2 core catalyst and the physically mixed catalyst Co/SiO_2-Z-M had been evaluated, and the reaction results are also compared in Table 3.1. Since the slight higher reaction temperature of 533K used in this study, all the tested catalyst exhibit good catalytic activity with CO conversion exceeding 90%. The zeolite capsule catalyst of Co/SiO_2-Z-HT gives the lowest CO conversion of 97.7 % among the tested catalysts. This zeolite capsule catalyst is prepared by using hydrothermal synthesis method to construct a zeolite shell enwrapping Co/SiO_2 core catalyst. The diffusion limitation of reactants/products passing zeolite shell should be considered. In addition, slightly lower catalytic activity of this zeolite capsule catalyst Co/SiO_2-Z-HT could be attributed to the formation of some zeolite crystals on the core catalyst covering part of the metallic Co particles. And the close contact of single zeolite crystal or shell with Co/SiO_2 in this sample will also lead to partial interaction of the metallic clusters with strong Brönsted acidity of zeolite, possibly leading to the suppression of the cracking activity of zeolite shell during the followed FTS reaction. For another zeolite capsule catalyst Co/SiO_2-Z-PA, it is prepared by using the newly developed PA method without employing hydrothermal synthesis to construct zeolite shell. The CO conversion of Co/SiO_2-Z-PA is almost same to that of Co/SiO_2 core catalyst, indicating that the PA method can effectively avoid the damage from hydrothermal synthesis and at the same time promote the diffusion of reactants and products passing zeolite shell.

Table 3.1 The catalytic performance of different catalysts in FTS reaction. [a]

Catalysts	Zeolite Increment (%) [e]	CO Conv. (%)	Sel. (%)		Selectivity (%) [f]			
			CH_4	CO_2	C_n	$C_=$	C_{iso}	C_{11+}
Co/SiO_2	0	99.2	25.7	17.1	88.0	1.5	10.5	15.3
Co/SiO_2-Z-HT [b]	25	97.7	17.5	19.8	49.7	1.0	49.3	0.4
Co/SiO_2-Z-PA [c]	25	99.1	20.1	18.2	47.6	8.6	43.8	1.2
Co/SiO_2-Z-M	25	98.5	23.7	16.0	53.4	10.4	36.2	8.2
Co/SiO_2-Z-PA	60	99.3	10.3	18.0	35.0	13.5	51.5	0.3
Co/SiO_2-Z-PA + Pd/SiO_2 [d]	60	99.5	11.2	23.2	37.1	1.4	61.5	1.2

[a] Reaction conditions: T = 553 K, P = 1.0 MPa, H_2/CO = 2, $W_{Co/SiO2}/F_{Syngas}$ =10 g·h·mol^{-1}.

[b] The "HT" means the hydrothermal synthesis method and the "Z" stands for the H-ZSM-5 zeolite shell.

[c] "PA" means the zeolite shell prepared by physically adhesive method.

[d] FTS reaction with the dual-catalyst-layer model: zeolite capsule catalyst + hydrogenation catalyst.

[e] Zeolite increment means the increased zeolite weight through HT or PA method towards to Co/SiO_2 core catalyst.

[f] C_n: normal paraffin; $C_=$: olefin; C_{iso}: isoparaffin; C_{11+}: hydrocarbons with carbon number more than 11.

The FTS products selectivity on different catalysts is also listed in Table 3.1. For the naked Co/SiO_2 catalyst, the main products are normal paraffin with the selectivity of 88.0 %, and there is only a few of olefin and isoparaffin in the final products. In addition, the selectivity of the heavy hydrocarbons (C_{11+}) reaches 15.3 %. All these results, for this conventional FTS catalyst Co/SiO_2, are consistent with the former reports［22］. For the physically mixed catalyst Co/SiO_2-Z-M made by mixing FTS catalyst Co/SiO_2 and H-ZSM-5 zeolite, it has a different products distribution compared with that of pure Co/SiO_2. The selectivity of normal paraffin on this hybrid catalyst is 53.4 %, very lower than that of the pure Co/SiO_2, as given in Table 3.1. But the selectivity of olefin and isoparaffin has reached up to 10.4 % and 36.2 % respectively.

The better ability of Co/SiO_2-Z-M on producing isoparaffin can be ascribed to its hybrid composition. In FTS reaction on this hybrid catalyst, the syngas first react on the Co/SiO_2 to produce the general FTS products (containing lots of long-chain hydrocarbons), and then part of the formed FTS products will escape from the catalyst layer without contact with zeolite catalyst, but other part of the FTS products can remain on this hybrid catalyst until being cracked or isomerized by H-ZSM-5 zeolite catalyst. Furthermore, it should also be noted that the re-adsorption of initial 1-olefins in FTS reaction on the zeolite surface can prevent the chain growth processes, partly contributing to the generation of light hydrocarbons [23-25]. However, the catalyst structure of this hybrid catalyst, randomly mixing, decides that it can not convert the heavy hydrocarbons as more as possible, as proved by the existence of C_{11+} with selectivity of 8.2 %.

Two types of zeolite capsule catalysts, Co/SiO_2-Z-HT and Co/SiO_2-Z-PA, exhibit different products distribution compared with that of Co/SiO_2-Z-M. Although with the same zeolite content to Co/SiO_2–Z–M, the selectivity of light isoparaffin obtained by zeolite capsule catalysts increase sharply and at the same time the formation of heavy hydrocarbons is suppressed obviously. As shown in Table 3.1, the zeolite capsule catalysts Co/SiO_2-Z-HT and Co/SiO_2-Z-PA give higher isoparaffin selectivity of 49.3 % and 43.8 % respectively, and their C_{11+} selectivities are only 0.4 % and 1.2 %. Here, the different products distribution of zeolite capsule catalyst compared with that of physically mixed catalyst Co/SiO_2-Z-M can be ascribed to their difference on catalyst structure. Different with the physically mixed catalyst Co/SiO_2-Z-M, the zeolite capsule catalyst has a special core-shell-like structure, which can form a confined reaction space and thus result in synergistic effect during the FTS reaction process. The core catalyst

Co/SiO_2 is used as the initial catalyst for general FTS reaction and the zeolite shell enwrapped core catalyst acts as the secondary catalyst to capture the formed long-chain hydrocarbons and crack/isomerizes heavy hydrocarbons into light isoparaffin, finally improving the content of isoparaffin in the FTS products. The FTS reaction together with cracking & isomerization reaction proceeds orderly, smoothly and cooperatively, resulting in the striking ability of these zeolite capsule catalysts on the direct synthesis light isoparaffin from syngas.

The PA method can manipulate the capacity of zeolite shell very easily. In this study, we also prepared the zeolite capsule Co/SiO_2-Z-PA with zeolite increment of 60 %, the FTS reaction results are also listed in Table 3.1. On account of the increase of zeolite shell capacity, the formed heavy hydrocarbons can be converted more completely, consequently leading to the sharp increase of isoparaffin selectivity reaching up to 51.5 %. But the olefin selectivity increases simultaneously since the cracking of hydrocarbons on the zeolite capsule. As we know, olefin is not welcome for FTS products if it is directly used as the substitute of gasoline. In order to reduce the olefin content, a dual-catalyst-layer FTS reaction using the zeolite capsule catalyst plus the hydrogenation catalyst Pd/SiO_2 is studied. The zeolite capsule catalyst Co/SiO_2-Z-PA is fixed at the first stage and the Pd/SiO_2 catalyst is located at the second stage, as shown in Scheme 3.2b. During the reaction, the syngas passes through the first catalyst layer to react similarly to the reaction happening on the single zeolite capsule catalyst, while the effluent products from the first stage enter the second stage for the hydrogenation of olefin. As listed in Table 3.1, the olefin selectivity on the combination of Co/SiO_2-Z-PA + Pd/SiO_2 strikingly decreased from 13.5 % to 1.4 %, and the selectivity of isparaffin increases markedly from 51.5 % to 61.5 %.

It should be also noted that zeolite capsule catalysts show lower CH_4 selectivity than that of naked Co/SiO_2 core catalyst. This uncommon result, contrary to the general rules of FTS reaction, could be ascribed to two possible reasons. One is the so called "bed dilution" phenomena. With the newly developed PA method, the zeolite loading amount on the core catalyst reaches up to 60 wt% even more, surpassing the zeolite loading ability offered by traditional hydrothermal synthesis method. The zeolite shell encapsulated core catalyst has bigger volume than that of bare Co/SiO_2, thus resulting in its slightly longer catalyst bed in reactor. Another reason that also influences capsule catalyst performance is the thermodynamic property of reaction. The FTS reaction happened on the core catalyst has a reversed thermodynamic property to that of cracking&isomerization reaction occurred on the zeolite shell. The exothermal FTS reaction and the endothermic cracking&isomerization are integrated as a tandem reaction mode. Cracking&isomerization reaction absorbs, in situ, the heat radiated from FTS reaction. These two thermodynamically opposite reactions sit closely, promote mutually and react simultaneously, leading to the changed temperature, syngas composition, as well as intrinsic pressure in the core region of capsule catalyst.

3.4 Conclusions

In this report, we successfully designed and prepared two types of core-shell-like zeolite capsule catalysts, Co/SiO_2-Z-HT and Co/SiO_2-Z-PA, by using two different methods respectively: (a) stepwise-synthesis method with the assistance of hydrothermal synthesis and (b) physically adhesive (PA) method without hydrothermal synthesis. The prepared zeolite capsule catalysts Co/SiO_2-Z-HT and Co/SiO_2-Z-PA were tested to investigate their catalytic ability on the direct synthesis of light isoparaffin

from syngas through FTS reaction. The catalyst evaluation results suggested that both of two types of zeolite capsule catalysts could effectively improve the selectivity of light isoparaffin, simultaneously depressing the formation of heavy hydrocarbons, very better than the traditional hybrid catalyst prepared by physically mixed method. The striking performance of these zeolite capsule catalysts stemmed from the confinement function and synergistic effect afforded by their specific core-shell structure. The PA method initially presented in this report was very cost-saving, reliable and scalable, overcoming much practical problems faced by the preparation of zeolite capsule catalysts through hydrothermal synthesis way. With this PA method, we can realize the industrialization of zeolite capsule catalyst more readily. Moreover, the concept of zeolite capsule catalysts and PA method presented in this report can also bring new opportunities to developing various zeolite capsule catalysts for different tandem catalysis systems.

References

[1] G. Yang, N. Tsubaki, J. Shamoto, Y. Yoneyama, Y. Zhang, ***J. Am. Chem. Soc.*** 132 (2010) 8129-8136.

[2] J. Bao, J. He, Y. Zhang, Y. Yoneyama, N. Tsubaki, ***Angew. Chem. Int. Ed.*** 47 (2008) 353-356.

[3] A.E. Farrell, ***Science*** 312 (2006) 1748-1748.

[4] Q. Zhang, J. Kang, Y. Wang, ***ChemCatChem*** 2 (2010) 1030-1058.

[5] X.H. Liu, A. Hamasaki, T. Honma, M. Tokunaga, ***Catal. Today*** 175 (2011) 494-503.

[6] A.Y. Khodakov, W. Chu, P. Fongarland, ***Chem. Rev.*** 107 (2007) 1692-1744.

[7] Y.C. Liu, J.G. Chen, K.G. Fang, Y.L. Wang, Y.H. Sun, ***Catal. Commun.*** 8 (2007) 945-949.

[8] J. Kang, K. Cheng, L. Zhang, Q. Zhang, J. Ding, W. Hua, Y. Lou, Q. Zhai, Y. Wang, ***Angew. Chem. Int. Ed.*** 50 (2011) 5200-5203.

[9] B.H. Davis, ***Ind. Eng. Chem. Res.*** 46 (2007) 8938-8945.

[10] N. Tsubaki, K. Yoshii, K. Fujimoto, ***J. Catal.*** 207 (2002) 371-375.

[11] X. Liu, M. Tokunaga, ***ChemCatChem*** 2 (2010) 1569-1572.

[12] Y. Wang, B. Hou, J. Chen, L. Jia, D. Li, Y. Sun, ***Catal. Commun.*** 10 (2009) 747-752.

[13] G.B. Yu, B. Sun, Y. Pei, S.H. Xie, S.R. Yan, M.H. Qiao, K.N. Fan, X.X. Zhang, B.N. Zong, ***J. Am. Chem. Soc.*** 132 (2010) 935-+.

[14] K. Cheng, J. Kang, S. Huang, Z. You, Q. Zhang, J. Ding, W. Hua, Y. Lou, W. Deng, Y. Wang, ***ACS Catal.*** 2 (2012) 441-449.

[15] X. Li, K. Asami, M. Luo, K. Michiki, N. Tsubaki, K. Fujimoto, ***Catal. Today*** 84 (2003) 59-65.

[16] Z.W. Liu, X.H. Li, K. Asami, K. Fujimoto, ***Appl. Catal. A Gen.*** 300 (2006) 162-169.

[17] Y. Yoneyama, J. He, Y. Morii, S. Azuma, N. Tsubaki, ***Catal. Today*** 104 (2005) 37-40.

[18] G. Yang, D. Wang, Y. Yoneyama, Y. Tan, N. Tsubaki, ***Chem. Commun.*** 48 (2012) 1263-1265.

[19] X.Y. Lai, J.E. Halpert, D. Wang, ***Energy Environ. Sci.*** 5 (2012) 5604-5618.

[20] J. He, Z. Liu, Y. Yoneyama, N. Nishiyama, N. Tsubaki, ***Chem. Eur. J.*** 12 (2006) 8296-8304.

[21] G. Yang, J. He, Y. Zhang, Y. Yoneyama, Y. Tan, Y. Han, T. Vitidsant, N. Tsubaki, ***Energy Fuel*** 22 (2008) 1463-1468.

[22] N. Tsubaki, S.L. Sun, K. Fujimoto, ***J. Catal.*** 199 (2001) 236-246.

[23] X.H. Liu, M. Tokunaga, ***ChemCatChem*** 2 (2010) 1569-1572.

[24] C. Ngamcharussrivichai, X.H. Liu, X.H. Li, T. Vitidsant, K. Fujimoto, ***Fuel*** 86 (2007) 50-59.

[25] X. Liu, X. Li, K. Fujimoto, ***Catal. Commun.*** 8 (2007) 1329-1335.

Chapter 4 Tunable isoparaffin and olefin synthesis in Fischer-Tropsch synthesis achieved by composite catalyst

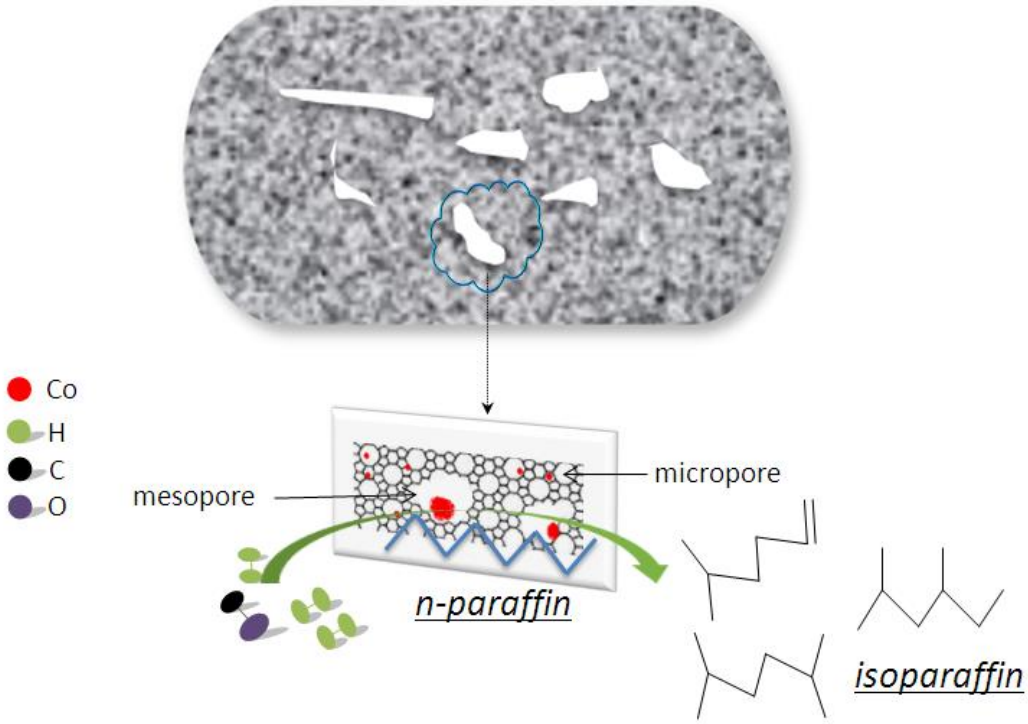

Abstract

Hierarchical HZSM-5 zeolite with combined micropores and mesopores was synthesized by one-step approach with TPAOH and F127 as dual templates. The physical and acidic properties of the hierarchical HZSM-5 zeolite were characterized by XRD, N_2 adsorption, SEM, TEM, NH_3-TPD techniques. The hierarchical HZSM-5 exhibited significantly higher mesopore surface area and larger mesopore volume than conventional HZSM-5. The prepared hierarchical HZSM-5 and conventional HZSM-5 supported cobalt catalysts were evaluated via Fischer-Tropsch synthesis (FTS) reaction to tune product selectivity. Compared with the conventional catalyst, the CO conversion of FTS reaction on the present catalyst increased significantly. Meanwhile, the C_{5+} selectivity and the isoparaffin selectivity also increased. The C_{5-11} hydrocarbons with a lot of isoparaffin and olefin had become the main FTS products due to optimized hydrocracking and isomerization afforded by the hierarchical pore structure, different from the conventional FTS hydrocarbons which were mainly composed of normal paraffin.

Keywords: Hierarchical, HZSM-5, Mesopore, Fischer-Tropsch Synthesis, Isoparaffin.

4.1 Introduction

Zeolites, with high internal surface area, high thermal stability, unique micropore size, intrinsic acidity, have been widely used as the shape-selective catalysts, used in oil refining and fine chemistry [1]. Unfortunately, the relatively small micropores strongly inhibit mass transfer of reactants and products in catalytic reactions [2,3]. In order to overcome this problem, the hierarchical zeolites as catalysts or catalyst supports have been studied widely. In recent years, different techniques have been employed to synthesize hierarchical zeolites with combined micropores and mesopores, generally including steaming, acid leaching (dealumination) or base leaching (desilication), templating, chemical treatment and direct synthesis process [4]. For example, desilication has been studied deeply as a common method to generate mesoporous HZSM-5 zeolite [5]. Moreover, mesoporous zeolites are usually synthesized through nanocasting method on various templates, *e.g.* $CaCO_3$ [6], carbon black [7], carbon nanotubes [8], carbon nanofiber [9], ordered mesoporous carbon [10], carbon aerogels and polymer aerogels [11]. However, the troublesome preparation or high cost of the carbon template is still inevitable. Therefore, direct synthesis of mesoporous zeolites is one of the promising strategies to reduce the use of raw materials, energy and costs.

Fischer-Tropsch synthesis (FTS) reaction is a process to produce ultra clean liquid fuel via the transformation syngas ($CO+H_2$), which can be generated from many resources such as coal, biomass, nature gas and garbage [12]. The FTS products are mostly linear paraffin, whose distribution (from methane to long-chain hydrocarbons) obeys the Anderson-Schultz-Flory (ASF) law [13]. Middle hydrocarbons, with a range of C_{5-11}, particularly rich in isoparaffin and olefin, as gasoline-range liquid fuels with high octane value, are important fuel from petrochemical industry. It is well known that acidic zeolites or other acidic supports present good performance for hydrocracking and isomerization to produce more isoparaffin as the ideal synthetic gasoline [14,15]. To obtain high selectivity of C_{5-11} hydrocarbons with high isoparaffin selectivity, several technologies such as

conventional HZSM-5 supported metal［16］, physical mixture［17］, two-step hydrocracking reaction［18］and a novel capsule catalyst［19］for middle isoparaffin synthesis via FTS have been investigated.

Here, we report a facile one-step synthesis of hierarchical HZSM-5 zeolite with TPAOH and F127 as dual templates, being applied in FTS reaction for direct middle isoparaffin synthesis. The overall synthetic route is illustrated in Fig. 4.1. In the first step, a homogeneous solution, including silicon source, aluminium source, water, micro- and meso-templates, was prepared and then the solution converted gradually into dry gel as in Fig. 4.1(b), followed by crystallization in a water-steaming environment as in Fig. 4.1(c). Finally, the micro- and meso-templates were removed through calcination in air.

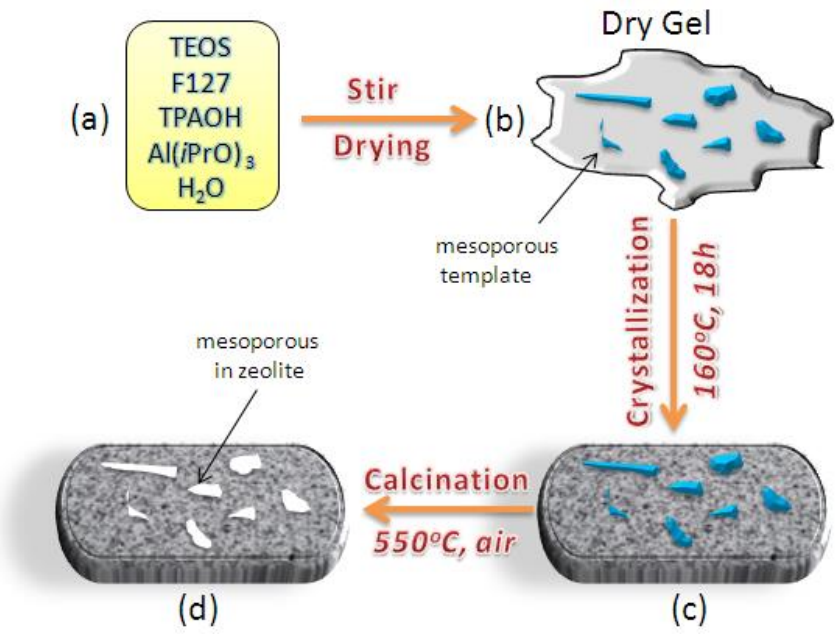

Fig. 4.1. Schematic depiction of the hierarchical zeolite preparation procedure.

4.2 Experimental Section

4.2.1 Catalyst preparation

The hierarchical HZSM-5 was prepared by a mixed aqueous solution of aluminium isoporpoxide, pluronic F127 (Sigma, MW=12600), tetraethylorthosilicate (TEOS) and distilled water under continuous stirring to get a clear solution. Then, the tetrapropylammonium hydroxide (TPAOH) was added drop wise to the solution, and

continued stirring at 40 ^{o}C to form a gel. The molar ratio of the resultant gel was 0.5 Al_2O_3: 50 SiO_2: 0.6 F127: 6 TPAOH: 2400 H_2O. The gel was aged at 60 ^{o}C, and dried at 90 ^{o}C overnight. Finally, the solid gel was transferred to Teflon-lined reactor and crystallized by steam-assisted crystallization (SAC) method at 160 ^{o}C for 18 h. The product was washed, dried and calcined at 550 °C for 5 h. The hierarchical HZSM-5 zeolite was denoted as meso-HZSM-5. A conventional HZSM-5 zeolite (conv-HZSM-5), as a reference catalyst, was also prepared by the same method but without F127 addition.

The FTS catalysts with the Co loading amount of 10 wt% were prepared by an incipient wetness impregnation method on conv-HZSM-5 and meso-HZSM-5 support with the aqueous solution of cobalt nitrate. Then the wet catalysts were dried at 120 ^{o}C overnight and calcined in air at 400 ^{o}C for 2 h. These catalysts were noted as Co/conv-HZSM-5 and Co/meso-HZSM-5, respectively.

4.2.2 Catalyst characterization

The crystalline structure of samples was measured by X-ray diffraction (XRD) with a Rigaku RINT 2400 diffractometer employing Cu K_α radiation. The nitrogen adsorption and desorption experiments of the samples were performed on an automatic gas adsorption system (Autosorb-1, Quantachrome). The surface morphology of sample was characterized with a scanning electron microscopy (SEM, JEOL, JSM-6360LV). Transmission electron microscopy (TEM) characterization on the catalyst was obtained by a JEOL JEM-200CX at 120 kV. NH_3 temperature programmed desorption (NH_3-TPD) experiments were conducted in a flow apparatus on a BELCAT-B-TT (BEL, Japan) instrument.

4.2.3 FTS tests

FTS reaction was carried out in a flowing fixed-bed reactor. In brief, 0.5 g catalyst was loaded at the center of the stainless steel reactor and reduced in situ at 400 ^{o}C in pure H_2 for 10 h, and followed by cooling to 240 ^{o}C. FTS reactions were carried out using the syngas with the ratio of H_2/CO=2 and $W_{Catalyst}$/F=10 gh/mol at 240 ^{o}C under reaction pressure of 1.0 MPa. The effluent gas released from the reactor was analyzed by two online gas chromatographs (Shimadzu GC-8A, TCD and

Shimadzu GC-14B, FID). An ice trap was fixed between reactor and back pressure regulator to capture the heavy hydrocarbons, which were analyzed by an offline gas chromatograph (Shimadzu GC-2014, FID). The configuration of the reactor was showed in Scheme 4.1.

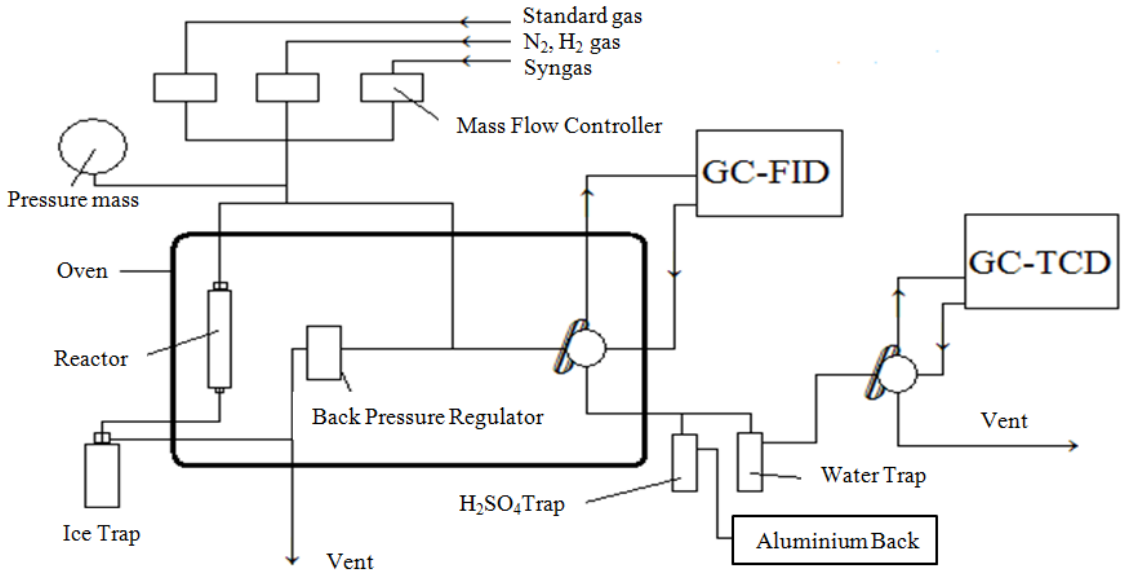

Scheme 4.1. Schematic diagram of FTS reaction

4.3 Results and Discussion

Fig. 4.2 shows the XRD patterns of Co/conv-HZSM-5 and Co/meso-HZSM-5 catalyst after caicination in air for 2 h at 400 ^{o}C. A series of diffraction peaks are clearly identified at range of 7-9^{o} and 23-25^{o}, suggesting that the conv- and meso-HZSM-5 with MFI structure were synthesized successfully. The peaks of the meso-HZSM-5 are slightly weaker than those of the conv-HZSM-5, which is in good agreement with the previous report [2]. The Co_3O_4 reflections are also identified. However, the Co_3O_4 size of Co/conv-HZSM-5 is 16.1 nm, larger than Co/meso-HZSM-5 with 12.7 nm (Table 4.1) because cobalt particles aggregated on the surface of conv-HZSM-5 support.

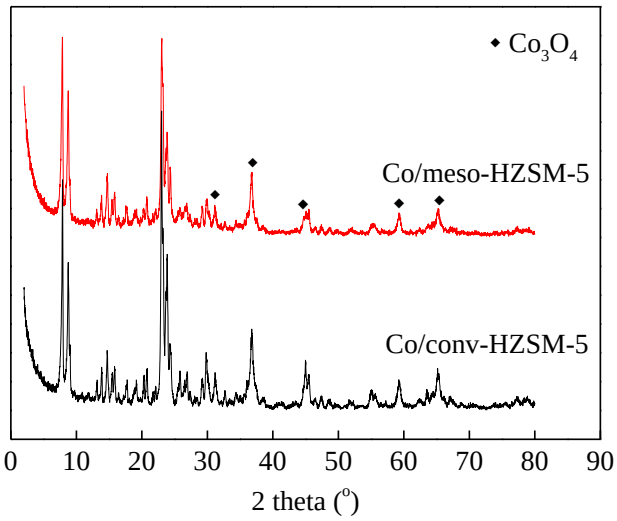

Fig. 4.2. XRD patterns of conv-HZSM-5 and meso-HZSM-5.

Fig. 4.3 shows the nitrogen adsorption and desorption isotherms of conv-HZSM-5 and meso-HZSM-5 samples. The conv-HZSM-5 exhibits type-I isotherm, a typical characteristic of microporous material. As compared, the isotherm of meso-HZSM-5 sample reveals a type-IV isotherm. It contains a hysteresis loop at relative pressures higher than P/P_0= 0.4, indicating the existence of mesopores. The pore size distribution of conv-HZSM-5 and meso-HZSM-5 obtained by using BJH method is displayed in Fig. 4.3b. For meso-HZSM-5 sample, an obvious mesopore size appears at 23.7 nm. These findings suggest that mesoporous HZSM-5 zeolite was one-step synthesized successfully as designed with the combination of micro-template (TPAOH) and meso-template (F127) as dual templates.

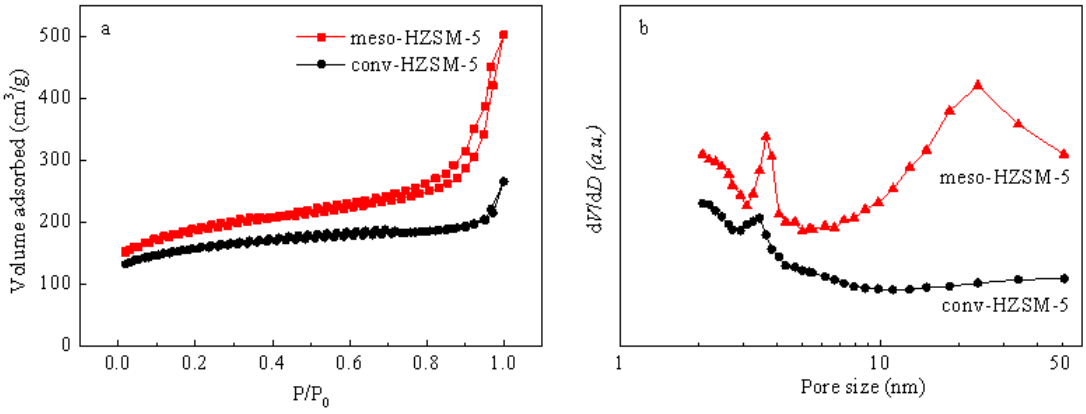

Fig. 4.3. N_2 sorption isotherms and pore size distribution of the conv-HZSM-5 and meso-HZSM-5.

The BET surface areas and pore volumes of samples are listed in Table 4.1. For the calcined meso-HZSM-5 sample, the BET surface area, especially micropore surface area obviously decrease if compared with that of the conv-HZSM-5. It is clear that the micropore and mesopore surface areas of the meso-HZSM-5 catalyst are 286 and 292 m^2/g respectively, indicating the coexistence of micropores and mesopores. In addition, the meso-HZSM-5 exhibits a large mesopore volume with 0.62 cm^3/g along with enhanced mesopore surface area, suggesting the generation of mesopores.

Table 4.1 Summary of the textural properties of different samples.

Sample	S(m^2/g)[a]			V(cm^3/g)			XRD (nm) [g]	Acidic amount
	Total	Micro[b]	Meso[c]	Total[d]	Micro[e]	Meso[f]	Co_3O_4	(mm/g)
conv-HZSM-5	615	415	200	0.48	0.23	0.25	16.1	2.02
meso-HZSM-5	578	286	292	0.78	0.16	0.62	12.7	2.26

[a] BET surface area.

[b] Microporous surface area evaluated by the *t*-plot method.

[c] Mesoporous surface area evaluated by the *t*-plot method.

[d] Total pore volume estimated from the adsorbed amount at $P/P_0 = 0.995$.

[e] Micropore volume evaluated by the *t* -plot method.

[f] Mesopore volume calculated as $V_{Meso} = V_{Total} - V_{Micro}$.

[g] Co_3O_4 crystallite size derived from XRD, applying the Scherrer equation.

The SEM and TEM images of the meso-HZSM-5 after hydrothermal treatment are displayed in Fig. 4.4. The SEM image presents uniform spherical shape with a

size around 500 nm. In addition, TEM image (Fig. 4.4b) shows the mesopores of 10-20 nm with combined micropores, indicating the presence of hierarchical pore structure, which will show an important effect on promoting the diffusion behavior of the reactants and the products.

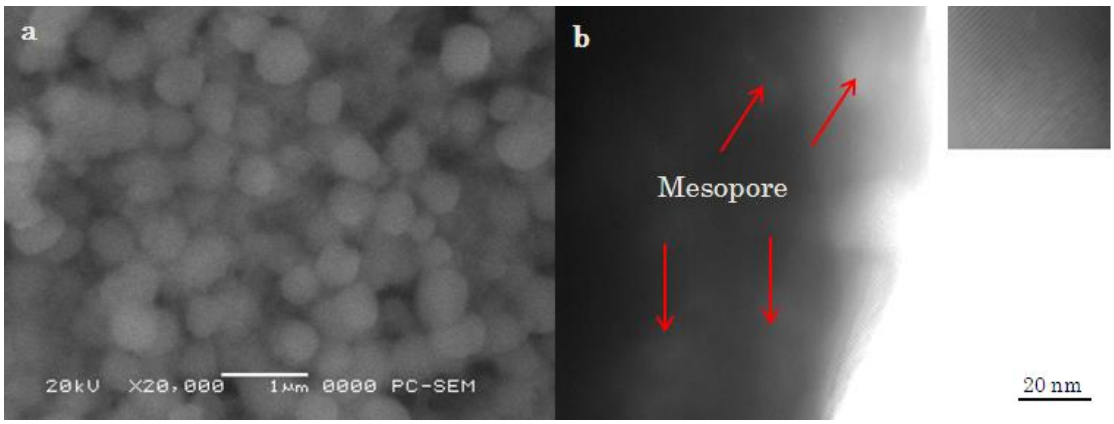

Fig. 4.4. SEM (a) and TEM (b) images of the obtained meso-HZSM-5.

The acidic properties of conv-HZSM-5 and meso-HZSM-5 samples are measured by NH_3-TPD in Fig. 4.5. The ammonium desorption profile of meso-HZSM-5 is similar to conv-HZSM-5. Both of the samples show three acid sites at 146, 242 and 310 ^oC, corresponding to weak acid sites, moderate acid sites and strong acid sites, respectively. As compared with those of the conv-HZSM-5, the weak acid strength increase significantly, but the moderate and strong peaks of meso-HZSM-5 decrease, probably due to the slightly amorphous nature of the mesopores walls［20,21］. The results are consistent with the results of XRD analysis. Catalyst acidity determined from TPD peak area is summarized in Table 4.1. This result indicates that acid property of meso-HZSM-5 enhanced to compare the conv-HZSM-5.

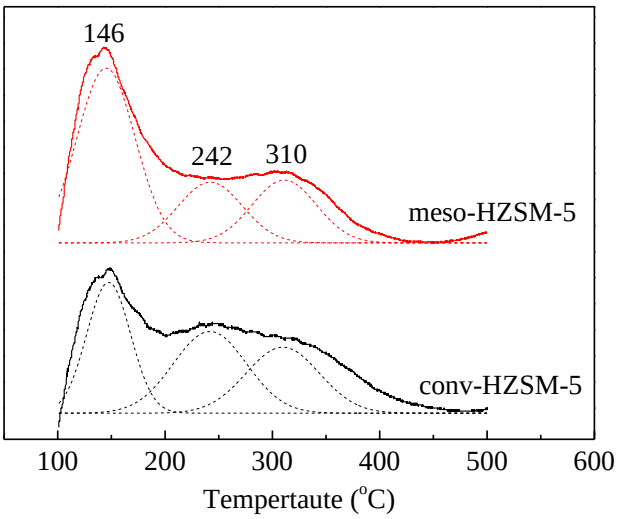

Fig. 4.5. NH_3-TPD profiles of conv-HZSM-5 and meso-HZSM-5.

The hierarchical structure of the HZSM-5 catalyst has an important effect on the diffusion behavior of reactants and products in catalytic process, which affects not only the catalytic activity but also the product selectivity [22]. FTS performances and product distribution over different catalysts are presented in Table 4.2 and Fig. 4.6. The conventional HZSM-5 supported Co catalyst (Co/conv-HZSM-5) exhibits 75.9 % CO conversion and a wide FTS product distribution with $C_{1\text{-}22}$. Contrarily, Co/meso-HZSM-5, the hierarchical HZSM-5 supported cobalt catalyst, gives higher CO conversion (79.0 %) and a narrow product distribution ranging from $C_{1\text{-}18}$ with lower 13.4 % CH_4 selectivity. At the same time, its selectivities of isoparaffin and C_{5+} hydrocarbons are increased significantly. Furthermore, the gasoline components ($C_{5\text{-}11}$) selectivity of 65.4 % is also increased if compared to that of the conventional catalyst (56.6 %). These findings are due to an enhancement in the diffusion efficiency of hydrocarbons and syngas inside the mesoporous zeolite channels. The secondary reactions, including hydrocracking and isomerization of the primary hydrocarbons, proceed more quickly over acidic sites at mesoporous channels in the hierarchical zeolite. Moreover, the C_{18+} hydrocarbons are totally suppressed on Co/meso-HZSM-5 catalyst, accompanied by a sharp anti-ASF law product distribution. These results suggest that the increased pore size of the support tunes successfully the hydrocarbon

distribution, changing the selectivities of isoparaffin and olefin.

Table 4.2 Tuned the FTS performance of different catalysts[a]

Catalyst	Conv. (%)	Product selectivity (%)							
	CO	CH_4	CO_2	n-papaffin	olefin	isoparaffin	C_{5-11}	C_{5+}	C_{iso}/C_n[b]
Co/conv-HZSM-5	75.9	14.8	1.7	52.8	30.9	16.2	56.6	70.7	0.50
Co/meso-HZSM-5	79.0	13.4	2.3	47.0	29.1	23.8	65.4	74.1	0.82

[a] Reaction conditions: Catalyst weight, 0.5 g; T, 240 ^oC; P, 1.0 MPa; H_2/CO, 2; $W_{Catalyst}/F$, 10 gh/mol.

[b] C_{iso}/C_n is the ratio of isoparaffin to paraffin of C_{4+}.

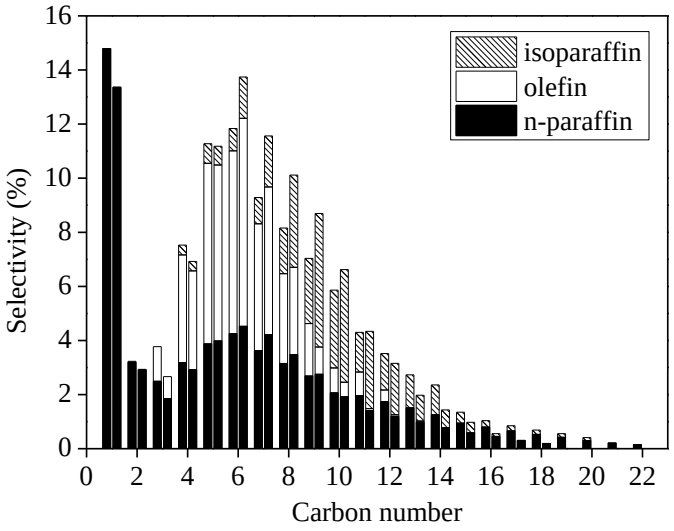

Fig. 4.6. FTS product distribution: *left*, Co/conv-HZSM-5; *right*, Co/meso-HZSM-5.

4.4 Conclusions

One-step synthesis of the hierarchical HZSM-5 with micropore and mesopore structure was prepared by using TPAOH and F127 as dual templates through a steam-assisted conversion process. The hierarchical HZSM-5 supported Co catalyst was employed to catalyze FTS reaction for direct synthesis of isoparaffin, exhibiting higher CO conversion and C_{5+} selectivity, compared with the conventional HZSM-5 supported Co catalyst. The C_{5-11} selectivity reached the highest 65.4 % and became the main hydrocarbon products due to optimized hydrocracking and isomerization function afforded by the hierarchical zeolite supports. Therefore, tuning the selectivity

of FTS products was realized using the hierarchical HZSM-5 supported cobalt catalyst. Moreover, the formation of C_{18+} hydrocarbons was completely suppressed. The hierarchical HZSM-5 support structure played a role in enhancing CO conversion and tuning the product distribution through FTS reaction.

References

[1] C. Li, Y. Wang, B. Shi, J. Ren, X. Liu, Y. Wang, Y. Guo, Y. Guo, G. Lu, ***Micropor. Mesopor. Mater.*** 117 (2009) 104-110.

[2] J. Zhou, Z. Hua, Z. Liu, W. Wu, Y. Zhu, J. Shi, ***ACS Catal.*** 1 (2011) 287-291.

[3] H. Liu, S. Yang, J. Hu, F. Shang, Z. Li, C. Xu, J. Guan, Q. Kan, ***Fuel Process. Technol.*** 96 (2012) 195-202.

[4] L.H. Chen, X.Y. Li, J.C. Rooke, Y.H. Zhang, X.Y. Yang, Y. Tang, F.S. Xiao, B.L. Su, ***J. Mater. Chem.*** 22 (2012) 17381-17403.

[5] L. Zhao, J. Gao, C. Xu, B. Shen, ***Fuel Process. Technol.*** 92 (2011) 414-420.

[6] H. Zhu, Z. Liu, Y. Wang, D. Kong, X. Yuan, Z. Xie, ***Chem. Mater.*** 20 (2008) 1134-1139.

[7] J. Lee, U.G. Hong, S. Hwang, M.H. Youn, I.K. Song, ***Fuel Process. Technol.*** 108 (2013) 25-30.

[8] I. Schmidt, A. Boisen, E. Gustavsson, K. Stahl, S. Pehrson, S. Dahl, A. Carlsson, C.J.H. Jacobsen, ***Chem. Mater.*** 13 (2001) 4416-4418.

[9] A.H. Janssen, I. Schmidt, C.J.H. Jacobsen, A.J. Koster, K.P. de Jong, ***Micropor. Mesopor. Mater.*** 65 (2003) 59-75.

[10] H.S. Cho, R. Ryoo, ***Micropor. Mesopor. Mater.*** 151 (2012) 107-112.

[11] Y. Tao, Y. Hattori, A. Matumoto, H. Kanoh, K. Kaneko, ***J. Phys. Chem. B*** 109 (2005) 194-199.

[12] H.L. Chum, R.P. Overend, ***Fuel Process. Technol.*** 71 (2001) 187-195.

[13] X. Huang, B. Hou, J. Wang, D. Li, L. Jia, J. Chen, Y. Sun, ***Appl. Catal. A Gen.*** 408 (2011) 38-46.

[14] J. Sun, C. Xing, H. Xu, F. Meng, Y. Yoneyama, N. Tsubaki, ***J. Mater. Chem. A*** 1 (2013) 5670-5678.

[15] J. Sun, X. Li, A. Taguchi, T. Abe, W. Niu, P. Lu, Y. Yoneyama, N. Tsubaki, ***ACS Catal.*** (2013) 1-8.

[16] Y.P. Li, T.J. Wang, C.Z. Wu, H.B. Li, X.X. Qin, N. Tsubaki, ***Fuel Process. Technol.*** 91 (2010) 388-393.

[17] Y. Yoneyama, J. He, Y. Morii, S. Azuma, N. Tsubaki, ***Catal. Today*** 104 (2005) 37-40.

[18] X. Li, K. Asami, M. Luo, K. Michiki, N. Tsubaki, K. Fujimoto, ***Catal. Today*** 84 (2003) 59-65.

[19] J. Bao, J. He, Y. Zhang, Y. Yoneyama, N. Tsubaki, ***Angew. Chem. Int. Ed.*** 47 (2008) 353-356.

[20] A.A. Rownaghi, F. Rezaei, J. Hedlund, ***Micropor. Mesopor. Mater.*** 151 (2012) 26-33.

[21] L. Xu, S. Wu, J. Guan, H. Wang, Y. Ma, K. Song, H. Xu, H. Xing, C. Xu, Z. Wang, Q. Kan, ***Catal. Commun.*** 9 (2008) 1272-1276.

[22] K. Cheng, J. Kang, S. Huang, Z. You, Q. Zhang, J. Ding, W. Hua, Y. Lou, W. Deng, Y. Wang, ***ACS Catal.*** 2 (2012) 441-449.

Chapter 5 Hierarchical zeolite Y supported cobalt as bifunctional catalyst for the tuning product selectivity in Fischer-Tropsch synthesis reaction

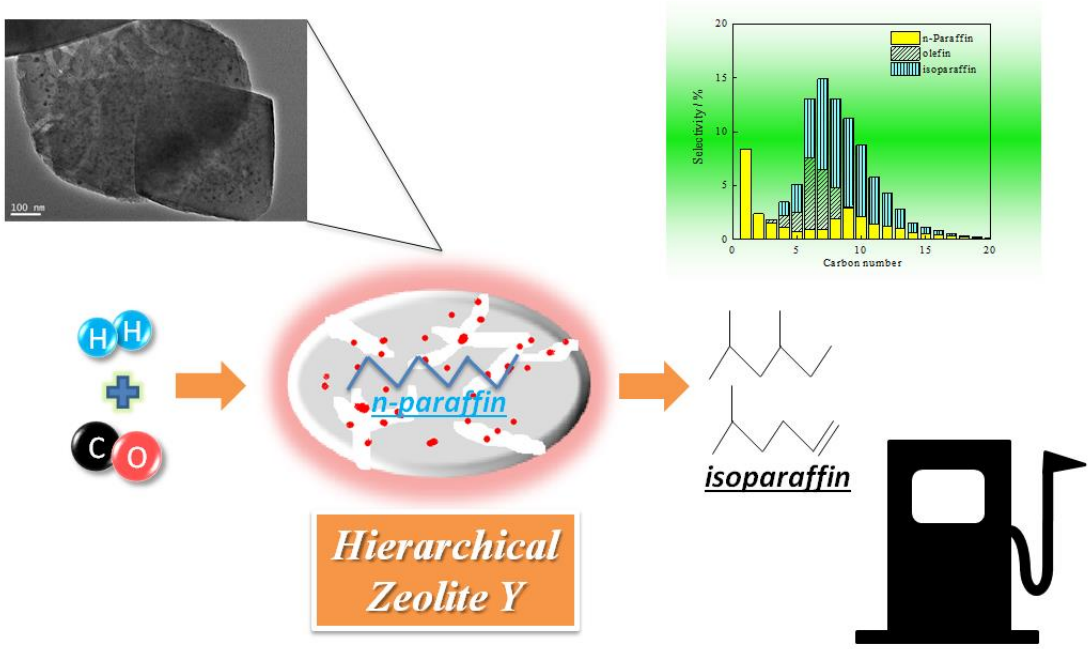

Abstract

A two-step process consisting of acid leaching and base leaching was applied to introduce mesopores on a commercially zeolite Y. Compositional, textural, morphological, structural, and acidity studies performed on hierarchical zeolite confirmed the presence of mesopore with zeolitic microporous walls. The analysis results showed that the surface area, pore volume and pore size of the hierarchical zeolite Y (Y-AB*x*, "*x*" stands for base leaching time) increased with increasing the base leaching time. The hierarchical zeolite Y supported Co as catalysts were employed to catalyze the hydrogenation of carbon monoxide in FTS reaction. The CO conversion and C_{5-11} selectivity of Co/AB*x* catalysts increased significantly as compared with the pristine Y supported Co catalyst. The isoparaffin selectivity of Co/AB4 reached the highest 52.3 %. Middle hydrocarbons had become the main FTS products due to the optimized hydrocracking and isomerization function afforded by the hierarchical zeolite Y.

Keywords: Hierarchical, Zeolite Y, Mesopore, Fischer-Tropsch synthesis, Isoparaffin.

5.1 Introduction

Zeolite, with unique micropore size, high thermal stability, high acidity and good thermal stability, is widely applied as catalysts or catalyst supports in numerous technical applications [1-3]. In general, the pore size and cavities of the zeolite channels are less than 0.8 nm and 1.5 nm, respectively [4,5]. Therefore, the narrow zeolite pores and channels lead to severe transport limitation for reactants and products in catalytic reactions [6,7].

In order to overcome this disadvantage, hierarchical zeolite with combined mesopores and zeolitic microporous walls, as highly active catalyst, has been studied deeply in recent years[8,9]. The general preparation methods for hierarchical zeolite are steaming, acid leaching (dealumination) or base leaching (desilication), templating and chemical treatment [7]. Sasaki et al. show that the dealumination led to the formation of mesoporous channels [10]. The application of desilicated ZSM-5 zeolite supported metal catalyst for direct gasoline synthesis from syngas has been deeply studied [11-16]. More recently, various carbon templates are used to introduce mesopores to the zeolite crystals [8,17-22]. For mesoporous zeolite-based catalysts, Bao and co-workers demonstrate that the mesoporous ZSM-5 loaded Mo catalysts showed an excellent catalytic performance for methane aromatization [23]. Li et al. prove that the mesoporous mordenite had better catalytic activity than conventional microporous mordenite in the alkylation of benzene with benzyl alcohol [24]. Wang et al. report high isoparaffin selectivity in Fischer-Tropsch synthesis (FTS) over the mesoporous ZSM-5 loaded noble metal catalyst [25]. However, in comparison with low cost iron and cobalt catalysts, the Ru catalyst with a small loading amount can not exhibit considerable reaction activity.

FTS reaction is a promising process to produce ultra clean liquid fuel by CO hydrogenation, which is also very important to deal with the recent oil crisis and environment protection [26-30]. It is well known that the FTS products are mostly linear paraffin and few α-olefin, and their distribution strictly follows the Anderson-Schultz-Flory (ASF) law [13,14,25,31,32]. As well known, the pore structure and acidity of catalyst support can affect FTS reaction rate and product

distribution. In recent years, researchers have devoted to selectively synthesize hydrocarbons with a narrow distribution, especially in the range of gasoline [16,33-35]. Zeolite Y with the faujasite (FAU) structure, as an excellent catalyst for cracking reaction, has been extensively used in fluid catalytic cracking (FCC) process [36]. However, the catalytic reaction rate is limited severely by the microporous channels of zeolite Y [7]. Herein, the development of mesoporous catalysts with zeolitic microporous walls is necessary.

In this paper, we designed a hierarchical zeolite Y supported cobalt catalyst for tuning the selectivity of FTS products. The hierarchical zeolite Y, simultaneously with micropores and mesopores, was readily prepared using a facile acid leaching and followed base leaching procedure. The acid leaching to zeolite Y not only enhanced its structure stability, but also improved its catalytic activity. In addition, the followed base leaching could remove partly some silicon from zeolite framework, forming the mesoporous structure. In this hierarchical zeolite Y structure, the micropores could provide a large surface area, high cobalt dispersion as well as enough acidic sites, while the mesoporous structure facilitated the diffusion of reactants and products.

5.2 Experimental Section

5.2.1 Catalyst preparation

The hierarchical zeolite Y was obtained by a sequential dealumination and desilication process. First, the pristine zeolite Y (commercial H-Y zeolite, Si/Al = 3.05, TOSOH CO.) was treated with a 0.17 M citric acid solution at 80 ^{o}C for 4 h, subsequently washed with deionized water, dried at 120 ^{o}C overnight and calcined in air at 550 ^{o}C for 3 h. The obtained sample was denoted as Y-A.

The pristine zeolite Y was also prepared using a 0.1 M NaOH aqueous solution for 1 h, followed by washing, drying, and calcination at 550 ^{o}C for 3 h. The calcined sample was further exchanged using ion-exchange method in $NH_4 \cdot NO_3$ aqueous solution. After the ion-exchanging, the solid product was obtained by filtration, followed by washing, drying, and calcination at 550 ^{o}C for 5 h to obtain H-type

zeolite Y. The final sample was named as Y-B.

The dealuminized zeolite Y (Y-A) was further leached with 0.1 M NaOH aqueous solution for 0.25, 1, 4 and 6 h, respectively. The sample was filtered, washed with deionized water, dried at 120 ^{o}C overnight and calcined in air at 550 ^{o}C for 3 h. Finally, the combination of acid and base treated zeolite was exchanged in $NH_4 \cdot NO_3$ solution, and then calcined at 550 ^{o}C for 5 h to get H-type zeolite Y. The hierarchical zeolite Y was denoted as Y-AB*x* (*x* = 0.25, 1, 4 and 6) where the "*x*" stands for the leaching time by NaOH solution.

The catalysts with the Co loading amount of 10 wt% were prepared by an incipient wetness impregnation (IWI) method on the hierarchical zeolite Y (Y-A, Y-B and Y-AB*x* samples) with the aqueous solution of cobalt nitrate. Finally, the wet catalyst was dried at 120 ^{o}C overnight and then calcined in air at 400 ^{o}C for 2 h. These catalysts were named Co/Y-A, Co/Y-B and Co/Y-AB*x* (*x* = 0.25, 1, 4 or 6), respectively. The pristine zeolite Y (Y-P) supported cobalt catalyst, as reference catalyst, was also prepared by IWI method and denoted as Co/Y-P.

5.2.2 Catalyst characterization

The crystalline structure of the samples was measured by X-ray diffraction (XRD) with a Rigaku RINT 2400 diffractometer employing Cu Kα radiation. All samples were scanned at 40 kV and 40 mA. The relative crystallinity (percentage crystalline material) of the zeolite was also determined by X-ray diffraction.

The Si/Al molar ratio of the samples was determined by energy dispersive X-ray spectroscopy (EDX-700, Shimadzu).

The nitrogen adsorption and desorption measurement of the samples were performed on a Micromeritics 3Flex analyzer (Micromeritics Instrument CO.). The surface area of samples was determined by the Brunauer-Emmett-Teller (BET) method. The pore size distribution of micropore was determined by HK method. The pore size distribution of mesopores was obtained from the desorption branch by the Barrett-Joyner-Halenda (BJH) method. The surface area and volume of micropore

were determined by the *t*-plot method. Mesoporous surface area was also evaluated by the *t*-plot method.

Transmission electron microscopy (TEM) measurements were performed on a JEOL JEM-2100 UHR at an acceleration voltage of 200 kV.

H_2 temperature programmed reduction (H_2-TPR) and NH_3 temperature programmed desorption (NH_3-TPD) experiments were performed in a flow apparatus on a BELCAT-B-TT (BEL CO.) instrument. In a typical H_2-TPR experiment, 0.03 g catalyst was pretreated at 150 ^oC in a quartz-made microreactor under flowing He for 1 h, followed by cooling to 50 ^oC. Then, a H_2/Ar mixture (5 %H_2, 20 mL/min) was introduced into the reactor, and the temperature was linearly increased from 150 ^oC to 500 ^oC with a heating rate of 5 ^oC/min. The consumption H_2 was detected by gas chromatograph with a thermal conductivity detector (TCD).

For the NH_3-TPD analysis, the catalyst was first loaded in a quartz reactor in flowing He at 150 ^oC for 1 h and then the followed adsorption was performed by using a 5 %$NH_3$95 %He mixture flow with a speed of 20 mL/min at 80 ^oC for 20 min. The desorption process was proceeded with the treatment of saturated catalyst at 80 ^oC for 1 h. The gas desorption step was then implemented with the increased temperature from 100 ^oC to 500 ^oC at the rate of 5 ^oC /min in He (20 mL/min).

5.2.3 FTS reaction

FTS reaction was carried out in a flowing fixed-bed reactor at 260 ^oC under reaction pressure of 1.0 MPa. In brief, 0.5 g catalyst was loaded in the middle of the stainless steel reactor and reduced in situ at 400 ^oC in a flow of pure H_2 (80 mL/min) for 10 h prior to reaction. FTS reaction was implemented using syngas with the ratio of $H_2/CO = 2$ and the flow velocity of $W_{Catalyst}/F = 10$ gh/mol. An ice trap with octane as solvent was fixed between reactor and back pressure regulator to capture the heavy hydrocarbons. The heavy hydrocarbons were finally analyzed by an offline gas chromatograph (Shimadzu GC-2014, FID). The residual gaseous products effused from the ice trap were analyzed online by other two online gas chromatographs

(Shimadzu GC-8A, TCD and Shimadzu GC-14B, FID). The configuration of the reactor was showed in Scheme 5.1.

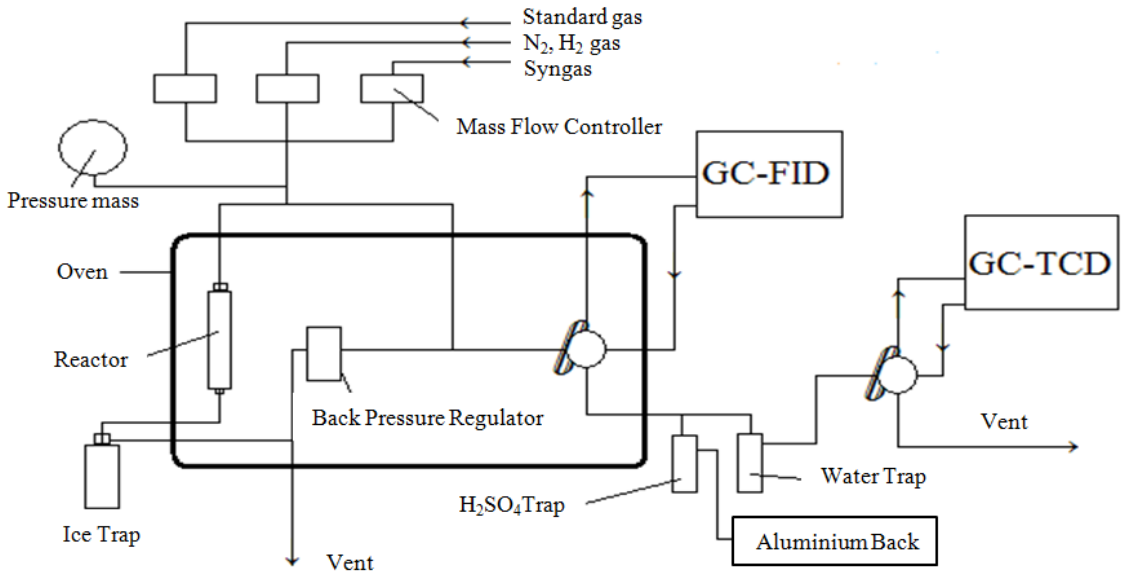

Scheme 5.1. Schematic diagram of FTS reaction

5.3 Results and Discussion

The XRD patterns of prepared samples are illustrated in Fig. 5.1. All samples exhibit similar peaks with the faujasite diffraction pattern. The crystallization intensity of the treated zeolite with acid, base or the sequential acid and base are weaker than that of the pristine zeolite Y (Y-P). The relative crystallinity of samples is also determined by XRD and listed in Table 5.1. It can be noticed that the crystallinity of samples after dealumination, desilication or by the sequential dealumination and desilication procedures decreases as compared with Y-P. However, there is an important loss of crystallinity for Y-AB6 sample, resulting in a relative drop of crystallinity down to 48.3 %, what indicates that the desilication by NaOH leaching for a long time with 6 h possibly led to partial amorphization of zeolite Y［4,37,38］.

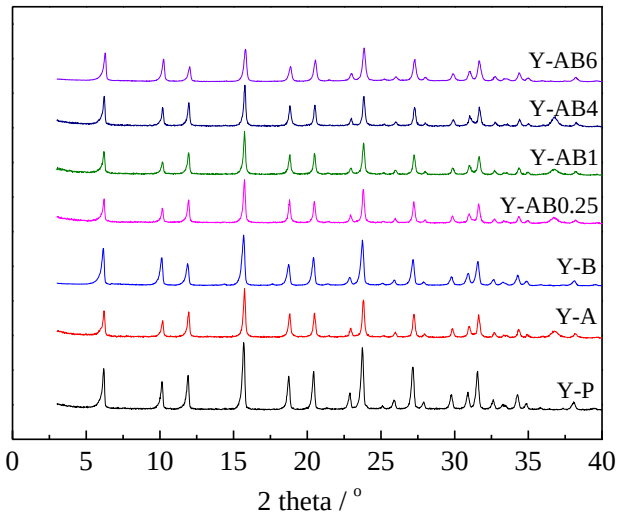

Fig. 5.1. XRD patterns of Y-P and hierarchical samples

Fig. 5.2 shows the nitrogen adsorption and desorption isotherms of the Y-P and hierarchical samples. The slopes of the isotherms of the hierarchical zeolite Y are larger than that of the pristine zeolite Y, indicating that mesopores were formed. After citric acid treated pristine zeolite Y, the hysteresis loop of Y-A sample enlarges slightly as compared with Y-P. It is interesting to note that the scope of the hysteresis loop enlarged obviously after base leaching. In addition, the scopes of the hysteresis loop for Y-AB*x* series samples enlarge gradually with increasing the base leaching time from 0.25 to 6 h. These results prove that the mesopores enlarge gradually with increasing the base leaching time.

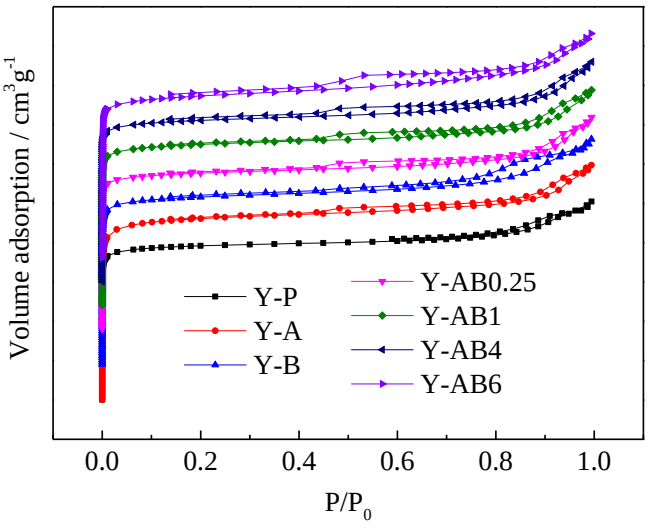

Fig. 5.2. N_2 sorption isotherms of mesoporous samples

The pore size distribution of the Y-P and hierarchical zeolite Y displays in Fig. 5.3. Fig. 5.3 *(left)* shows that the pristine zeolite Y has a bimodal pore distribution around 0.56 and 0.71 nm in microporous region, respectively. For a single step dealumination process on the pristine zeolite Y (Y-A), the peak around 0.56 nm is lower intensity as compared with Y-P, while the intensity of the peak at 0.71 nm enhances significantly. After desilication using NaOH leaching, Y-B and Y-P have a bimodal distribution around similar values with the degree of peak intensities. By using a two-step process consisting of the sequential acid leaching and base leaching on Y-P, Y-AB*x* series samples also exhibit a bimodal pore distribution, but shifts lower pore size to 0.69 nm, which may be due to the larger number of Brønsted acid sites (See Fig. 5.7, NH_3-TPD) [39]. According to the analysis by the BJH method, the pore diameter in the mesoporous region for Y-P and hierarchical zeolite Y show two pore sizes (Fig. 5.3 *(Right)*). For hierarchical zeolite Y, all of peaks enlarge clearly to compare the Y-P. For Y-P zeolite, two peaks appear at 3.6 and 16.4 nm. However, Y-B sample exhibits smaller pore size at 12.0 nm and relatively broader pore diameter distribution than that of Y-P. After citric acid leaching (Y-A), the peak at 3.6 nm is higher intensity as compared with Y-P. With increasing the NaOH leaching time on Y-A, the intensity of the peak at 3.6 nm further increase obviously. These results

suggest that the mesopores on zeolite Y could be generated effectively by using the combination of the acid leaching and base leaching. Moreover, the increase base leaching time is effective for generating mesopore on the zeolite Y, forming hierarchical mesoporous zeolite Y structure.

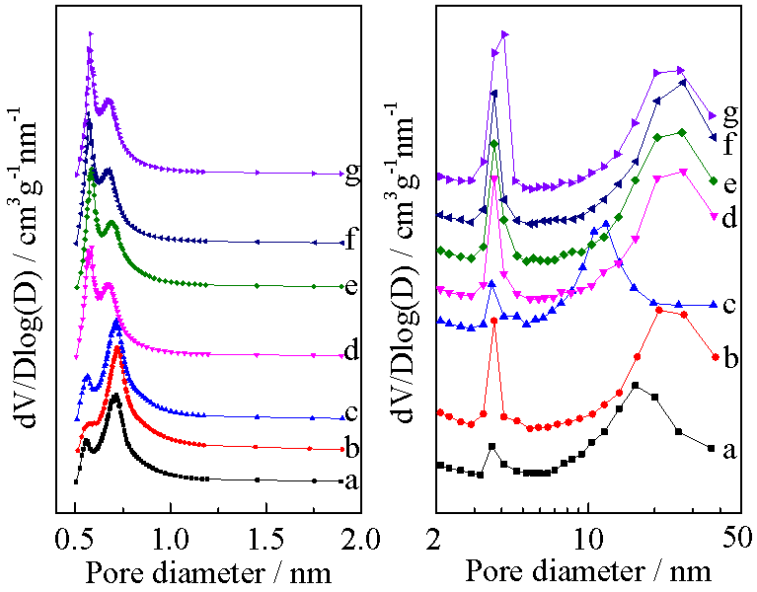

Fig. 5.3. Pore size distribution for the pristine and hierarchical zeolite Y by using *(left)* microporous region (HK method) and *(right)* mesoporous region (BJH method): a, Y-P; b, Y-A; c, Y-B; d, Y-AB0.25; e, Y-AB1; f, Y-AB4; d, Y-AB6.

The BET surface area, pore volume, Si/Al ratio and relative crystallinity of the pristine zeolite Y and hierarchical zeolite Y are listed in Table 5.1. It is clear that the mesopore surface area and mesopore volume of the Y-P catalyst are 61 m^2/g and 0.10 m^3/g respectively, indicating the coexistence of micropores and a small number of mesopores on the commercial pristine zeolite Y. As compared with Y-A, the BET surface area and total pore volume of Y-A (acid leaching) and Y-B (base leaching) increase obviously. With increasing the base leaching time from 0.25 to 6 h on Y-A, the mesopore surface area and mesopore volume of Y-AB*x* samples increase as compared with Y-P, suggesting the mesopores were created within the pristine zeolite Y by a sequential dealumination and desilication process. Selective dealumination during acid leaching (Y-A) results an increase the Si/Al ratio from 3.04 to 4.92 to compare with Y-P (Table 5.1). After desilication process, the Si/Al ratio of Y-AB*x* series samples decreases gradually with increasing the base leaching time.

Table 5.1 Summary of the textural properties of different samples

Sample	S(m^2/g)[a]			V(cm^3/g)			Si/Al ratio[g]	%Cryst[h]
	Total	Micro[b]	Meso[c]	Total[d]	Micro[e]	Meso[f]		
Y-P	589	528	61	0.38	0.28	0.10	3.04	100.0
Y-A	628	557	71	0.45	0.31	0.15	4.92	75.9
Y-B	643	564	79	0.43	0.30	0.13	2.84	82.8
Y-AB0.25	638	563	75	0.46	0.28	0.18	4.72	65.5
Y-AB1	619	541	78	0.48	0.28	0.20	4.69	63.4
Y-AB4	615	530	85	0.52	0.28	0.24	4.32	58.1
Y-AB6	607	509	98	0.57	0.28	0.29	4.05	48.3

[a] BET surface area.

[b] Microporous surface area evaluated by the *t*-plot method.

[c] Mesoporous surface area evaluated by the *t*-plot method.

[d] Total pore volume calculated by single point method at $P/P_0 = 0.99$.

[e] Micropore volume evaluated by the *t* -plot method.

[f] Mesopore volume calculated as $V_{Meso} = V_{Total} - V_{Micro}$.

[g] Si/Al mole ration determined by EDX analysis.

[h] The relative crystallinity value (%Cryst) calculated by XRD.

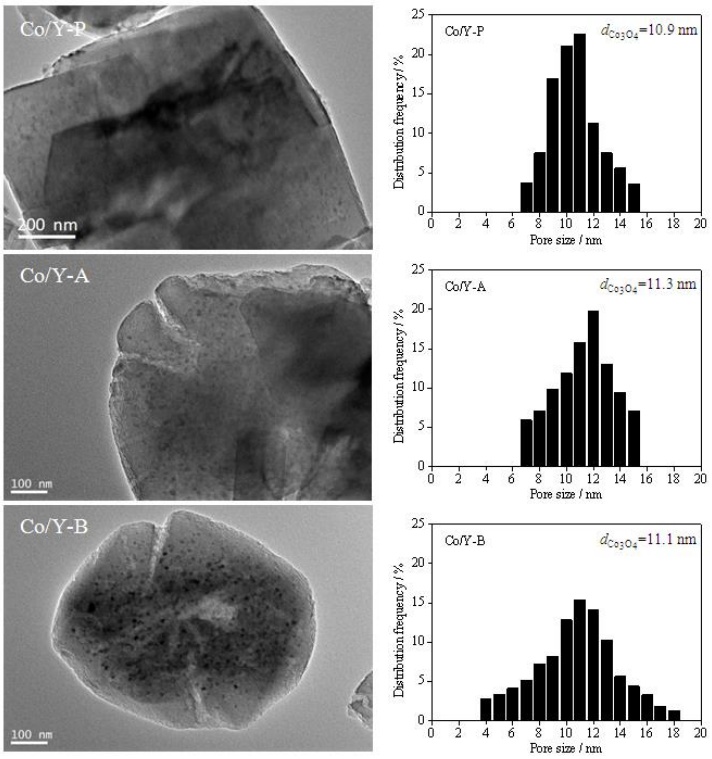

Fig. 5.4. TEM images and particle size distribution of Co/Y-P, Co/Y-A and Co/Y-B catalysts

TEM images and particle size distribution of the Co loaded on the pristine zeolite Y (Y-P) and hierarchical zeolite catalysts are provided in Fig. 5.4 and Fig. 5.5. A small

number of mesopores are introduced after acid leaching (Y-A) or base leaching (Y-B) on Y-P (Fig. 5.4). The average Co_3O_4 diameter was measured by TEM obvservation. All of the catalysts, Co_3O_4 particles are distributed in the range of 4-19 nm. In addition, the Co/Y-B catalyst exhibits a broad particle size distribution. With increasing the NaOH leaching time from 0.25 to 6 h used for the preparation of hierarchical zeolite Y samples (Fig. 5.5), the mesoporous channels increase significantly, which is an important effect on the promoting diffusion behavior of reactants and products in catalytic process. By sequential dealumination by citric acid and desilication by NaOH solution for 4 h on Y-P, as mesoporous zeolite supported Co catalyst (Co/Y-AB4), shows a smallest average particle size with 10.7 nm than that of other samples. However, when the NaOH leaching time increased to 6 h, the zeolite grain collapse slightly, which is in good agreement with the previous report［40］.

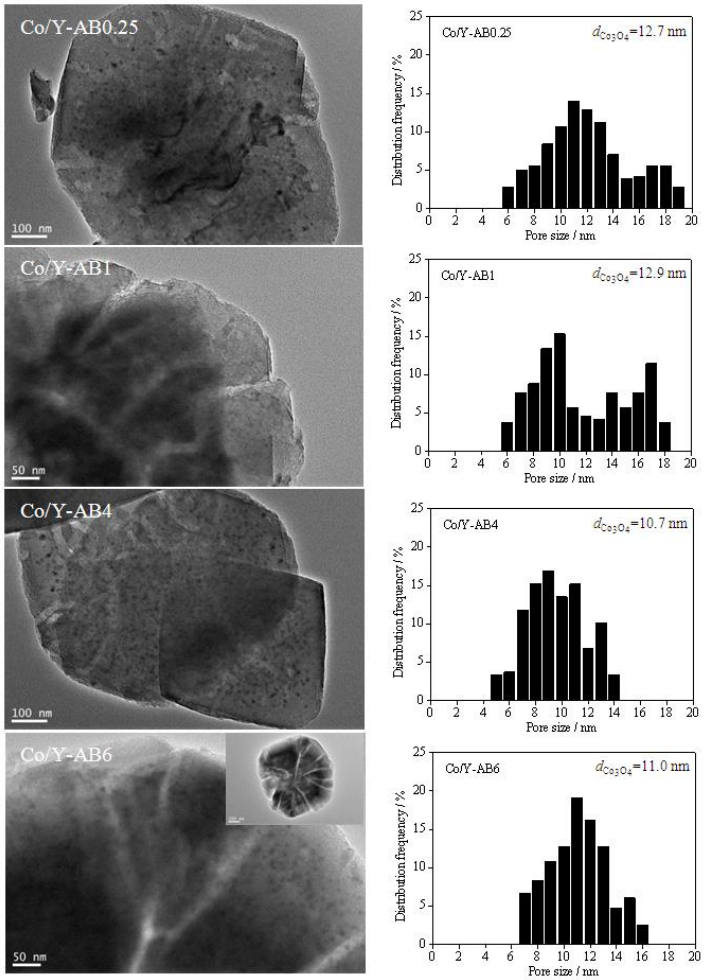

Fig. 5.5. TEM images and particle size distribution of Co/Y-AB*x* series catalysts

The reduction behaviors of the calcined Co/Y-P and hierarchical zeolite Y supported Co catalysts are studied using H_2-TPR (Fig. 5.6). The H_2-TPR profiles for all catalysts exhibit three main reduction peaks with the temperature at about 180-230 ^oC, 250-310 ^oC and 310-500 ^oC, respectively. The first reduction peak can be attributed to the reduction of the residual cobalt nitrate after calcination [41]. The second reduction peak is ascribed to the reduction of Co_3O_4 to CoO. The third reduction peak belongs to the reduction of CoO to Co^0 [42,43]. It can be seen that the reduction step of Co_3O_4 to CoO is fast (giving a sharp low-temperature peak) while the CoO reduction step is slow, resulting a broad profile [44]. However, the Co/Y-B catalyst exhibits a broad reduction peak above 310 ^oC, possibly due to a wide particle size distribution ranging from 4 to 18 nm (See Fig. 5.4).

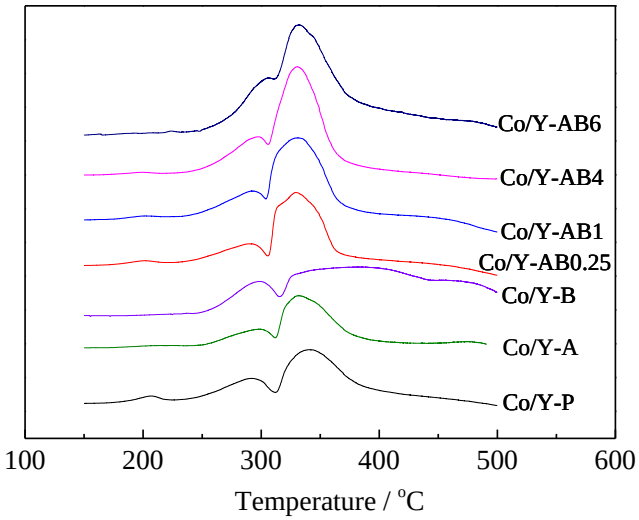

Fig. 5.6. H_2-TPR curve of the prepared catalysts

The acid properties of the prepared samples are measured by NH_3-TPD. The NH_3-TPD profiles of the Y-P, Y-A, Y-B and Y-AB*x* are showed in Fig. 5.7. The pristine zeolite Y exhibits two broad NH_3 desorption peaks. The lower temperature peaks at 180 ^oC is associated with the weak acidic sites weakly Brønsted acidic sites, Lewis acidic sites and terminal silanol groups [45]. The higher temperature peak at 420 ^oC is attributed to strong Brønsted and Lewis acidic sites. After base leaching on

the pristine zeolite Y, the higher temperature desorption peak increase obviously as compared with Y-P, suggesting that the strong Brønsted and Lewis acidic sites were increased through the desilication procedure. With increasing the leaching time of NaOH on Y-A sample used for the preparation of Y-AB*x* series samples, the strong Brønsted and Lewis acidic sites above 300 ^{o}C enhance obviously due to the decrease of Si/Al ratio (Table 5.1). Although, the details of the acidity and distribution of these acidic sites in zeolite is not clear now, it is reasonable to assume that the improved mass transfer of hierarchical zeolite one of important factors responsible for the different catalytic activity, owing to the presence of mesopores［3］.

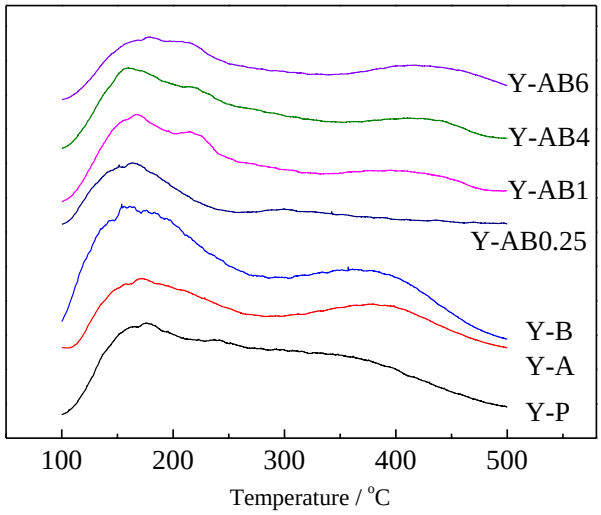

Fig. 5.7. NH_3-TPD curve of the prepared samples

As well known, the hierarchical structure of the catalyst is an important effect on the diffusion behaviors of the reactants and products in catalytic process, which affects the FTS activity and product selectivity［46］. The FTS reaction performances of the pristine and hierarchical zeolite Y supported Co particles catalysts are presented in Table 5.2. Before considering the catalytic performance of the sequential acid leaching and base leaching of Y-P supported cobalt metal catalysts, we firstly compare the FTS reaction results of the single acid leaching or base leaching on Y-P. As shown in Table 5.2, the CO conversion of the Co/Y-P catalyst is only 50.2 %, much lower than that of Co/Y-A (66.2 %) and Co/Y-B (69.7 %). At the same time, the isoparaffin

selectivity also enhances significantly to compare with Co/Y-P, which can be attributed to the secondary reactions, including hydrocracking and isomerization of the primary hydrocarbons over zeolite acidic sites［16,47］. Moreover, the CH_4 selectivity over Co/Y-P with 21.9 %, is two times higher than that of Co/Y-A and Co/Y-B catalysts. It is attributed to contribute the CH_4 formation in FTS reaction through the existed more micropore cavities of the pristine zeolite Y as compared with hierarchical Co/Y-A or Co/Y-B［12］.

Table 5.2 Catalytic performance of the pristine and hierarchical zeolite Y supported cobalt catalysts[a]

Catalyst	Conv./%	Sel./%								
	CO	CO_2	CH_4	C_{2-4}	C_{5-11}	C_{12+}	C_n	$C_=$	C_{iso}	C_{iso}/C_n[b]
Co/Y-P	50.2	1.1	21.9	13.6	59.2	5.3	51.7	18.6	29.8	1.40
Co/Y-A	66.2	1.5	10.8	13.9	69.4	3.4	41.9	7.3	50.9	1.97
Co/Y-B	69.7	2.9	11.9	13.6	65.2	9.3	46.4	10.1	43.5	1.47
Co/Y-AB0.25	66.3	1.9	14.7	10.7	67.6	7.0	46.0	18.1	35.9	1.46
Co/Y-AB1	75.7	3.5	11.4	10.2	67.0	11.4	39.1	18.2	42.6	1.89
Co/Y-AB4	75.9	1.8	8.4	7.7	71.8	12.1	29.5	18.3	52.3	3.06
Co/Y-AB6	66.5	2.0	14.5	12.8	65.0	7.7	46.2	13.9	39.9	1.58

[a] Reaction conditions: Catalyst weight, 0.5 g; T, 260 ^oC; P, 1.0 Mpa; H_2/CO, 2; $W_{Catalyst}/F$, 10 gh/mol.

[b] C_{iso}/C_n is the ratio of isoparaffin to paraffin of C_{4+}.

The CO conversion and hydrocarbons selectivity of the two-step process consisting of acid leaching and followed base leaching of Y zeolite (Co/Y-AB*x*) supported cobalt metal catalysts are also compared in Table 5.2. The CO conversion increases gradually with the increase of leaching time from 0.25 to 4 h, but the CO_2 selectivity is stability on the Co/Y-AB*x* series catalysts, indicating a very low water-gas shift activity under the reaction conditions. However, the CO conversion decrease significantly with further increasing the base leaching time to 6 h on Y-A. It is attributed to the partial damage for zeolite structure (See Fig. 5.1 and Fig. 5.5). The C_{2-4} selectivity of Co/Y-AB*x* series catalysts decrease with increasing the base leaching time on Y-A, that is, increasing the pore size of the carrier (See Fig. 5.3) should contribute to weakening the effect of confinement in the mesoporous zeolite

channels. In addition, the C_{5-11} selectivity increases clearly with increasing the base leaching time. This is due to an enhancement of mesoporous zeolite channels. On the other hand, it can be partly attributed to the secondary reactions, including hydrocracking and isomerization of the heavy hydrocarbons over the acidic sites in the hierarchical zeolite Y. These results suggest that the increased pore size of mesoporous zeolite Y support leads to the formation of hydrocarbons toward with higher carbon number, being in agreement with Khodakov's report［48］. At the same time, the C_{12+} selectivity increases slightly with the enhanced pore size of the support due to the hydrocracking and isomerization of C_{12+} hydrocarbons on the acidic sites of zeolite Y.

In FTS reaction, zeolite Y acts as not only a support but also an excellent hydrocracking and isomerization catalyst owing to its acidic sites, special pores, cavities, and regular channels. Reaction results in Table 5.2 also show that isoparaffin can be synthesized directly via FTS reaction using the hierarchical zeolite Y supported cobalt catalysts. The isoparaffin selectivity enhances significantly with increasing the base leaching time on acid treated zeolite support (Y-A). The Y-AB4 supported cobalt catalyst (Co/Y-AB4) exhibits that the isoparaffin as the main products has the highest selectivity of 52.3 %. The hydrocarbon distribution of FTS reaction over Co/Y-P, Co/Y-A, Co/Y-B and Co/Y-AB*x* series catalysts has been showed in Fig. 5.8. Generally, FTS products are normal aliphatic hydrocarbons［49］. However, the selectivity of the isoparaffin is clearly enhanced on the Co/Y-AB*x* catalysts with hierarchical zeolite Y as the supports. More importantly, the light hydrocarbons of C_{1-4} are suppressed via the hierarchical structure.

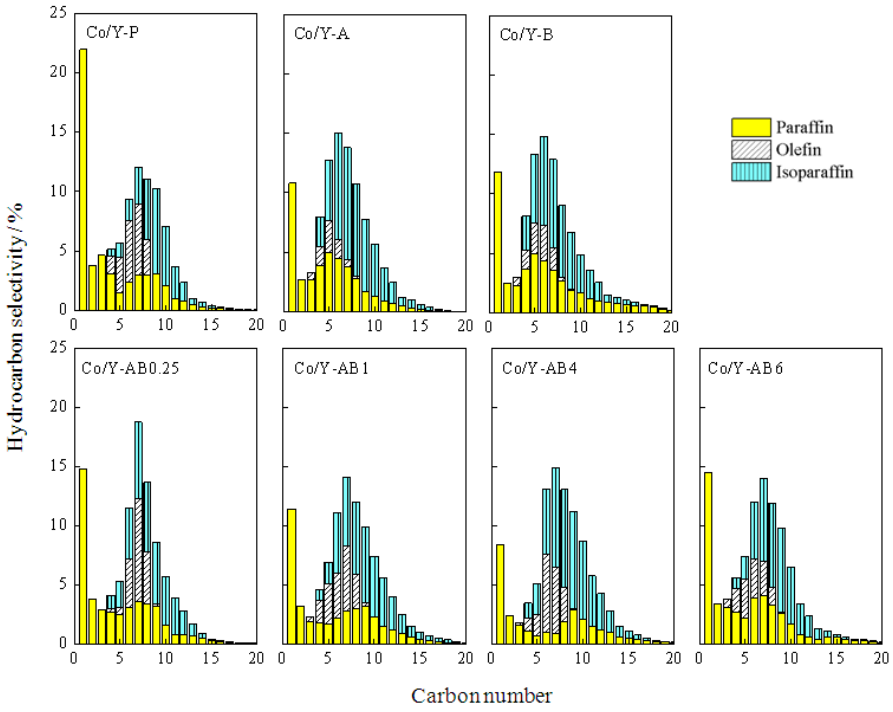

Fig. 5.8. Product distribution of the prepared catalysts

5.4 Conclusions

Hierarchical zeolite Y with intra-crystalline mesopores was obtained by a sequential acid and base leaching method. With increasing the base leaching time from 0.25 to 6 h on Y-A (citric acid treated pristine zeolite Y), the mesopore surface area and mesopore volume of Y-AB*x* samples increase as compared with the pristine zeolite Y. The CO conversion and C_{5+} selectivity of the hierarchical zeolite Y supported Co catalyst were much higher than that of conventional one (Co/Y-P). The isoparaffin selectivity reached the highest 52.3 % and became the main FTS products due to the optimized hydrocracking and isomerization function afforded by the hierarchical zeolite Y supports. Although the mesopores were also achieved after single acid or base treatment, both of the CO conversion and isoparaffin selectivity were lower than that of Co/AB4 catalyst. Therefore, tuning the selectivity of FTS products was realized easily using the hierarchical zeolite Y supported cobalt bifunctional as catalysts. This achievement further highlights a two-step process consisting of acid leaching and base leaching to prepare hierarchical zeolite in an industrial application.

References

[1] S. van Donk, A.H. Janssen, J.H. Bitter, K.P. de Jong, ***Catal. Rev.*** 45 (2003) 297-319.

[2] B. Louis, F. Ocampo, H.S. Yun, J.P. Tessonnier, M.M. Pereira, ***Chem. Eng. J.*** 161 (2010) 397-402.

[3] H. Tao, H. Yang, X. Liu, J. Ren, Y. Wang, G. Lu, ***Chem. Eng. J.*** 225 (2013) 686-694.

[4] J.C. Groen, S. Abello, L.A. Villaescusa, J. Perez-Ramirez, ***Micropor. Mesopor. Mater.*** 114 (2008) 93-102.

[5] Y.P. Guo, H.J. Wang, Y.J. Guo, L.H. Guo, L.F. Chu, C.X. Guo, ***Chem. Eng. J.*** 166 (2011) 391-400.

[6] J.C. Groen, L.A.A. Peffer, J.A. Moulijn, J. Perez-Ramirez, ***Colloid Surf. A Physicochem. Eng. Asp.*** 241 (2004) 53-58.

[7] K.P. de Jong, J. Zecevic, H. Friedrich, P.E. de Jongh, M. Bulut, S. van Donk, R. Kenmogne, A. Finiels, V. Hulea, F. Fajula, ***Angew. Chem. Int. Ed.*** 49 (2010) 10074-10078.

[8] L.H. Chen, X.Y. Li, J.C. Rooke, Y.H. Zhang, X.Y. Yang, Y. Tang, F.S. Xiao, B.L. Su, ***J. Mater. Chem.*** 22 (2012) 17381-17403.

[9] X. Meng, F. Nawaz, F.-S. Xiao, ***Nano Today*** 4 (2009) 292-301.

[10] Y. Sasaki, T. Suzuki, Y. Takamura, A. Saji, H. Saka, ***J. Catal.*** 178 (1998) 94-100.

[11] S. Sartipi, M. Makkee, F. Kapteijn, J. Gascon, ***Catal. Sci. Technol.*** 4 (2014) 893.

[12] S. Sartipi, M. Alberts, V.P. Santos, M. Nasalevich, J. Gascon, F. Kapteijn, ***ChemCatChem*** 6 (2014) 142-151.

[13] S. Sartipi, J.E. van Dijk, J. Gascon, F. Kapteijn, ***Appl. Catal. A Gen.*** 456 (2013) 11-22.

[14] S. Sartipi, K. Parashar, M.J. Valero-Romero, V.P. Santos, B. van der Linden, M. Makkee, F. Kapteijn, J. Gascon, ***J. Catal.*** 305 (2013) 179-190.

[15] S. Sartipi, K. Parashar, M. Makkee, J. Gascon, F. Kapteijn, ***Catal. Sci. Technol.*** 3 (2013) 572-575.

[16] K. Cheng, J. Kang, S. Huang, Z. You, Q. Zhang, J. Ding, W. Hua, Y. Lou, W. Deng, Y. Wang, ***ACS Catal.*** 2 (2012) 441-449.

[17] R.J. White, A. Fischer, C. Goebel, A. Thomas, ***J. Am. Chem. Soc.*** 136 (2014) 2715-2718.

[18] C. Xue, F. Zhang, L. Wu, D. Zhao, ***Micropor. Mesopor. Mater.*** 151 (2012) 495-500.

[19] H.S. Cho, R. Ryoo, ***Micropor. Mesopor. Mater.*** 151 (2012) 107-112.

[20] X. Wang, G. Li, W. Wang, C. Jin, Y. Chen, ***Micropor. Mesopor. Mater.*** 142 (2011) 494-502.

[21] R. Chal, C. Gerardin, M. Bulut, S. van Donk, ***ChemCatChem*** 3 (2011) 67-81.

[22] N. Chu, J. Yang, C. Li, J. Cui, Q. Zhao, X. Yin, J. Lu, J. Wang, ***Micropor. Mesopor. Mater.*** 118 (2009) 169-175.

[23] L. Su, L. Liu, J. Zhuang, H. Wang, Y. Li, W. Shen, Y. Xu, X. Bao, ***Catal. Lett.*** 91 (2003) 155-167.

[24] X. Li, R. Prins, J.A. van Bokhoven, ***J. Catal.*** 262 (2009) 257-265.

[25] J. Kang, K. Cheng, L. Zhang, Q. Zhang, J. Ding, W. Hua, Y. Lou, Q. Zhai, Y. Wang, ***Angew. Chem. Int. Ed.*** 50 (2011) 5200-5203.

[26] G. Yang, J. He, Y. Zhang, Y. Yoneyama, Y. Tan, Y. Han, T. Vitidsant, N. Tsubaki, ***Energy Fuel*** 22 (2008) 1463-1468.

[27] J. Bao, J. He, Y. Zhang, Y. Yoneyama, N. Tsubaki, ***Angew. Chem. Int. Ed.*** 47 (2008) 353-356.

[28] C. Xing, G. Yang, D. Wang, C. Zeng, Y. Jin, R. Yang, Y. Suehiro, N. Tsubaki, ***Catal. Today*** 215 (2013) 24-28.

[29] M. Yao, N. Yao, Y. Shao, Q. Han, C. Ma, C. Yuan, C. Li, X. Li, ***Chem. Eng. J.*** 239 (2014) 408-415.

[30] L.C. Almeida, F.J. Echave, O. Sanz, M.A. Centeno, G. Arzamendi, L.M. Gandia, E.F. Sousa-Aguiar, J.A. Odriozola, M. Montes, ***Chem. Eng. J.*** 167 (2011) 536-544.

[31] J. He, B. Xu, Y. Yoneyama, N. Nishiyama, N. Tsubaki, ***Chem. Lett.*** 34 (2005) 148-149.

[32] Q. Zhang, J. Kang, Y. Wang, ***ChemCatChem*** 2 (2010) 1030-1058.

[33] Y.L. Wang, B. Hou, J.G. Chen, L.T. Jia, D.B. Li, Y.H. Sun, ***Catal. Commun.*** 10 (2009) 747-752.

[34] Q.H. Zhang, J.C. Kang, Y. Wang, ***ChemCatChem*** 2 (2010) 1030-1058.

[35] X. Huang, B. Hou, J. Wang, D. Li, L. Jia, J. Chen, Y. Sun, ***Appl. Catal. A Gen.*** 408 (2011) 38-46.

[36] A. Corma, ***Chem. Rev.*** 95 (1995) 559-614.

[37] K. Tarach, K. Góra-Marek, J. Tekla, K. Brylewska, J. Datka, K. Mlekodaj, W. Makowski, M.C. Igualada López, J. Martínez Triguero, F. Rey, ***J. Catal.*** 312 (2014) 46-57.

[38] D. Verboekend, G. Vile, J. Perez-Ramirez, ***Cryst. Growth Des.*** 12 (2012) 3123-3132.

[39] L. Chen, R.K. Singh, P. Webley, ***Micropor. Mesopor. Mater.*** 102 (2007) 159-170.

[40] M. Ogura, S.Y. Shinomiya, J. Tateno, Y. Nara, M. Nomura, E. Kikuchi, M. Matsukata, ***Appl. Catal. A Gen.*** 219 (2001) 33-43.

[41] Y.G. Ji, Z. Zhao, A.J. Duan, G.Y. Jiang, J. Liu, ***J. Phys. Chem. C*** 113 (2009) 7186-7199.

[42] S.F. Mu, D.B. Li, B. Hou, L.H. Jia, J.G. Chen, Y.H. Sun, ***Energy Fuel*** 24 (2010) 3715-3718.

[43] J. Sun, W. Niu, A. Taguchi, T. Abe, Y. Yoneyama, N. Tsubaki, ***Catal. Sci. Technol.*** 4 (2014) 1260-1267.

[44] H. Xiong, Y. Zhang, K. Liew, J. Li, ***J. Mol. Catal. A Chem.*** 295 (2008) 68-76.

[45] N. Taufiqurrahmi, A.R. Mohamed, S. Bhatia, ***J. Nanopart. Res.*** 13 (2011) 3177-3189.

[46] X. Zhang, K. Tao, T. Kubota, T. Shimamura, T. Kawabata, K. Matsuda, S. Ikeno, N. Tsubaki, ***Appl. Catal. A Gen.*** 405 (2011) 160-165.

[47] A. Martinez, G. Prieto, ***Top. Catal.*** 52 (2009) 75-90.

[48] A.Y. Khodakov, A. Griboval-Constant, R. Bechara, V.L. Zholobenko, ***J. Catal.*** 206 (2002) 230-241.

[49] J. Sun, X. Li, A. Taguchi, T. Abe, W. Niu, P. Lu, Y. Yoneyarna, N. Tsubaki, ***ACS Catal.*** 4 (2014) 1-8.

Chapter 6 Novel iron based micro-capsule catalyst for the direct synthesis of middle isoparaffin from syngas

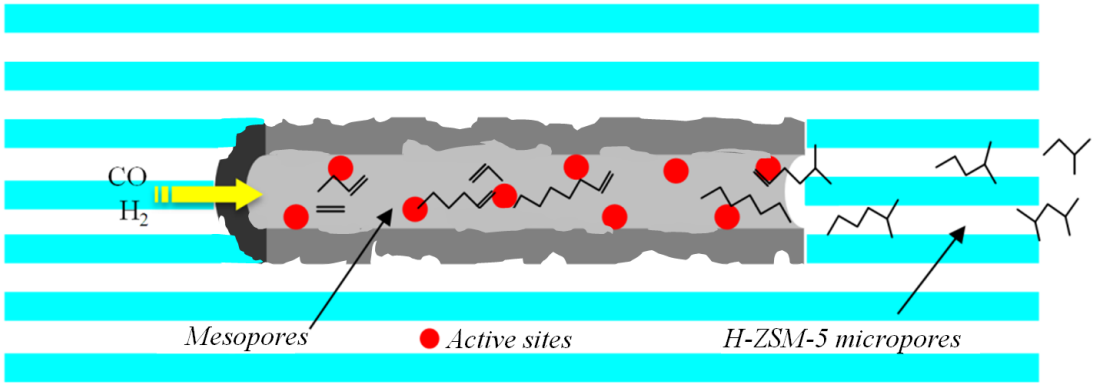

Abstract

A novel iron based micro-capsule catalyst with interior Fe/Silica *core* and exterior H-ZSM-5 *shell* was synthesized via in-situ crystallization route on Fe/SBA-15 catalyst by using steam-assisted crystallization (SAC) process and evaluated for direct synthesis of middle isoparaffin from syngas in a fixed bed reactor. Structure characterization indicated that the size of micro-capsule catalyst was about 1-2 um. Activity test results revealed that original Fe/SBA-15 catalyst exhibited a low selectivity of isoparaffin with 8.2 % and high selectivities of olefin and normal paraffin. But the as-prepared micro-capsule catalyst achieved an excellent performance for isoparaffin synthesis with the selectivity up to 46.5 %. Different from the zeolite coated cobalt catalysts, the high isoparaffin selectivity of micro-capsule catalyst was mainly attributed to the polymerization of the light olefin catalyzed by the H-ZSM-5 zeolite shell. Meanwhile, the physical mixture catalyst (Fe/SBA-15 and H-ZSM-5) exhibited lower isoparaffin selectivity with 33.9% than that of the micro-capsule catalyst. The spatial confinement effect of the micro-capsule catalyst plays an important role for the high selectivity of isoparaffin synthesis.

Keynote: Fischer-Tropsch Synthesis, Iron, Micro-Capsule Catalyst, Spatial Confinement Effect, Isoparaffin.

6.1 Introduction

The depletion of crude oil and the rapid growing demand of liquid fuels have attracted more interest for the synthesis of alternative fuels from the rich-reserved coal, natural gas and renewable biomass via Fischer-Tropsch synthesis (FTS) reaction[1]. Generally, the FTS reaction mainly produces normal hydrocarbons and some building-block chemicals such as lower olefin, which can not be directly used as the transportation fuels, especially for the extensively demanded gasoline[2, 3]. Additional hydrocracking and isomerization steps are usually employed for the production of gasoline in industry. But these steps increase the operating cost and complexity of the processes. So it is more promising for the direct synthesis of gasoline components (rich in middle isoparaffin) from syngas without extra processes.

Bifunctional catalysts with the combination of the conventional FTS catalyst and acidic zeolite, have been studied widely for direct synthesis of middle isoparaffin[4-9]. Until now, there are three kinds of bifunctional catalysts for direct synthesis of middle isoparaffin: physical mixture catalyst[10, 11], zeolite supported metal catalyst[12, 13], and the capsule or coating catalyst with the conventional FTS catalyst core and zeolite shell[14-16]. The physical mixture catalyst usually has a relative low selectivity of middle isoparaffin due to the random hydrocracking/isomerization of long chain hydrocarbons in acidic zeolite. Zeolite supported metal catalyst, as the active metal dispersed on acidic zeolite supports, exhibits a low conversion due to the strong metal support interaction (SMSI). Capsule catalyst is more effective for isoparaffin synthesis because of the spatial confinement effect and unique pore structure of the zeolite shell, which could enforce effectively the hydrocracking/isomerization of long chain hydrocarbons. Cobalt based capsule catalyst has been studied extensively for the direct isoparaffin synthesis[17, 18]. Fe based catalyst have much lower cost and methane selectivity than Co based catalyst, which are proper candidates for the capsule catalyst[19, 20]. Recently, our group reported a fused iron based capsule catalyst for isoparaffin synthesis, which was synthesized without organic template, giving a remarkably increase of

isoparaffin/normal paraffin ratio compared to the core catalyst (fused iron)[21]. However, more works are still needed to further increase the catalytic activity and middle isoparaffin selectivity for iron based capsule catalyst, as well as enhancing the diffusion of products due to the fused iron without pore structure. In order to enhance the catalyst activity and diffusion of products, iron based core catalyst with mesopore structure and large surface area is recommended. SBA-15 as an ordered mesoporous silica with large surface area, unique pore size and thermostability, is applied widely as modal support for FTS reaction[22-27]. Furthermore, it has been proved that the ordered pore silica supported catalysts exhibited superior performance to compare with the traditionally disordered silica catalysts in FTS, such as the high activity and stability due to the confinement effect of ordered pore channels[28, 29].

Zeolite with a highly thermal stability, ordered structure, high acidity and shape selectivity, has been applied widely as heterogeneous catalysts in the traditional petroleum-related processes and fine chemical industries[30-32]. So far, synthesizing zeolite membrane coated the core catalysts are usually prepared by the hydrothermal synthesis method[20, 33, 34] and physically adhesive method[14, 35]. However, hydrothermal synthesis method produces a lot of waste water. Moreover, it also limits the design and preparation of various zeolite shell coated core catalysts. The physically adhesive method, that is, the independent zeolite powders are directly pasted onto the core catalyst surface with adhesive. The prepared capsule catalyst by using the physically adhesive method can not exhibit a very high selectivity of gasoline. For these reasons, the steam-assisted crystallization (SAC) process as a new method to prepare capsule catalysts is desired.

In prior studies, the conventional capsule catalyst with the size scale of 1000-2000 um[16, 33, 36], this is a significantly technological interest to reduce the size of the capsule catalyst. Herein, we designed the Fe base micro-capsule catalyst with unique size about 1-2 um. The micro-capsule catalyst with Fe/Silica core and H-ZSM-5 zeolite shell via an in-situ crystallization route on Fe/SBA-15 catalyst by using the SAC process was first synthesized and applied in direct synthesis of isoparaffin from syngas via FTS reaction. The overall synthetic route is illustrated in

Fig. 6.1. In the first step, iron precursor was impregnated over ordered mesoporous silica (SBA-15). Subsequently, Fe/SBA-15 was dissolved partially in zeolite synthesis solution (Fig. 6.1c). After solvent evaporation, the obtained Fe/Silica dry gel (Fig. 6.1d) acted as the capsule catalyst of silicon source. Finally, Fe/Silica core catalyst was coated by H-ZSM-5 zeolite through the SAC method (Fig. 6.1e, Fe/Silica/SZ).

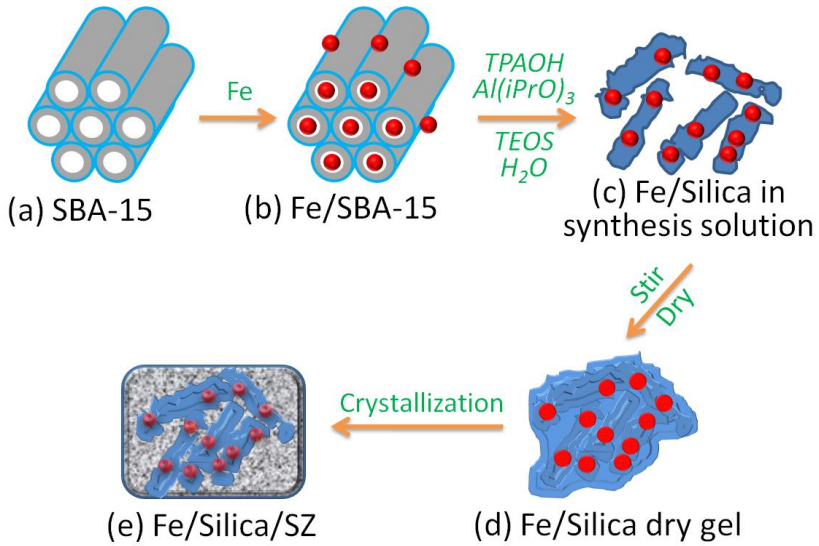

Fig. 6.1. Synthesis schematic route of iron based micro-capsule catalyst

6.2 Experimental Section

6.2.1 Catalyst preparation

The mesoporous SBA-15 was synthesized according to the procedure described by Zhao et al[37]. Briefly, 4.0 g P123 (Pluronic P123, EO:PO:EO = 20:70:20, MW=5800, Aldrich) was dissolved in 30 g of deionized water, followed the addition of 2 M HCl solution at 35 ^{o}C with stirring. Then, 8.5 g of tetraethyl orthosilicate (TEOS, 95.0 %, Wako) was added to the former solution. The obtained mixture was stirred at 35 ^{o}C for 20 h, subsequently kept in a closed Teflon vessel at 100 ^{o}C for 12 h. The solid product was filtered, washed with deionized water, dried at room temperature and calcained in air at 500 ^{o}C for 6 h with a heating rate of 1 ^{o}C/min.

The Fe/SBA-15 catalyst was prepared by impregnation of the SBA-15 support with $Fe(NO_3)_3 \cdot 9H_2O$ ethanol solution. The impregnated sample was first dried using rotary evaporator at 80 ^{o}C, and then further dried at 120 ^{o}C for 24 h. The dried sample

was calcined at 450 ^{o}C under air for 4 h to obtain the Fe/SBA-15 catalyst. The final Fe content of the catalyst was 27 wt%.

The micro-capsule catalyst with Fe/SBA-15 core and H-ZSM-5 shell was prepared by SAC method[38], and denoted as Fe/Silica/SZ. Firstly, Fe/SBA-15 (1 g) catalyst was added to 0.026 g aluminium isopropoxide, 10.72 g distilled water and 3.26 g TEOS under vigorously stirring to get a clear solution until get a sol. And then, 3.03 g tetrapropylammonuim hydroxide (TPAOH, 10%) was added dropwise into the sol. Stirring was continued to form a solidified gel at 40 ^{o}C. The resultant wet gel was aged at 60 ^{o}C for 8 h and subsequently, dried at 90 ^{o}C for 12 h. Then, the as-prepared gel was crystallized by SAC method at 160 ^{o}C for 18 h. The obtained sample was washed, filtrated repeatedly for several times and the dried at 120 ^{o}C overnight. Finally, the dried sample was calcined at 500 ^{o}C in air for 5 h to obtain the micro-capsule catalyst. The conventional H-ZSM-5, as a physical mixture catalyst with Fe/SBA-15, was also synthesized by the same method but without Fe addition. For comparison, the physical mixture catalyst (denoted as Fe/SBA-15+SZ) was also prepared by the mechanical mixture of the conventional H-ZSM-5 and Fe/SBA-15 catalyst.

6.2.2 Catalyst characterization

The nitrogen sorption experiments were performed at -196 ^{o}C on a 3Flex analyzer (Micromeritics). The surface area of samples was determined by the Brunauer-Emmett-Teller (BET) method. The pore size distributions were obtained by Barrett-Joyner-Halenda (BJH) method. Micropore volume and surface area were evaluated by the *t*-plot method.

Small-angle X-ray diffraction (SARD) patterns were carried out on a Bruker D8 Advance powder diffraction system with CuKα radiation (40 kV, 40 mA). The wide-angle X-ray diffraction (XRD) patterns were characterized by a Rigaku D/max-2550 V diffractometer with CuKα radiation (40 kV, 40 mA) in the 2θ angle ranging from 5 to 80°.

The surface morphology of samples was characterized with a scanning electron microscopy (SEM, JEOL, JSM-6360LV).

Transmission electron microscopy (TEM) measurements were performed on JEOL JEM-2100 UHR at an acceleration voltage of 200 kV to analysis the morphology of zeolite samples.

Ammonia temperature programmed desorption (NH_3-TPD) experiments were conducted in a flow apparatus on a BELCAT-B-TT (BEL, Japan) instrument. In a typical NH_3-TPD experiment, 0.03 g catalyst was first loaded in a quartz reactor in flowing He at 150 ^oC for 1 h and then the followed adsorption was performed by using the 5 % NH_3 in helium flow with a speed of 20 mL/min at 80 ^oC for 20 min. The desorption process first proceeded the treatment of saturated catalyst at 80 ^oC for 30 min and then the gas desorption step was then implemented with the increased temperature from 80 ^oC to 800 ^oC at the rate of 5 ^oC/min in flowing He (20 mL/min) atmosphere.

6.2.3 Isoparaffin direct synthesis reaction

FTS reaction was carried out using a pressurized stainless steel fixed-bed reactor with H_2/CO ratio of 1:1 and W/F ratio of 10 gh/mol. Before reaction, the catalyst was loaded in the center of reactor and reduced in situ at 400 ^oC in a flow of H_2/CO (1:1, 80 ml/min) for 10 h, and then cooled down to 300 ^oC under N_2 flow. During the reaction, gaseous products were online analyzed by two gas chromatographs (Shimadzu, GC-8A and Shimadzu, GC-14B). Liquid products from an ice trap were analyzed an offline gas chromatograph (Shimadzu GC-2014, FID). The configuration of the reactor was showed in Scheme 6.1.

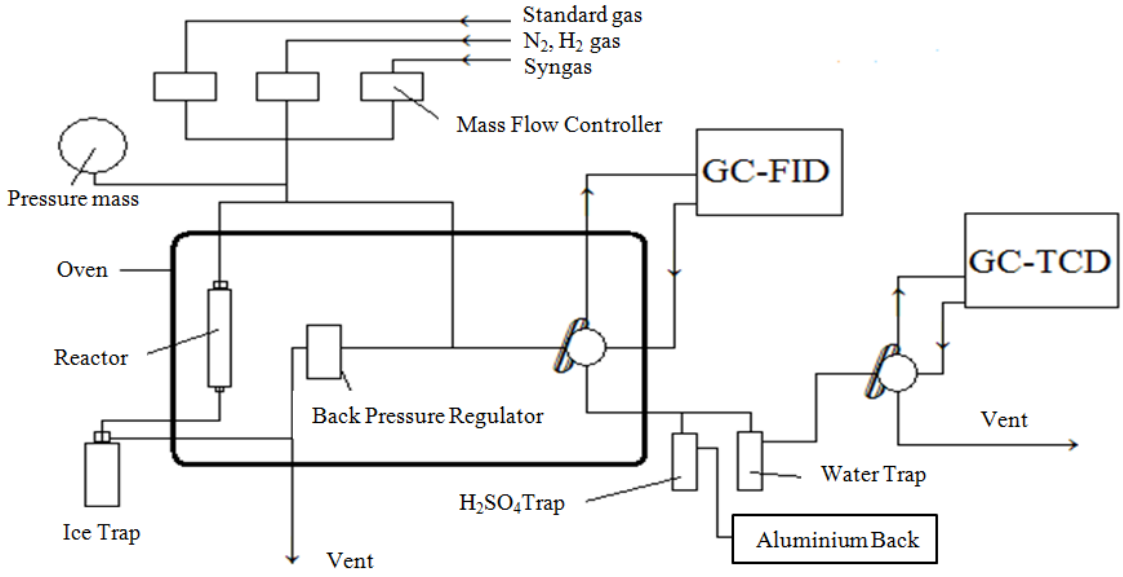

Scheme 6.1. Schematic diagram of FTS reaction

6.3 Results and Discussion

6.3.1 Structures of the micro-capsule catalyst

6.3.1.1 XRD analysis

The XRD patterns of the calcined SBA-15, Fe/SBA-15 and Fe/Silica/SZ are presented in Fig. 6.2. The SBA-15 sample exhibits three diffraction peak at 2θ = 0.9º, 1.6º, and 1.8º (Fig. 6.2a), which indicates the well hexagonal pore structure of SBA-15[39]. However, Fe/Silica/SZ micro-capsule catalyst has not found any signature of peaks in the small-angle X-ray diffraction, indicating that the SBA-15 structure was destroyed during SAC process. After impregnation with iron, the diffraction peaks of Fe_2O_3 appear as shown in Fig. 6.2b. For the micro-capsule catalyst Fe/Silica/SZ, the appearance of XRD reflections at 2θ = 23-25º is the characteristic feature of MFI zeolite, which confirms the existence of H-ZSM-5 zeolite in this capsule catalyst.

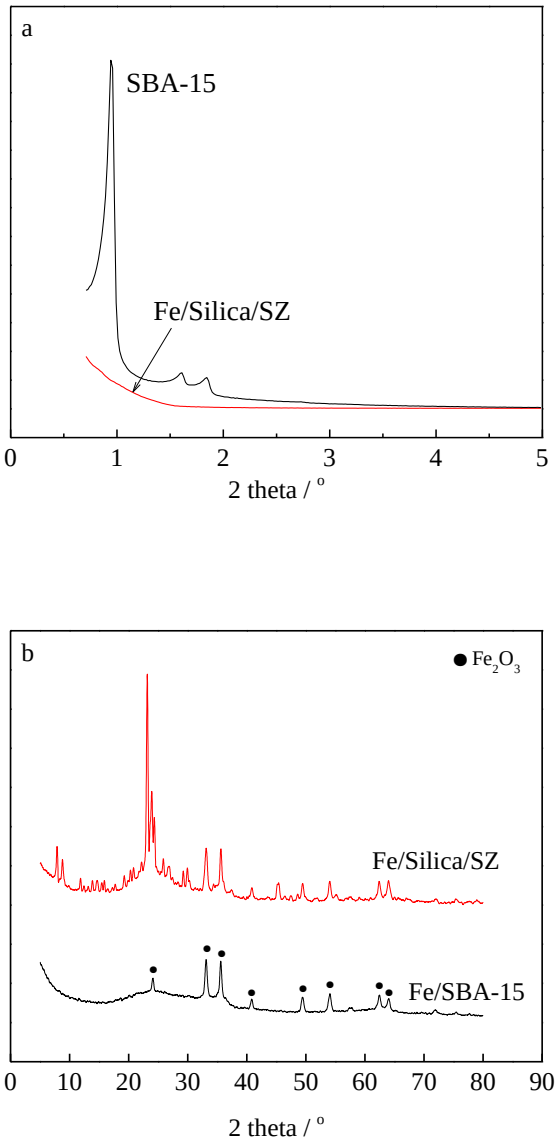

Fig. 6.2. XRD patterns of SBA-15, Fe/SBA-15 and Fe/Silica/SZ

6.3.1.2 Pore properties

The pore structures of the SBA-15 support, Fe/SBA-15 and Fe/Silica/SZ catalysts are characterized by the N_2 sorption analysis. The N_2 adsorption-desorption isotherms and pore size distributions are showed in Fig. 6.3 and the calculated pore parameters are summarized in Table 6.1. SBA-15 presents a typical type IV isotherm with a H1 hysteresis loop, indicating uniform tubular mesopores (6.2 nm, Fig. 6.4b). After the loading of iron, the N_2 adsorption capacity decreased gradually. It means that the loaded iron blocked the partial mesopores of the SBA-15. However, the

Fe/Silica/SZ micro-capsule catalyst exhibits a significant uptake at the relative pressure (P/P_0) of 0.4-0.9, indicating the existence of a broad mesoporous distribution. In addition, an adsorption at P/P_0 = 0.95-1.0 is also observed for Fe/Silica/SZ, indicating the presence of macropores. The macropores may contribute from aggregated zeolite particles.

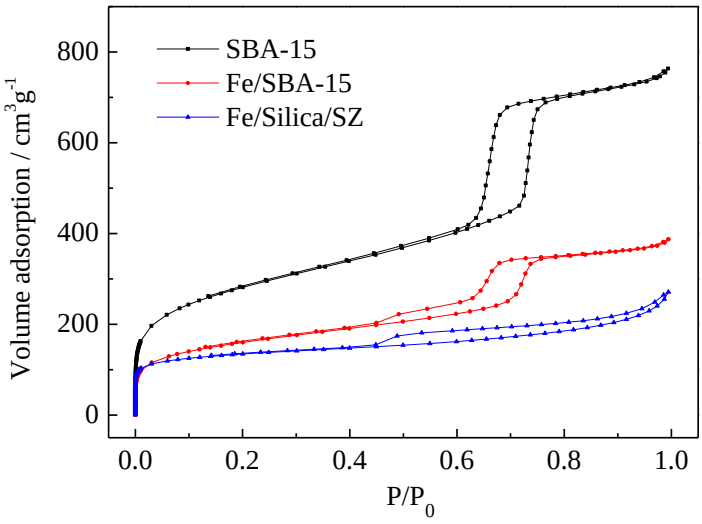

Fig. 6.3. Nitrogen sorption isotherms of SBA-15, Fe/SBA-15 and Fe/Silica/SZ.

As shown in Table 6.1, it can be seen that the SBA-15 support exhibits high surface areas of 993 m^2/g and large pore volume of 1.17 cm^3/g. After impregnation with iron, the surface (560 m^2/g) area and pore volume (0.59 cm^3/g) are lower distinctly than that of SBA-15. Further coating with H-ZSM-5 zeolite on Fe/Silica (Fe/Silica/SZ) results in a remarkable increase of microporous surface area from 161 to 240 m^2/g, suggesting an in-situ crystallization transformation of SBA-15 silicon source during SAC process. Moreover, Fe/Silica/SZ gives the average pore size with 3.6 nm, indicating the formation of mesopores in the capsule catalyst structure.

Table 6.1 Summary of the textural properties of different samples

Sample	$S(m^2/g)$[a]		$V(cm^3/g)$		Average
	Total	Micropore[b]	Total[c]	Micropore[d]	pore size
SBA-15	993	161	1.17	0.07	4.7
Fe/SBA-15	560	127	0.59	0.06	4.2
Fe/Silica/SZ	449	240	0.41	0.12	3.6

[a] BET surface area.
[b] Microporous surface area evaluated by the *t*-plot method.
[c] Total pore volume calculated by single point method at $P/P_0 = 0.99$.
[d] Micropore volume evaluated by the *t* -plot method.

The pore size distributions (PSD) of SBA-15, Fe/SBA-15 and Fe/Silica/SZ samples are display in Fig. 6.4. As shown in Fig. 6.4a, the micropore PSD calculated by the HK method shows a peak centered at 0.59 nm, which is in accordance with the microporosity of the H-ZSM-5 zeolite. Both of SBA-15 and Fe/SBA-15 exhibit a broad microporosity PSD within the micropore range, which derives from the intrawall porosity of SBA-15. The mesopore PSD of samples was calculated by the BJH method. SBA-15 exhibits uniform mesopores and narrow PSD centered at 6.2 nm (Fig. 6.4b). After Fe doped into SBA-15 (Fe/SBA-15), it exhibits two mesopores at 3.8 and 6.2 nm due to the partial blockage of the pores by Fe clusters. For Fe/Silica/SZ catalyst, a similar pore size at 3.8 nm is also observed.

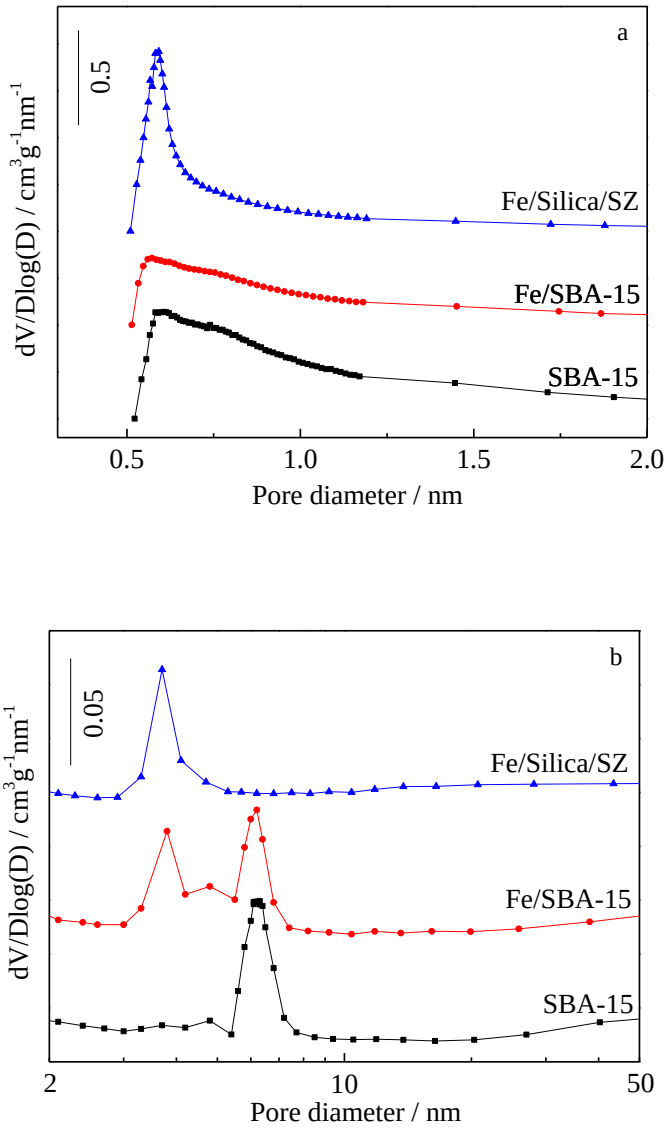

Fig. 6.4. N_2 sorption isotherms (a) and BJH pore size distributions (b) of calcined SBA-15, Fe/SBA-15 and Fe/Silica/SZ

6.3.1.3 Morphology and surface composition analysis

The morphologies of samples are characterized by SEM, and the results are showed in Fig. 6.5. The SEM image of SBA-15 (Fig. 6.5a) shows very uniform rodlike morphology particles, which is in good agreement with the result obtained the low-angle XRD analysis, confirming successful synthesis of high quality SBA-15 silica. The micro-capsule catalyst Fe/Silica/SZ, with Fe/Silica as core and H-ZSM-5 as shell respectively, was prepared by an in-situ crystallization transformation of SBA-15 as silicon source during SAC process. As shown in Fig. 6.5b, Fe/Silica/SZ

reveals the presence of aggregates of worm-like H-ZSM-5 crystals. The TEM image of Fe/Silica/SZ (Fig. 6.5c) shows that the mesoporous channels are disordered, indicating the destroyed SBA-15 structure during SAC process.

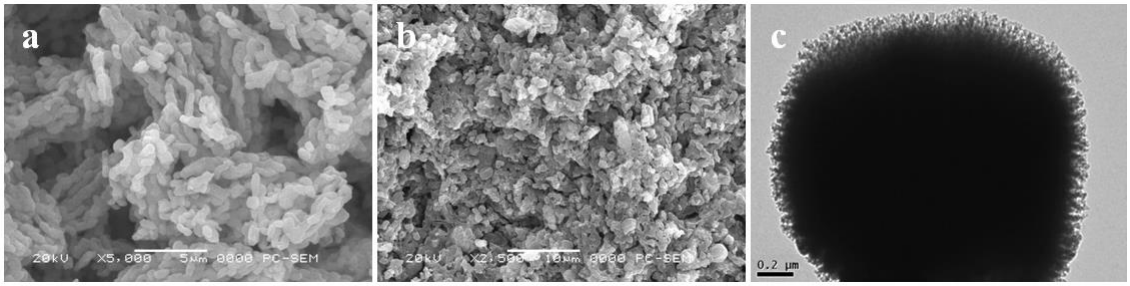

Fig. 6.5 SEM images of (a) SBA-15 and (b) Fe/Silica/SZ and TEM image of (c) Fe/Silica/SZ.

6.3.2 NH_3-TPD characterization

The acidity property of the micro-capsule catalyst was measured by NH_3-TPD. Fig. 6.6 shows the NH_3-TPD profiles of Fe/SBA-15 and Fe/Silica/SZ. There is no obvious NH_3 desorption peak in Fe/SBA-15 sample, indicating that Fe/SBA-15 catalyst has not remarkable acidic sites. Two distinct NH_3 desorption peaks appear in micro-capsule catalyst Fe/Silica/SZ. The desorption peaks above 400 ^oC can be assigned to the desorption of NH_3 from strong B and L sites[40]. The desorption peaks below 400 ^oC can be attributed to weak acidic sites or physically adsorbed ammonia, weak B and L sites. The abundant acidic sites of the micro-capsule catalyst are mainly provided by the H-ZSM-5 shell, which are very important to the performance for middle isoparaffin synthesis.

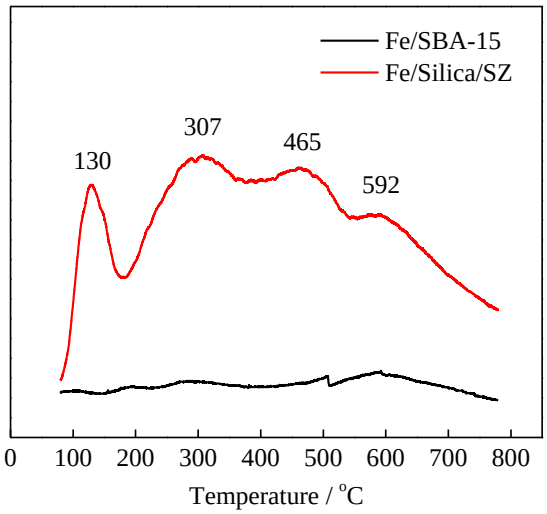

Fig. 6.6. NH_3-TPD profiles of samples

6.3.3 FTS reaction properties

The FTS results and product distributions of core catalyst Fe/Silica, micro-capsule catalyst Fe/Silica/SZ and a physical mixture catalyst Fe/SBA-15+SZ for isoparaffin synthesis were tested in a fixed bed reactor, as shown in Table 6.2 and Fig. 6.7. The CO conversion of Fe/Silica/SZ is 57.6 %, lower than that of Fe/SBA-15, which is mainly ascribed to the partial coverage of Fe active sites by the H-ZSM-5 shell[41]. According to Fig. 6.7 and Table 6.2, Fe/SBA-15 exhibits a broad product distribution up to C_{16}, but the isoparaffin selectivity is only 8.2 % and a high selectivity of olefin with 49.2 %. For Fe/Silica/SZ micro-capsule catalyst, extremely high isoparaffin selectivity with 46.5 % is obtained. Meanwhile, the selectivity of olefin decreases significantly to 16.8 %. Surprisingly, according to the product distributions (Fig. 6.7), the light olefin (C_{2-4}) selectivity decrease suddenly after the doped zeolite with Fe/SBA-15 (Fe/Silica/SZ and Fe/SBA-15+SZ), that is, the transference of a partial FTS products from light olefin to middle isoparaffin, suggesting that the high selectivity of isoparaffin might be mainly attributed to olefin polymerization. For Fe/Silica/SZ, the hydrocracking and isomerization of the formed C_{12+} hydrocarbons may also contribute to improve high isoparaffin selectivity. The translations of olefin and C_{12+} hydrocarbons to isoparaffin are mainly catalyzed by the

acidic sites on H-ZSM-5 shell. It is noted that the increases of CH_4 and CO_2 selectivity are very small after the coating of H-ZSM-5 shell on Fe/Silica core catalyst. This might be due to the small size and thin shell of the micro-capsule catalyst. As the case of physical mixture catalyst (Fe/SBA-15+SZ), a broad product distribution and relative low isoparaffin selectivity (33.9 %) are achieved. In addition, a low light olefin selectivity (2.5 %) is also observed in this catalyst, which further confirmed the translation of light olefin to isoparaffin. It is clear to see that certain amount of C_{12+} fractions (Fig. 6.7) is still produced up to C_{16} hydrocarbons in the mechanical mixture catalyst due to the lack of spatial confinement effect.

Table 6.2 Catalytic performance of the catalysts[a]

Catalysts	Conv./%	Sel./%								
	CO	CO_2	CH_4	$C_{=2-4}$	C_{5+}	C_n	$C_=$	C_{iso}	$C_=/C_n$[b]	C_{iso}/C_n[c]
Fe/SBA-15	68.5	37.0	12.8	23.1	51.0	42.6	49.2	8.2	1.65	0.40
Fe/Silica/SZ	57.6	37.3	15.3	5.8	62.7	36.7	16.8	46.5	0.79	3.71
Fe/SBA-15+SZ	63.6	43.8	19.2	2.5	54.1	56.0	10.1	33.9	0.27	1.67

[a] Reaction conditions: Catalyst weight, 0.5 g; T, 300 °C; P, 1.0 MPa; H_2/CO, 1; W/F, 10 gh/mol.
[b] $C_=/C_n$ is the ratio of olefin to paraffin of C_{2+}.
[c] C_{iso}/C_n is the ratio of olefin to paraffin of C_{4+}.

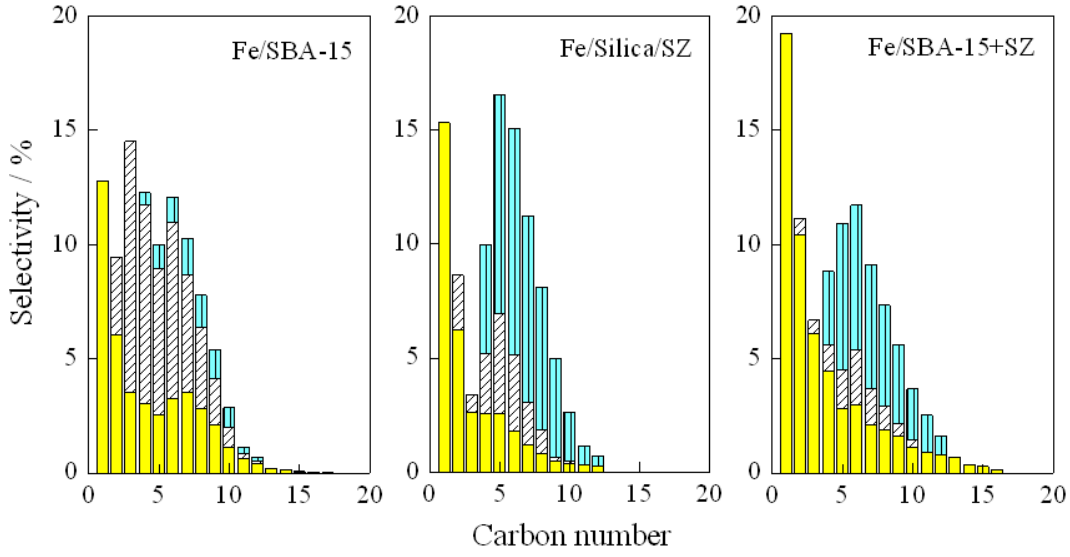

Fig. 6.7. FTS product distributions of catalysts:
yellow, n-paraffin; *gray (slash)*, olefin; *cyan (perpendicular)*, isoparaffin.

According to the structure characterization and performance tests, the schematic diagram of direct synthesis of middle isoparaffin over the micro-capsule catalyst is showed in Fig. 6.8. Syngas first passes through the mesoporous channels of core to contact the active sites, where normal paraffin and olefin are formed. The formed light olefin and long chain paraffin subsequently convert to isoparaffin by the catalysis of the acidic sites of H-ZSM-5 shell. High selective of middle isoparaffin is realized with the help of spatial confinement effect of H-ZSM-5 shell. The mesoporous channels of micro-capsule catalyst core (Fe/Silica) can offer a high diffusion rate of reactants and products, as well as the H-ZSM-5 micropores shell with acidic sites afford to hydrocrack and isomerize the heavy hydrocarbons, simultaneously tuning the products selectivity as desired.

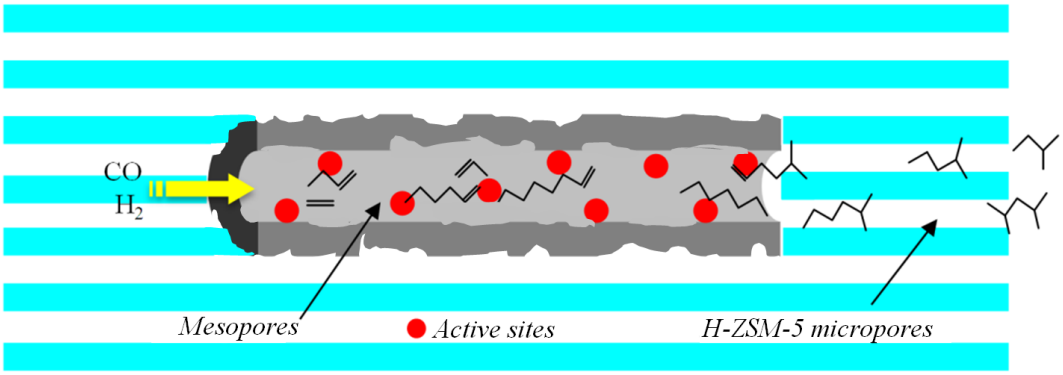

Fig. 6.8. Schematic diagram of middle isoparaffin direct synthesis over the micro-capsule catalyst

6.4 Conclusion

In summary, a novel micro-capsule catalyst with interior Fe/Silica core and exterior H-ZSM-5 shell was firstly designed and performed for direct synthesis of middle isoparaffin from syngas. The as-prepared micro-capsule catalyst Fe/Silica/SZ achieved an excellent performance with 46.5 % isoparaffin selectivity. Different from zeolite coated cobalt catalyst, the high isoparaffin selectivity of micro-capsule catalyst was mainly attributed to the polymerization of the light olefin catalyzed by the H-ZSM-5 zeolite shell. The spatial confinement effect of the H-ZSM-5 zeolite shell acted as an important role for the improvement of isoparaffin selectivity. The newly

developed heterogeneous catalyst preparation method reported here will be also widely applied in designing other similar micro-capsule catalyst for varied tandem catalysis processes.

References

[1] Q. Zhang, J. Kang, Y. Wang, ***ChemCatChem*** 2 (2010), 1030-1058.

[2] S. Sartipi, K. Parashar, M. Makkee, J. Gascon, F. Kapteijn, ***Catal. Sci. Technol.*** 3 (2013), 572-575.

[3] J.Y. Liu, J.F. Chen, Y. Zhang, ***Catal. Sci. Technol.*** 3 (2013), 2559-2564.

[4] K. Cheng, J. Kang, S. Huang, Z. You, Q. Zhang, J. Ding, W. Hua, Y. Lou, W. Deng, Y. Wang, ***ACS Catal.*** 2 (2012), 441-449.

[5] S. Sartipi, M. Alberts, V.P. Santos, M. Nasalevich, J. Gascon, F. Kapteijn, ***ChemCatChem*** 6 (2014), 142-151.

[6] S. Sartipi, K. Parashar, M.J. Valero-Romero, V.P. Santos, B. van der Linden, M. Makkee, F. Kapteijn, J. Gascon, ***J. Catal.*** 305 (2013), 179-190.

[7] S. Sartipi, M. Makkee, F. Kapteijn, J. Gascon, ***Catal. Sci. Technol.*** 4 (2014), 893.

[8] J. Sun, W. Niu, A. Taguchi, T. Abe, Y. Yoneyama, N. Tsubaki, ***Catal. Sci. Technol.*** 4 (2014), 1260-1267.

[9] J. Sun, X. Li, A. Taguchi, T. Abe, W. Niu, P. Lu, Y. Yoneyarna, N. Tsubaki, ***ACS Catal.*** 4 (2014), 1-8.

[10] Y. Yoneyama, J. He, Y. Morii, S. Azuma, N. Tsubaki, ***Catal. Today*** 104 (2005), 37-40.

[11] S.H. Kang, J.H. Ryu, J.H. Kim, P.S. Prasad, J.W. Bae, J.Y. Cheon, K.W. Jun, Catal. Lett. 141 (2011), 1464-1471.

[12] J. Sun, C. Xing, H. Xu, F. Meng, Y. Yoneyama, N. Tsubaki, ***J. Mater. Chem. A*** 1 (2013), 5670-5678.

[13] S.H. Kang, J.H. Ryu, J.H. Kim, I.H. Jang, A.R. Kim, G.Y. Han, J.W. Bae, K.S. Ha, ***Energy Fuel*** 26 (2012), 6061-6069.

[14] G. Yang, C. Xing, W. Hirohama, Y. Jin, C. Zeng, Y. Suehiro, T. Wang, Y. Yoneyama, N. Tsubaki, ***Catal. Today*** 215 (2013), 29-35.

[15] J. Bao, J. He, Y. Zhang, Y. Yoneyama, N. Tsubaki, ***Angew. Chem. Int. Ed.*** 47 (2008), 353-356.

[16] J. He, Z. Liu, Y. Yoneyama, N. Nishiyama, N. Tsubaki, ***Chem. Eur. J.*** 12 (2006), 8296-8304.

[17] Y. Jin, R. Yang, Y. Mori, J. Sun, A. Taguchi, Y. Yoneyama, T. Abe, N. Tsubaki, ***Appl. Catal. A Gen.*** 456 (2013), 75-81.

[18] Y. Li, T. Wang, C. Wu, Y. Lv, N. Tsubaki, ***Energy Fuel*** 22 (2008), 1897-1901.

[19] C. Xing, G. Yang, D. Wang, C. Zeng, Y. Jin, R. Yang, Y. Suehiro, N. Tsubaki, ***Catal. Today*** 215 (2013), 24-28.

[20] B. Sun, G. Yu, J. Lin, K. Xu, Y. Pei, S. Yan, M. Qiao, K. Fan, X. Zhang, B. Zong, ***Catal. Sci. Technol.*** 2 (2012), 1625-1629.

[21] Q. Lin, G. Yang, X. Li, Y. Yoneyama, H. Wan, N. Tsubaki, ***ChemCatChem*** 5 (2013), 3101-3106.

[22] S. Chen, J. Li, Y. Zhang, Y. Zhao, J. Hong, ***Catal. Sci. Technol.*** 3 (2013), 1063-1068.

[23] Q. Cai, J.L. Li, ***Catal. Commun.*** 9 (2008), 2003-2006.

[24] L.A. Cano, M.V. Cagnoli, J.F. Bengoa, A.M. Alvarez, S.G. Marchetti, ***J. Catal.*** 278 (2011), 310-320.

[25] L.F.F.P.G. Braganca, M. Ojeda, J.L.G. Fierro, M.I.P. da Silva, ***Appl. Catal. A Gen.*** 423 (2012), 146-153.

[26] L.A. Cano, M.V. Cagnoli, N.A. Fellenz, J.F. Bengoa, N.G. Gallegos, A.M. Alvarez, S.G. Marchetti, ***Appl. Catal. A Gen.*** 379 (2010), 105-110.

[27] S. Chen, J. Li, Y. Zhang, Y. Zhao, K. Liew, J. Hong, ***Catal. Sci. Technol.*** 4 (2014), 1005-1011.

[28] J. Panpranot, J.G. Goodwin Jr., A. Sayari, ***J. Catal.*** 211 (2002), 530-539.

[29] J. Panpranot, J.G. Goodwin Jr., A. Sayari, ***J. Catal.*** 213 (2003), 78-85.

[30] B. Yilmaz, U. Muller, M. Feyen, S. Maurer, H. Zhang, X. Meng, F.S. Xiao, X. Bao, W. Zhang, H. Imai, T. Yokoi, T. Tatsumu, H. Gies, T. De Baerdemaeker, D. De Vos, ***Catal. Sci. Technol.*** 3 (2013), 2580-2586.

[31] X. Meng, F.S. Xiao, ***Chem. Rev.*** 114 (2014), 1521-1543.

[32] L.H. Chen, X.Y. Li, J.C. Rooke, Y.H. Zhang, X.Y. Yang, Y. Tang, F.S. Xiao, B.L. Su, ***J. Mater. Chem.*** 22 (2012), 17381-17403.

[33] G. Yang, N. Tsubaki, J. Shamoto, Y. Yoneyama, Y. Zhang, ***J. Am. Chem. Soc.*** 132 (2010), 8129-8136.

[34] G. Yang, M. Thongkam, T. Vitidsant, Y. Yoneyama, Y. Tan, N. Tsubaki, ***Catal. Today*** 171 (2011), 229-235.

[35] K. Pinkaew, G. Yang, T. Vitidsant, Y. Jin, C. Zeng, Y. Yoneyama, N. Tsubaki, ***Fuel*** 111 (2013), 727-732.

[36] G. Yang, Kawata, Q. Lin, J. Wang, Y. Jin, C. Zeng, Y. Yoneyama, N. Tsubaki, ***Chem. Sci.*** 4 (2013), 3958-3964.

[37] D. Zhao, J. Feng, Q. Huo, N. Melosh, G.H. Fredrickson, B.F. Chmelka, G.D. Stucky, ***Science*** 279 (1998), 548-552.

[38] J. Zhou, Z. Hua, Z. Liu, W. Wu, Y. Zhu, J. Shi, ***ACS Catal.*** 1 (2011), 287-291.

[39] Q.Q. Hao, Y.H. Zhao, H.H. Yang, Z.T. Liu, Z.W. Liu, ***Energy Fuel*** 26 (2012), 6567-6575.

[40] F. Lonyi, J. Valyon, ***Micropor. Mesopor. Mater.*** 47 (2001), 293-301.

[41] G. Yang, J. He, Y. Zhang, Y. Yoneyama, Y. Tan, Y. Han, T. Vitidsant, N. Tsubaki, ***Energy Fuel*** 22 (2008), 1463-1468.

Chapter 7 Summary and outlook

Interest in the carbon dioxide reforming of methane has been increasing owing to the issues of natural gas utilization, the reduction of greenhouse gases and syngas gas (H_2 + CO) production, as shown in **Chapter 1**. Ni based catalysts for the carbon dioxide reforming of methane are the most popular catalysts because of their low cost and high activity. However, Ni/γ-Al_2O_3 catalyst without promoter addition exhibited low catalytic activity and abundant carbon deposition. With the La_2O_3-CeO_2 binary promoters on Ni/γ-Al_2O_3 catalyst, it not only was the amount of carbon deposition decreased, but the activity was also improved due to alkaline function and dispersion action of La_2O_3-CeO_2, as well as the electronic interactions between CeO_2 and nickel. Ni based catalysts usually deactivated because of metal sintering and/or carbon deposition, which is the most important problem on the future development of the CO_2 reforming of CH_4 reaction.

Design and development of catalyst formulations that maximize the direct production of liquid fuels via transformation syngas by combining conventional Fischer-Tropsch synthesis (FTS), hydrocarbon cracking, and isomerization into one single catalyst particle have been investigated in this thesis, as shown in **Chapter 2** to **Chapter 6**.

The depletion of crude oil and the rapid growing demand of liquid fuels have attracted more interest for the synthesis of alternative fuels from the rich-reserved coal, natural gas and renewable biomass via FTS reaction. Generally, the FTS reaction mainly produces normal paraffin and some building-block chemicals such as lower olefin (**Chapter 2**), which can not be directly used as the transportation fuels, especially for the extensively demanded gasoline (**Chapter 3** to **Chapter 6**). For conventional catalyst, it is acknowledged that the FTS products obey the Anderson-Schulz-Flory (ASF) law. Middle hydrocarbons, with a range of $C_{5\text{-}11}$, particularly rich in isoparaffin and olefin, as gasoline-range liquid fuels with high

octane value, are important fuel from petrochemical industry

Bifunctional catalysts with the combination of the conventional FTS catalyst and acidic zeolite, were studied widely for direct synthesis of middle isoparaffin (**Chapter 3** to **Chapter 6**). In this thesis, there are two kinds of bifunctional catalysts for direct synthesis of middle isoparaffin: hierarchical zeolite supported metal catalyst (**Chapter 4 and Chapter 5**), and the capsule or coating catalyst with the conventional FTS catalyst core and zeolite shell (**Chapter 3 and Chapter 6**). Capsule catalyst is more effective for isoparaffin synthesis because of the spatial confinement effect and unique pore structure of the zeolite shell, which could enforce effectively the hydrocracking/isomerization of long chain hydrocarbons. Cobalt based capsule catalysts have been studied extensively for the direct isoparaffin synthesis (**Chapter 3**). Fe based catalysts have much lower cost and methane selectivity than Co based catalysts, which are proper candidates for the capsule catalyst (**Chapter 6**). In **Chapter 4 and Chapter 5**, the hierarchically bifunctional catalysts were also successfully synthesized and evaluated for direct synthesis of middle isoparaffin as gasoline with high octane value via FTS reaction to realize a sharp anti-ASF law product distribution.

Further modification of the bifunctional catalysts may lead to the commercialization of this novel Fischer-Tropsch process with tailored product selectivity in the near future. However, in spite of these advantages, a number of drawbacks need to be pointed in order to make the direct synthesis of isoparaffin from syngas more attractive, as follow: (i) the high selectivity towards methane derived from the strong interactions between the FTS phase and the zeolite. (ii) the long-term stability of these catalysts has been largely unexplored. Future studies should be considered and researched in deeply.

List of Publication

(1) **Chuang Xing**, Guohui Yang, Ding Wang, Chunyang Zeng, Yuzhou Jin, Ruiqin Yang, Yoshifumi Suehiro, Noritatsu Tsubaki*, Controllable encapsulation of cobalt clusters inside carbon nanotubes as effective catalysts for Fischer-Tropsch synthesis, ***Catalysis Today***, 215, 24-28, 2013.

(2) Guohui Yang, **Chuang Xing**, Wataru Hirohama, Yuzhou Jin, Chunyang Zeng, Yoshifumi Suehiro, Tiejun Wang, Yoshiharu Yoneyama, Noritatsu Tsubaki*, Tandem catalytic synthesis of light isoparaffin from syngas via Fischer-Tropsch synthesis by newly developed core-shell-like zeolite capsule catalysts, ***Catalysis Today***, 215, 29-35, 2013.

(3) Ruiqin Yang, **Chuang Xing**, Chengxue Lv, Lei Shi, Noritatsu Tsubaki*, Promotional effect of La_2O_3 and CeO_2 on Ni/Al_2O_3 catalysts for CO_2 reforming of CH_4, ***Applied Catalysis A: General***, 385, 92-100, 2010.

(4) Jian Sun, **Chuang Xing**, Hengyong Xu, Fanqiong Meng, Yoshiharu Yoneyama, Noritatsu Tsubaki*, Filter and buffer-pot confinement effect of hollow sphere catalyst for promoted activity and enhanced selectivity, ***Journal of Materials Chemistry A***, 1, 5670-5678, 2013.

(5) Chun Jin, **Chuang Xing**, Fan Wang, Wenzhong Shen*, Rapid synthesis of functional carbon microspheres: preparation, forming mechanism and application in formic acid and ammonia treatment, ***Science of Advanced Materials***, 5, 663-667, 2013.

(6) Pei Li, **Chuang Xing,** Tuoping Hu, Wenzhong Shen*, Synthesis of carbon microsphere under hydrothermal carbonization process and its adsorption for formic acid and ammonia, ***Journal of Biobased Materials and Bioenergy***, 8, 21-26, 2014.

(7) Ding Wang, Xiaoyu Sun, **Chuang Xing**, Guohui Yang, Kai Tao, Tokimasa Kawabata, Kenji Matsuda, Yisheng Tan, Noritatsu Tsubaki*, Copper nanoparticles decorated inside or outside carbon nanotubes used for methyl acetate hydrogenation.

Journal of Nanoscience and Nanotechnology, 13, 1274-1277, 2013.

(8) Lei Shi, Kai Tao, Ruiqin Yang, Fanzhi Meng, **Chuang Xing**, Noritatsu Tsubaki*, Study on the preparation of Cu/ZnO catalyst by sol–gel auto-combustion method and its application for low-temperature methanol synthesis, ***Applied Catalysis A: General***, 401, 46-55, 2011.

(9) **Chuang Xing,** Wenzhong Shen, Guohui Yang, Ruiqin Yang, Peng Lu, Jian Sun, Yoshiharu Yoneyama, Noritatsu Tsubaki*, Completed encapsulation of cobalt particles in mesoporous H-ZSM-5 zeolite catalyst for direct synthesis of middle isoparaffin from syngas, ***Catalysis Communications***, 55, 53-56, 2014.

(10) **Chuang Xing,** Jian Sun, Guohui Yang, Wenzhong Shen, Li Tan, Masahiro Kyodo, Ruiqin Yang, Yoshiharu Yoneyama, Noritatsu Tsubaki*, Tunable isoparaffin and olefin synthesis in Fischer-Tropsch synthesis achieved by composite catalyst, ***Fuel Processing Technology***, *minor revise, under review*.

(11) **Chuang Xing,** Qingjun Chen, Guohui Yang, Peng Lu, Wenzhong Shen, Jianwei Mao, Ruiqin Yang, Noritatsu Tsubaki*, Tunable isoparaffin and olefin yields in Fischer-Tropsch Synthesis achieved by a novel iron based micro-capsule catalyst, ***Catalysis Today***, *under review.*

(12) **Chuang Xing,** Guohui Yang, Mingbo Wu, Li Tan, Jian Sun, Peng Lu, Jianwei Mao, Ruiqin Yang, Yoshiharu Yoneyama, Noritatsu Tsubaki*, Hierarchical zeolite Y supported cobalt as bifunctional catalyst for tuning product selectivity in Fischer-Tropsch synthesis reaction, ***Fuel,*** *preparation*.

(13) **Chuang Xing**, Guohui Yang, Li Tan, Wenzhong Shen, Xikun Gai, Jianwei Mao, Ruiqin Yang, Noritatsu Tsubaki*, A hierarchically spherical Co-based zeolite with aggregated nanorods structure for improved Fischer-Tropsch synthesis reaction activity and isoparaffin selectivity, *manuscript finished*.

List of International Conferences

(1) **Chuang Xing**, Guohui Yang, Ding Wang, Chunyang Zeng, Yuzhou Jin, Ruiqin Yang, Yoshifumi Suehiro, Noritatsu Tsubaki*, Controllable encapsulation of cobalt clusters inside carbon nanotubes as effective catalysts for Fischer-Tropsch synthesis. *Synfuel2012*, Oral, Munich, Germany, 2012 June 29-30.

(2) **Chuang Xing,** Yoshinori Kozakura, Yoshiharu Yoneyama, Noritatsu Tsubaki*, Direct synthesis of middle isoparaffin from syngas using the completed encapsulation of cobalt particles in ordered mesoporous H-ZSM-5 as catalyst. *The 7th International Symposium on Acid-Base Catalysis*, Poster, Tokyo, Japan, 2013 May 12-15.

(4) **Chuang Xing,** Jian Sun, Ruiqin Yang, Yoshiharu Yoneyama, Noritatsu Tsubaki,* Catalytic cracking of 4-(1-naphthylmethyl)bibenzyl in sub- and supercritical water. *The 7th Tokyo Conference on Advanced Catalytic Science and Technology*, Poster, Kyoto, Japan, 2014 June 01-06.

(5) **Chuang Xing,** Wenzhong Shen, Qingjun Chen, Peng Lu, Jianwei Mao, Ruiqin Yang, Yoshiharu Yoneyama, Noritatsu Tsubaki*, Novel iron based micro-capsule catalyst for the direct synthesis of middle isoparaffin from syngas, *The 13th International Conference on Inorganic Membranes*, Poster, Brisbane, Australia, 2014 July 06-09.

Acknowledgements

My deepest gratitude goes first and foremost to Professor Noritatsu Tsubaki, my supervisor, for his invaluable guidance, innovative suggestions, continued patience and constant encouragement. He has walked me through all the stages of the writing of this thesis. Without his consistent and illuminating instruction, this thesis could not havereached its present form. His love of science and desire for excellence will remain an inspiration to me in further.

Second, I would like to express my heartfelt gratitude to Associate Professor Yoshiharu Yoneyama for his much assistance in experiments and discussion in this research. My heart was very touched when he experimentalized hand by hand.

I would like to especially thank Dr. Guohui Yang who shared his knowledge, attention and resources. I am extremely grateful to thank the colleagues in Tsubaki Lab, Dr. Xiaoguang San, Dr. Lei Shi, Dr. Ding Wang, Dr. Qingxiang Ma, Dr. Chunyang Zeng, Dr. Jian Sun, Dr. Peng Lu, Dr. Pengfei Zhu, Dr. Minghui Tan, Mr. Li Tan, and Mr. Masahiro Kyoto, for their deep friendships and many helpful discussions.

Furthermore, I am very thankful for the helpful discussions and advice given by visiting Prof. Hengyong Xu, Prof. Wenzhong Shen, Prof. Mingbo Wu, Prof. Xuejun Zhang, Prof. Yisheng Tan and Dr. Mingyue Ding.

I must express the deep respect to Prof. Ruiqin Yang in Zhejiang University of Science and Technology, my supervisor in Bachelor. Five years ago, under her recommendation, I studied in University of Toyama, who tuned into a change my fate.

Finally, I would like to thank my family for their love, understanding, patience, support and many sacrifices.